Summer 8-2014

# Fluorine Containing UV-Curable Materials for Advanced Transport Applications

James Thomas Goetz
*University of Southern Mississippi*

## Recommended Citation

Goetz, James Thomas, "Fluorine Containing UV-Curable Materials for Advanced Transport Applications" (2014). *Dissertations*. 286.
https://aquila.usm.edu/dissertations/286

The University of Southern Mississippi

# FLUORINE CONTAINING UV-CURABLE MATERIALS FOR ADVANCED TRANSPORT APPLICATIONS

by

James Thomas Goetz

Abstract of a Dissertation
Submitted to the Graduate School
of The University of Southern Mississippi
in Partial Fulfillment of the Requirements
for the Degree of Doctor of Philosophy

August 2014

# ABSTRACT

# FLUORINE CONTAINING UV-CURABLE MATERIALS FOR ADVANCED TRANSPORT APPLICATIONS

by James Thomas Goetz

August 2014

The characterization of structure, thermal, gas transport, and free volume properties of two unique UV cured polymeric systems are studied and reported. In the initial pursuit of waterproof high water vapor transport membranes, it became apparent that the UV curing of fluorinated materials yielded routes to develop unique materials that fundamentally challenge conventional models for free volume and light gas transport behavior. UV-curing provides a means to rapidly “lock-in” morphologies that are accessible in the small molecule, monomer phase but rapidly become kinetically inaccessible when constraints such as covalent bonding and cross linking limit motion in the polymer system. This “locking-in” was exploited in Chapters II, III, IV, and V while Chapters VI and VII study this phenomenon.

While the motivation for this project stems from the ability to selectively transport water vapor over bulk water, similar principals are used in the selective transport of light gases. Light gases were extensively used in this work to probe the molecular structures of high permeability polymer networks. Probing of these molecular structures was supported by extensive free volume analysis using both volumetric and molecular probing of free volume properties.

The first chapter of this document outlines the basics of fluorinated, UV cured and thiol-ene materials, transport of gases in polymeric systems, and free volume. These topics are complimented by a discussion of the methods used throughout this work to study the phenomena described.

Chapter II gives brief overview of our research group's historical modification of thiol-ene networks. Through the modification of a tetrafunctional thiol with various chemical moieties, our group has shown the ability to retain the glass transition temperature of a network while tuning the permeability of the system over three orders of magnitude through the use of hydrogen bonding groups, linear aliphatic, and linear perfluorinated modifications. UV-curing allows for the rapid development of a network where monomer functionality was retained, leading to networks with similar long range connectivity and short range differences in backbone spacing and free volume. Chapter III continues this work by exploring the modification of thiol-ene networks with silane groups. Chapter IV delves into the details of the modification procedure using perfluorinated acrylate moieties as the modification. By changing the length of linear perfluorinated acrylates bound covalently into the network, the repulsion of the network backbone by the fluorinated moiety increases. This phenomenon was evidenced by free volume, X-ray diffraction, DSC and pressure volume temperature data and analysis. The resulting "thermodynamic frustration," caused by the incompatible fluorinated groups, increased the transport of light gases across 2.5 orders of magnitude in some cases and shows a stretching of the network backbone structure without impacting glass transition temperature.

Chapters VI and VII highlight the exploration of “switchable” fluorinated UV-cured acrylate side chain polymers. The rigid rod structure of side chain acrylates of a given length gives rise to a morphology that has a well-defined crystalline order and melting temperature. Melting of this ordered structure gives rise the “switching” behavior that can be utilized as a molecular valve for certain applications, activated using a thermal stimulus. The well-defined order of $C_8F_{17}$- and $C_{10}F_{21}$ side chain acrylates was well characterized and shown to develop a mesophase upon UV-curing that was irreversible unless quenched using liquid nitrogen. The well-defined melting temperature of 72 °C was exploited in the study of gas transport properties that traversed this melting temperature, showcasing the permeability switching. Permeability gains across the melting of the ordered morphology, for several gases, were shown to be due to solubility increases alone. Contrary to standard two-phase systems where ordered phases increase tortuosity and therefore decrease diffusivity in the semicrystalline systems, these systems show no discernable switch in diffusivity across the transition temperature. Analysis of both the free volume hole size and volume contributions are reported. Furthermore, the side chain morphology lends itself to high $He/H_2$ separation performance.

The University of Southern Mississippi

# FLUORINE CONTAINING UV-CURABLE MATERIALS FOR ADVANCED TRANSPORT APPLICATIONS

by

James Thomas Goetz

A Dissertation
Submitted to the Graduate School
of The University of Southern Mississippi
in Partial Fulfillment of the Requirements
for the Degree of Doctor of Philosophy

Approved:

Committee Chair

Dean of the Graduate School

August 2014

# DEDICATION

This work is dedicated to my mother and father for their never-ending love, sacrifice, and support in the pursuit of my education.

# ACKNOWLEDGMENTS

I want to acknowledge my advisor and friend Sergei Nazarenko on countless measures. During the past four and a half years of my graduate education, Dr. Nazarenko has challenged me to think beyond the current understanding of my research and has driven me to dive into the pure fundamentals of the work you see here. He has pushed me to become a better writer and a better scientist during the process. He has granted me complete intellectual freedom, allowing me to pursue projects that in some cases have led to interesting discoveries and in others, lessons learned. Dr. Nazarenko allowed me to pursue a hobby of computer programming and electronics in order to contribute to the improvement of infrastructure of the lab which will stand as my “legacy” in the group for years to come. I could not have asked for a better advisor.

Luke Kwisnek has been an invaluable resource, friend, and mentor throughout my PhD career. At PSU I learned of his legacy but only experienced his expertise when I fell in his footsteps again at USM. His research set the ground work and the springboard for my research. Without his guidance and training, I would not have accomplished what you will see in this document.

My summer students, Brian Greenhoe, Setedra Anderson, Jacob Schekman, and Erik Wislinsky, and my high school students, De’Andre Stafford-May, Chris Jenkins, and O’Meshia Moffett, taught me something I never expected to learn in graduate school, how to teach. For this I am forever grateful.

I would also like to acknowledge the School of Human Performance and Recreation for their support during my tenure at USM. Dr. Trent Gould and Dr. Scott Piland pushed me to become a professional scientist and helped me understand how to face adversity and overcome obstacles in my research.

Finally, none of this research would have been possible without the financial support of Fusion UV Systems and the NSF’s GK12 program. Fusion UV Systems gave me and our lab a great opportunity to explore UV polymerizations with near no bounds. This is every researcher’s dream and I am grateful for this opportunity.

## TABLE OF CONTENTS

# LIST OF TABLES

Table

# LIST OF ILLUSTRATIONS

Figure

# CHAPTER I

# RESEARCH BACKGROUND

## Applications and Larger Impact of High Flux Membranes

Gas flux describes the flow of gases or liquids through a substrate per unit area with common units of $cc_{gas}$(STP) $m^{-2}$ $sec^{-1}$. In regards to polymeric membranes, the flux is the measure of gas, liquid, or vapor transport through said membrane. Flux can be altered by changing system parameters such as exposed film area and applied pressure differential or by changing the material according to

$$\text{Equation 1} \quad J = P * \frac{\Delta p}{l}$$

where $\Delta p$ is the pressure differential applied across the film, $l$ is the membrane thickness and $P$ is the permeability coefficient. Permeability is a material property that is dependent on numerous chemical and physical parameters such as chemistry and morphology. Permeability will be discussed later in this chapter.

High flux polymeric membranes find most of their utility in the separation of gases and liquids for purification processes. For example, high flux membranes are used in the enrichment of medical oxygen, removal of $CO_2$ from methane feed streams, and $H_2$ from $CO_2$ streams.[1] There are several groups of materials that show sufficient permeability and separation performance to be industrially viable including polyacetylenes, perfluoro polymers, poly(norbornene)s, polyimides, and thermally rearranged polymers.[2] As will be shown later in this chapter, high permeability requires high free volume. It is therefore no surprise that the highest free volume polymers, poly(1-trimethylsilyl-

1-propyne), poly(4-methyl-2-pentyne) and Teflon AF have very high permeability.[3]

High water vapor transport membranes have been studied for applications in textiles and protective garments.[4,5] The most well-known protective garment material, Gore-TEX, membranes take advantage of the micro porosity of expanded PTFE to achieve high water flux. This type of water proof breathable membrane is susceptible to contamination with oil and dirt and requires a secondary continuous membrane for higher performance.[6] Continuous membranes of linear polymers such as poly(ether-b-amide) (i.e. PEBAX), poly(PBT-b-PEO) (ie Sympatex) rely on water-polymer interactions with the ether linkage.[5,7,8] Commonly, block co-polymers incorporate the soft ethylene or propylene oxide blocks with a more rigid poly(urethane) block in order to retain mechanical strength.[7] This work was aimed at developing a continuous membrane for application in such a system.

Other high flux materials such as soft contact lenses require high oxygen, ion, and water transport to retain comfort and normal corneal metabolism.[9] Historically, a large group of materials have been explored for their high oxygen permeability including, but not limited to, hydrogels, silanes and fluorosilanes, poly(ethylene oxide), poly(propylene oxide), acrylates, and methacrylates. Fluorinated monomers are also used in order to retain oxygen permeability while improving mechanical properties and providing lipophobicity. Providing the required properties for these types of membranes requires a chemistry development platform that is flexible and modular.

As you can see in the few applications shown above, one common trend in high flux membranes is the use of fluorinated or silane polymers. This was the motivation and the driving force behind the following research. The remainder of this chapter will give a stronger background on some of the science behind the topics covered above.

## Fluorine's Peculiar Behavior and Unique Properties

The exceptional properties afforded by fluoro polymers arise from the unique nature of fluorine itself. There is an ever increasing academic interest in fluorinated polymers as noted by the increase in citations in the past 20 years.[10] The location of fluorine on the periodic table gives an insight into some of its unique properties as fluorine is the lightest halogen in the top right of the periodic table with a single missing electron in its p-orbital. Carbon-fluorine bonds are exceptionally strong as fluorine requires a carbon valence electron to fill the p-orbital. Compared to a carbon-hydrogen bond, carbon-fluorine bonds are very strong, 105.4 kcal/mol compared to 98.8 kcal/mol, and even stronger when multiple fluorine atoms are bound to a single carbon 126 kcal/mol in $CF_3$-$CF_3$ compared to 107 kcal/mol in $CH_3$-$CH_2F$. [11,12]

Perfluorinated chains, such as the chains studied in the bulk of this work, benefit from the self-packing nature of fluorine around a carbon chain. The repulsive forces of fluorine in long perfluorinated carbons develop a "protective sheath" around the carbon backbone causing a rigid rod zig-zag type conformation as shown in Figure 1.[13] This highly protective packing also lends saturated fluorocarbons to be very dense compared to hydrocarbon analogs.

Together with the high polarity of the carbon-fluorine bond, the rigid structure of perfluorinated fluorocarbons gives rise to high density and low intermolecular interactions and low surface tensions in polymer systems.[13] Saturated fluorocarbons continuously find new applications in surface coatings, biomedical applications, composites, energy storage, and membranes.[10]

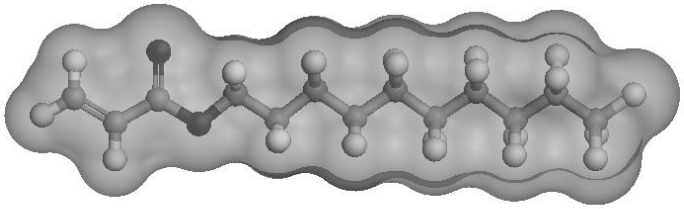

*Figure 1*. A Connolly space filling model of 2-perfluorooctyl ethyl acrylate showing the all trans conformation fluorocarbon tail.

### *UV Initiated Polymerization*

The study and use of UV initiated polymerization chemistries has shown great growth over the past several years with applications in optics, adhesives, micro devices, coatings, high impact polymers, liquid crystalline polymers, and polymer functionalization.[14] The increase in applications and understanding stem from the many benefits of the UV initiated polymerization process. To understand these benefits, a brief introduction to the photopolymerization process is necessary. Figure 2 shows an abbreviated photopolymerization curing scheme of an acrylate polymer. UV initiated radical photopolymerizations use UV light to excite a photo initiator with a photo labile bond to generate radicals (Figure 2A). Rapid initiation occurs as a brief exposure to intense UV light generates large amounts of free radicals within a few seconds.[15] Initiation proceeds through the addition of the first monomer, commonly across the vinylic bond of an acrylate or a methacrylate. Propagation (Figure 2B), the chain growth step, proceeds through the addition of subsequent monomers adding across double bonds, building polymer molecular weight as the chain length increases. The resulting polymer chains are short as a product of various, rapid termination processes. To build molecular weight and obtain applicable materials, multifunctional monomers are incorporated into monomer mixtures prior to curing (Figure 2C).

Termination processes in UV photo polymerizations are a result of bimolecular coupling or, more detrimentally, oxygen inhibition. Bimolecular termination (Figure 2D) is a result of coupling of the propagating polymer chain with another propagating chain or with an initiating radical. Oxygen inhibition occurs when oxygen is present during photo polymerizations.[16] Free radicals, whether from propagating chains or an initiator, are rapidly scavenged by $O_2$, generating peroxy radicals capable of abstracting hydrogen from the polymer chain or generating several undesirable products (Figure 2E) and decreased mechanical properties. Several methods have been used to reduce the amount of $O_2$ inhibition such as increasing initiator concentrations, performing polymerizations in inert $N_2$ or $CO_2$ atmospheres,[14] and adding amines to consume $O_{2,}$[14,17] but require extra infrastructure considerations and increased expense. Recent work has highlighted the attempts to reduce oxygen inhibition through several chemical means.[18]

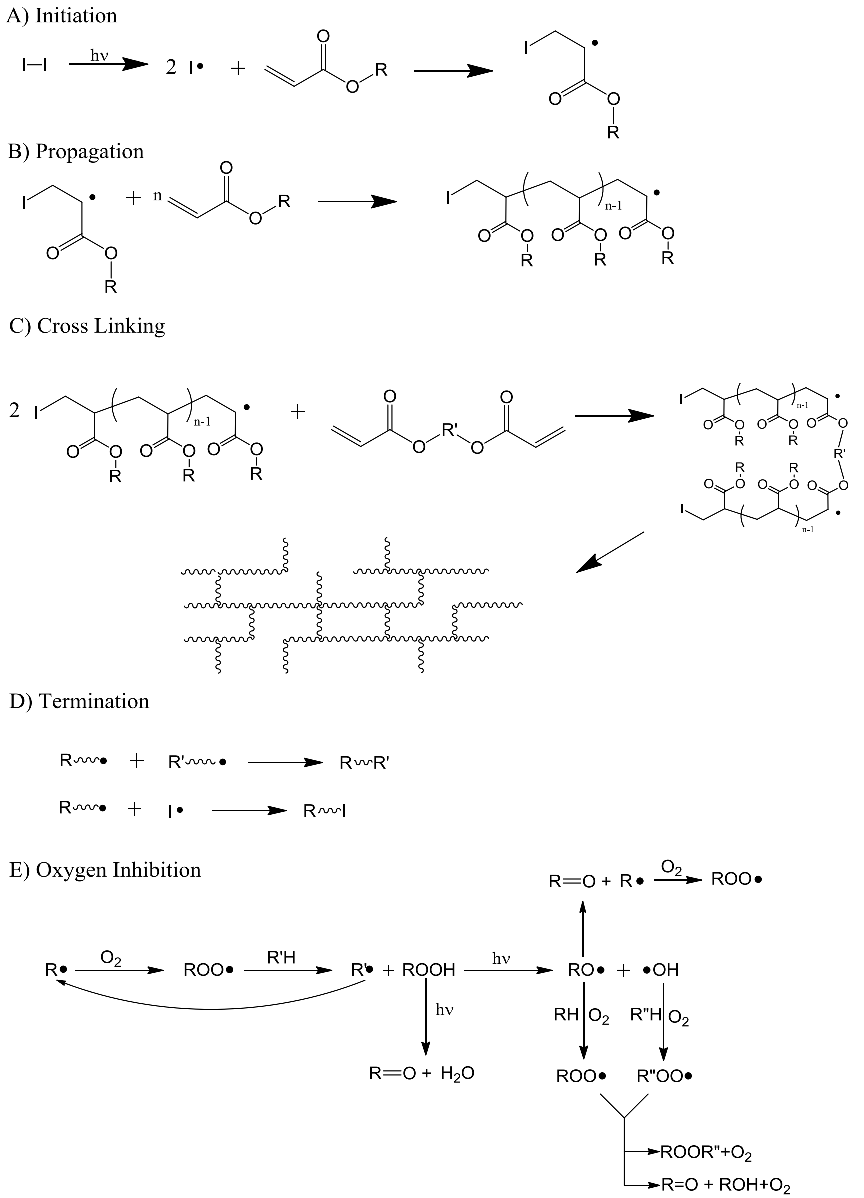

*Figure 2.* Initiation (A), propagation (B), cross linking (C), and termination (D) schemes for a typical UV photopolymerization. Oxygen inhibition (E) occurs in the presence of O2 and retards or restricts UV polymerizations.

Beyond oxygen inhibition, UV polymerization of vinylic monomers are limited in application by high volumetric shrinkage, gelation at low conversion, limited curing of pigmented resins, and difficulty in adhering to substrates during curing.[19] But the advantages of UV curing render these challenges worth overcoming. The rapid kinetics of cure makes processing fast and available to a broad variety of industries. A huge library of commercially available monomers allows for endless formulation possibilities. Relatively low infrastructure cost of lights compared to the infrastructure required for solution and thermal based polymerizations along with the 100% solids, polymerizations without solvents, and, for the most part, liquid monomer precursors, make the utilization of UV cured polymers very attractive on the industrial scale.

### *Thiol-ene Chemistry*

The efficiency and modularity of thiol-ene reactions allowed Hoyle and Bowman[20] to conclude that thiol-ene reactions fall under Sharpless' description of click chemistry. [21] Click chemistry is the classification given to selective, highly efficient, modular, and orthogonal reactions that give no offensive by products. Thiol-ene reactions occur under mild conditions and produce nearly quantitative yields, which allows for the development and study of various polymer systems without intense chemical synthesis or purification methods.

The UV initiated radical addition of a thiol to a carbon-carbon double bond, known as a thiol-ene reaction, has seen resurgence in research in recent years. [19,20,22-25] The benefits of the reaction come from the radical step growth polymerization process of the thiol adding to the ene as shown in Figure 3. A UV generated radical abstracts a labile hydrogen radical from a thiol functionality (Figure 3A) generating a thiyl radical. Propagation (Figure 3B) occurs with the thiyl radical adding across the terminal carbon of a the ene yielding a carbon centered radical which can then abstract a subsequent hydrogen radical from a thiol and continue with propagation or terminate. Termination occurs through dithiol coupling, thiol-carbon radical coupling, or carbon carbon radical coupling

(Figure 3C). Contrary to oxygen inhibition in acrylates, where peroxy radicals cannot add to a double bond, in thiol-ene systems, peroxy radicals are able to extract hydrogen radicals from thiol moieties, allowing for the continuation of the polymerization (Figure 3D).

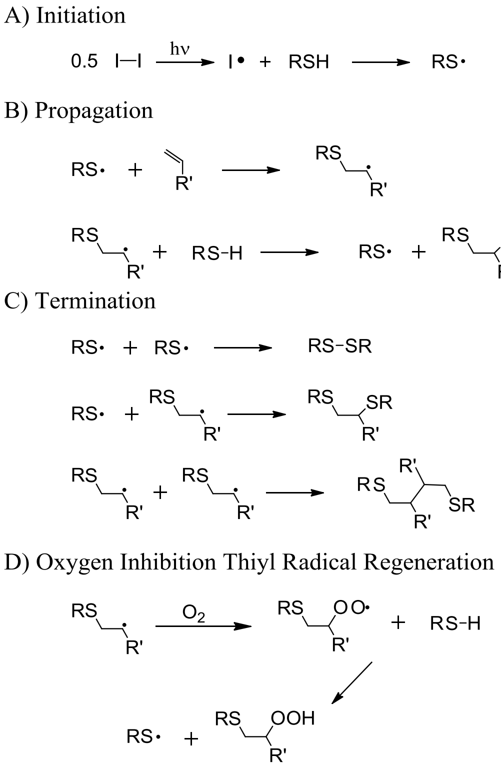

*Figure 3*. Reaction steps in a UV initiated radical step-growth thiol-ene polymerization: initiation (A), propagation (B), termination (C), and oxygen inhibition with subsequent thiyl radical regeneration (D).[19]

Currently there are several limitations that must be overcome before there will be a large dispatch of thiol-ene materials into the market place. First there are a limited number of suppliers of basic thiol building blocks, making supply chain management of source materials a risk that may not be worth taking on for a new product launch. Secondly the application of most thiol-ene polymer networks is limited by very low glass transition temperatures caused by the product thio-ether linkage. Also, the historical bad reputation of thiol monomers having foul odors limits the number of companies willing to pursue thiol-ene chemistries. Yellowing of final films also limited thiol-ene use but these concerns have been alleviated by cleavage type initiators since then.[19]

### *Thiol-Michael Addition*

The wide range of acrylate formulations and polymerization product properties stem from the large acrylate monomer library which includes endless chemical structures, but there are several challenges that restrict the industrial applicability of certain monomers. Thiol-enes benefit from the ease of production but are limited by the availability of functional building block precursors. The thiol-Michael addition allows us to benefit from the massive acrylate monomer library to produce thiol monomers with greater functionality.

The addition of an acrylate to a thiol via a thiol-Michael addition allows for the expansion of the thiol monomer toolbox to include all chemical groups found in the acrylate library of monomers. While thiol-ene networks can be modified with the direct addition of acrylates into the thiol and ene monomer formulation, the UV initiation process would allow for the homopolymerization of the acrylate monomers with the possibility of phase separation of thiol-ene and acrylate polymer systems as shown in Figure 4. Using the thiol-Michael addition, new thiol monomers can be developed from the selective covalent bonding of the acrylate functionality to the thiol functionality.[26-29]

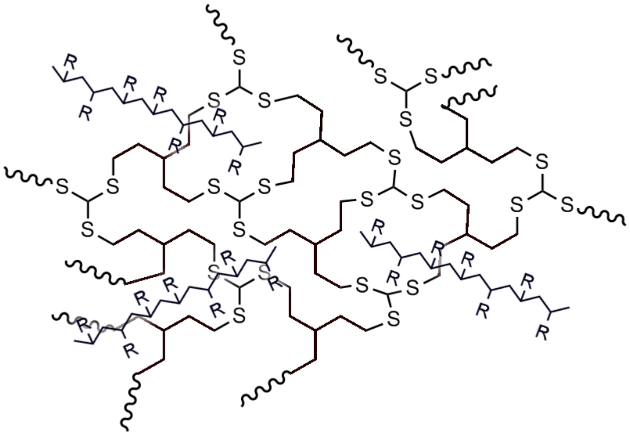

*Figure 4*. The UV cured product of mixing acrylate, thiol and ene monomers could yield homo acrylate polymers along with a thiol-ene acrylate network.

Thiol-Michael addition is described as addition of any electron deficient double bond, such as an acrylate, to yield a thio ether. The proposed mechanism is shown in Figure 5. A full review of the proposed mechanism and its utility are outlined elsewhere.[20,25] First a nucleophilic catalyst adds to the electron deficient double bond. The resulting strong carbanion is able to deprotonate the thiol which can subsequently add to another active double bond.[25] This mechanism is very rapid and produces high yields with no side products, making the thiol-Michael addition a “click” reaction.

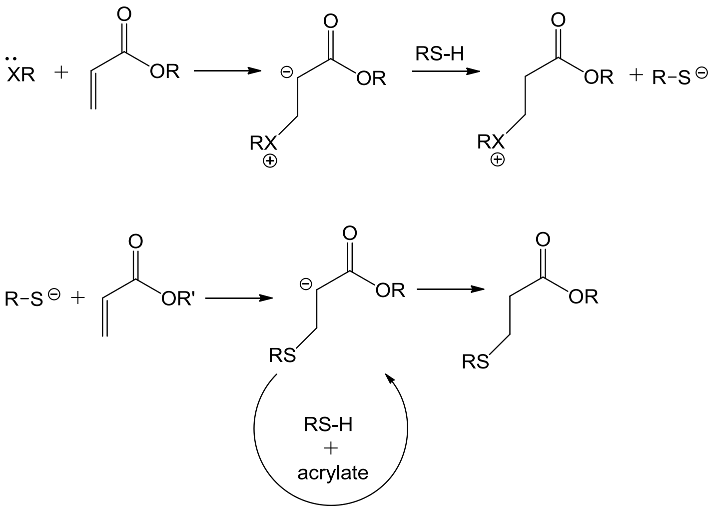

*Figure 5*. Thiol-Michael addition of a thiol to an acrylate in the presence of a nucleophile.[20]

*Network Development Using Multifunctional Monomers*

Shown in the previous sections, acrylate and thiol-ene polymerizations have numerous benefits which make them useful in various applications. One issue with both systems is the inability to produce linear polymers of sufficient molecular weight using UV polymerization. Acrylates are limited by the array of termination mechanisms. Thiol-ene polymers, given A-A B-B difunctional monomers, show step growth characteristics where molecular weight is widely disperse and low relative to chain growth products. Therefore, multifunctional monomers with a functionality of greater than one, for acrylate systems, and greater than two for thiol-ene systems are required to develop robust UV-cured polymers.

## Gas Transport in Polymeric Materials: Theories, Methods, and Analysis

The transport of small molecules in polymeric materials resulting from a difference in partial pressures on opposing sides of a membrane is commonly described by the solution diffusion model where small molecule gasses first sorb into the material, diffuse through free volume holes of sufficient size and desorb on the lower pressure side. Barrer described this phenomenon using the equation $P = D * S$ where *P* is the permeability coefficient, *D* is the diffusion coefficient and *S* is the solubility coefficient.[30] A cartoon schematic of the solution-diffusion model is presented in Figure 6.

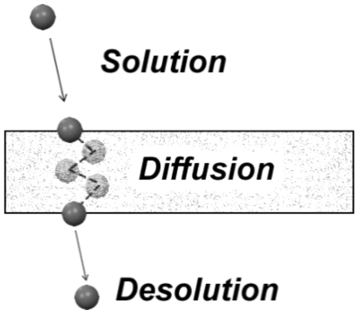

*Figure 6*. Schematic of a light gas dissolving into the upstream, diffusing through, and desorbing from the downstream surface of the polymer film.

Permeability is a proportionality coefficient that describes the number of gas molecules that permeate a thickness, *l*, across a partial pressure drop, *Δp*, at a constant flux, *J*. The diffusion coefficient describes the random walk of small molecule gasses through a polymer film with the total jump length, *l (i.e film thickness)*, and a time lag, *θ*. The solubility coefficient is the Henry's law constant for a given gas-polymer pair describing the amount of gas sorbed, *C*, into a polymer at a given external pressure, *p*.

Equation 2: $$P = \frac{J \cdot l}{\Delta p} \qquad D = \frac{l^2}{6 \cdot \theta} \qquad S = \frac{C}{p}$$

In amorphous regimes, the diffusion process of light gases is considered to be a random walk of jumps between free volume elements of sufficient size at a given distance apart. In semicrystalline polymers, diffusion processes are impacted by crystalline domains and are known to both hinder diffusion by creating a tortuous path and promote diffusion via channeling.[31] These phenomena are illustrated in Figure 7. It is widely accepted that the crystalline regions of semicrystalline polymers such as polyethylene, are impermeable, resulting in a decrease in permeability caused by diffusion of molecules through a tortuous path and the presence of crystals decreasing the relative total volume of polymer accessible to gas molecules.

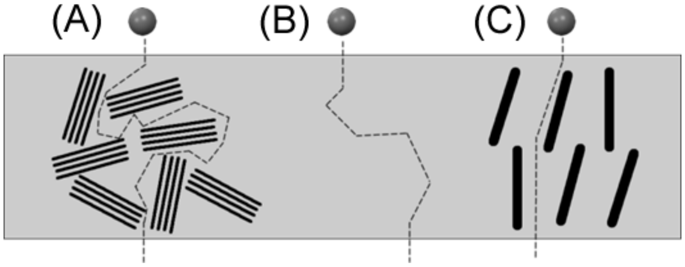

*Figure 7*. Three different paths of gas diffusion: A) diffusion through a tortuous path, B) random walk diffusion, C) directed or channeled diffusion.

*Constant Volume Variable Pressure*

The study of transport phenomena of light gases in a polymer membrane can be performed using various techniques.[32] The constant volume variable pressure (CVVP), or diffusion lag, technique allows for the determination of all three transport properties, $P$, $D$, and $S$, from one single experiment.[30,33] CVVP tests are based on the application of high pressure gas to the upstream side of a polymeric film and collecting penetrant gas in a downstream vessel of a calibrated volume. The pressure increase as a function of time is recorded using a differential pressure transducer where the reference pressure is high vacuum. Figure 8 shows typical CVVP data collected on a polymer membrane. As gas sorbs into the upstream surface, diffuses through, and desorbs on the downstream side of the membrane, pressure in the downstream slowly increases until a steady state pressure increase versus time, $dp_1/dt$, is achieved. Steady state pressure increases are fit using a standard linear regression. The permeability coefficient is calculated using:

$$\text{Equation 3:} \quad P = \frac{V_d l}{p_2 ART}\left[\left(\frac{dp_1}{dt}\right)_{ss} - \left(\frac{dp_1}{dt}\right)_{leak}\right]$$

where $P$ is permeability, $V_d$ is the downstream volume, $l$ is the film thickness, $A$ is the film area exposed to the permeate gas, $R$ is the gas constant, and $T$ is the absolute temperature. [33,34] The linear extrapolation of the steady state pressure region of the curve can be used to determine the time lag, θ, used to calculate the diffusion coefficient according to Equation 2. Applying the solution diffusion theory, the solubility of a gas can therefore be determined using $S = P/D$.

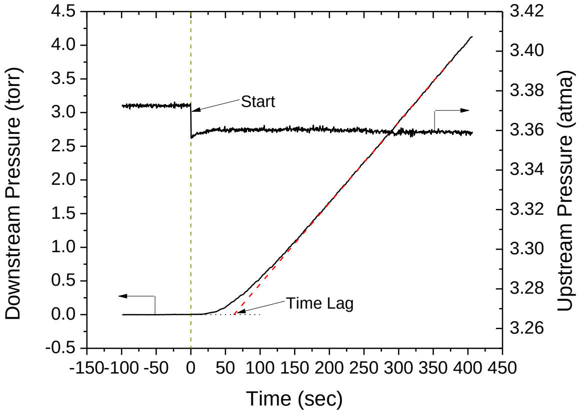

*Figure 8.* A standard downstream and upstream pressures as a function of time collected during a CVVP test.

Figure 9 shows a schematic of the instrument used in our lab which is based on Pye's description of the instrument.[33] In this experimental setup, there are two sample cells to allow for the testing of two sample films after each degasing stage. Each sample must be degased sufficiently after testing to ensure the films are free of any residual gas from previous tests. Degasing commonly occurs over night or for greater than 12 hours.

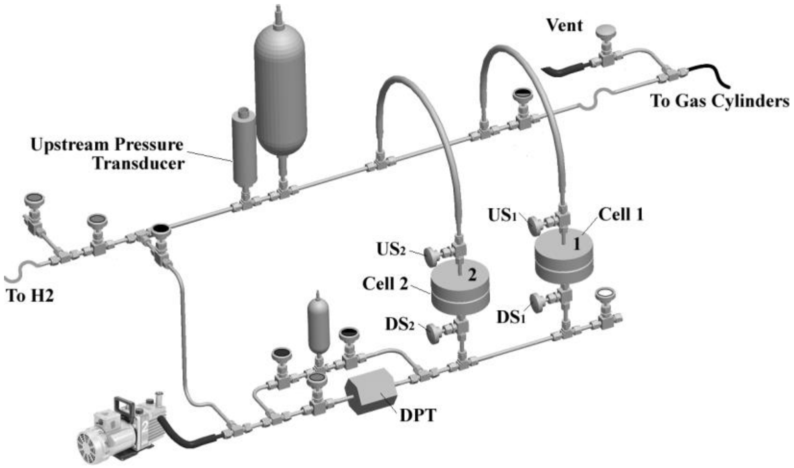

*Figure 9*. Schematic of a constant volume variable pressure apparatus.

## Free Volume in Polymeric Materials: Theories, Methods and Analysis

### *Free Volume in Polymeric Materials*

Free volume is described as the interstitial, unoccupied space in a polymer system. Free volume is best known to impact chain mobility and therefore various properties including aging, mobility, and small molecule diffusion. Specifically, the diffusion of light gases is predicted to be impacted by the fractional free volume using

Equation 4 $$D = D_0 * \exp\left(-\frac{B}{v_f}\right)$$

where $D$, as defined earlier, is the diffusion coefficient, $D_0$ is the diffusion coefficient when there are holes of sufficient size, $B$ is related to the molecular volume of the penetrant and $v_f$ is the average free volume. The exponential term describes the probability of a hole of sufficient size.[35]

Diffusion of a molecule is zero unless there is a free volume element of sufficient size to jump into.[35] Therefore, there is great need to understand the nature of free volume in order to develop membranes with high flux or controlled diffusion.

Volume of a polymer can be described by the sum of occupied and unoccupied, free volume.[36]

Equation 5 $$V_{sp} = V_{occ} + V_f$$

where $V_{occ}$ is the occupied volume and $V_f$ is the specific free volume. Furthermore, $V_f$, can be described by a concentration, $N'_h$, and size of free volume holes $\langle v_h \rangle$:

Equation 6 $$V_{sp} = V_{occ} + N'_h \langle v_h \rangle$$

$V_{sp}$ and $\langle v_h \rangle$ are determined using pressure volume temperature dilatometry, PVT, and positron annihilation lifetime spectroscopy, PALS, respectively. The fractional free volume is determined from the ratio of free volume to the total free volume.

Equation 7 $$FFV = \frac{(V_{sp} - V_{occ})}{V_{sp}}$$

As seen through Equations 5, 6, and 7, a knowledge of the free volume hole size or the occupied volume alone does not shed light on the volumetric behavior of a polymer. To fully understand free volume behavior, one must study both the hole size and the volumetric fraction of free volume. For example, Figure 10 shows three representative cells where the white holes represent unoccupied cells and the total free volume is equal. While all three of these systems maintain a similar FFV, the hole size is vastly different. To study the free volume properties of polymers a combination of positron annihilation lifetime spectroscopy and pressure volume temperature dilatometry are required.

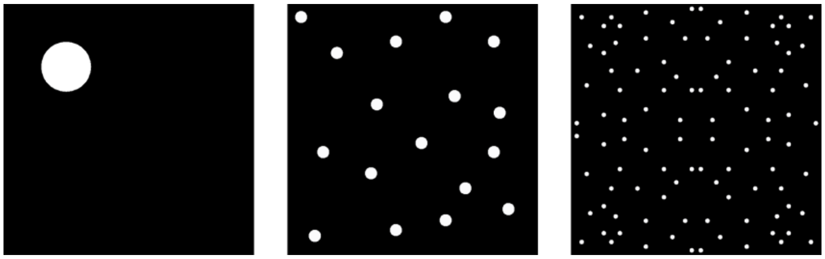

*Figure 10*. Schematic of a unit area with similar fractional free volumes (white) only differing by the size of holes.

### *Pressure-Volume-Temperature High Pressure Dilatometry (PVT)*

The volume and mass  of a material are the most fundamental properties of a material and dictate nearly all performance properties of a material.[37]  The measurement of mass is simple and there are various highly advanced methods to determine mass accurately. Determination of volume to a high degree of accuracy is not as straight forward. Several methods allow for the estimation of the temperature dependence of volume such as thermal mechanical analysis and picnometry but these techniques do not give a full understanding of the temperature and pressure dependence of volume.  One method that allows for full volumetric analysis of a polymeric sample is the use of a push rod dilatometer.[38] Zoller developed a mercury dilatometer specifically for polymeric materials using mercury as the confining fluid.[39] This dilatometer allows for the measurement of volume change as a function of pressure and temperature. The resulting data allows for the calculation of specific volume, expansivity, compressibility, bulk modulus, occupied volume, and fractional free volume. Figure 11 shows the data collected from a standard isothermal run at pressures from 10 MPa to 150 MPa and in the temperature range of 30 °C to 200 °C. 0

MPa extrapolations are performed within the Gnomix software using Tait equations and are accurate to within ± 0.0015 cm³/g.[39]

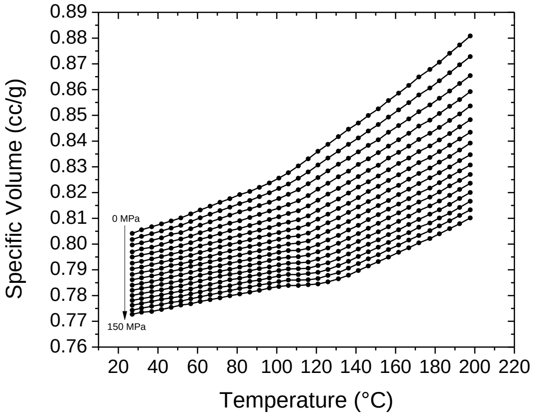

*Figure 11*. Raw $V_{sp}$ versus temperature data from PVT.

In order to exploit the full utility of PVT experimentation and data, several common analysis techniques are utilized to determine volumetric behavior in polymeric systems. For example, data collected on PVT is commonly fit using the Simha-Somcynsky Equations of State (SS-EOS) which allows for the prediction of equilibrium states below melting and glass transition temperatures. Figure 12 shows characteristic 0 MPa data for a typical glassy polymer with a $T_g$ of 100 °C fit with SS-EOS. A brief explanation of this method is highlighted by Utracki and will be explained here.[40]

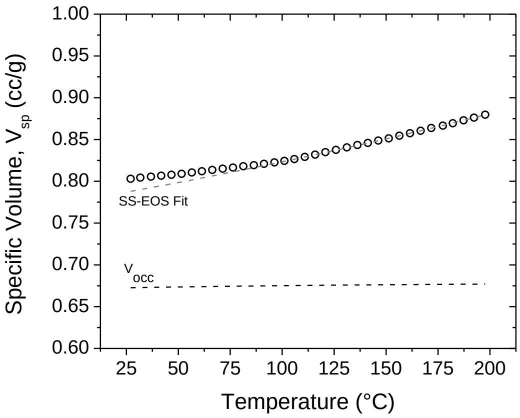

*Figure 12*. Specific volume data (○) for 0 MPa fit with SS-EOS and the calculated occupied volume

The PVT behavior of many amorphous fluorinated linear polymers[41,42] has been described by a simplified equation of state by Utracki and Simha[43] in the equilibrium melt state using

Equation 8 $$V(P,T) = V^* * exp\left(a_0 + a_1(\tilde{T})^{\frac{3}{2}} + (\tilde{P})\left[a_2 + \left(a_3 + a_4(\tilde{P}) + a_5(\tilde{P})^2\right) * (\tilde{T})^2\right]\right)$$

Equation 9 $$\tilde{P} = \frac{P}{P^*} \quad \tilde{T} = \frac{T}{T^*} \quad \tilde{V} = \frac{V}{V^*}$$

where $\tilde{P}$, $\tilde{T}$, and $\tilde{V}$ are reduced parameters and $P^*$, $T^*$, and $V^*$ are fit parameters.[41] Constants $a_0$ through $a_5$ are described as $a_0$= -0.10346, $a_1$= 23.854, $a_2$= -0.1320, $a_3$= -33.7, $a_4$= 1032.5, $a_5$= -1329.9.[43] The conventional method to fit $V_{sp}$ data from PVT experiments at ambient conditions is to consider $P$ = 0 MPa and therefore $\tilde{P}$ = 0 reducing SS-EOS to[40,43,44]

Equation 10 $$V(P,T) = V^* * exp\left(a_0 + a_1\left(\frac{T}{T^*}\right)^{\frac{3}{2}}\right)$$

Figure 13 shows a typical *ln(V)* dependence on the reduced temperature, $T^{3/2}$. From this plot V* and T* can be determined from the slope and intercept as shown in Equations 11 and 12.

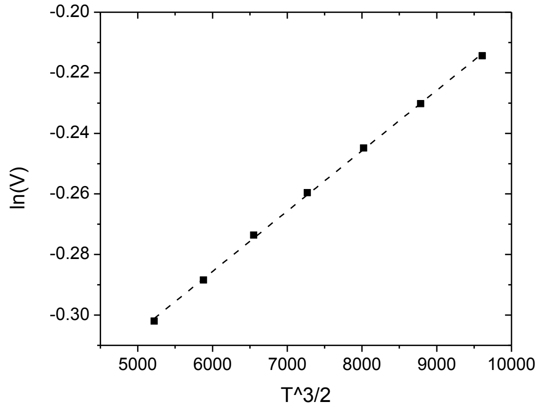

*Figure 13.* A standard linear regression of ln(V) v. $T^{3/2}$ data used to determine V* and T*.

Equation 11 $intercept = ln\,(V^*) - a_0$

Equation 12 $slope = a_1 * \left(\frac{1}{T^*}\right)^{\frac{3}{2}}$

To determine P*, both T* and V* are held constant across all high pressure isobars and a least squares fit was applied to Equation 8. As performed by Dlubek,[41] an average P* was determined from individual P* least squares fits and applied to all isobars.

Using the SS-EOS, it is possible to estimate the occupied fraction of lattice sites in these networks using[41]

Equation 13 $\frac{\tilde{P}\tilde{V}}{\tilde{T}} = \left[1 - y\left(2^{\frac{1}{2}}\, y\, \tilde{V}\right)^{-\frac{1}{3}}\right]^{-1} + \frac{y}{\tilde{T}}\left[2.002\left(y\,\tilde{V}\right)^{-4} - 2.409\left(y\,\tilde{V}\right)^{-2}\right]$

where y is the fraction of occupied lattice sites. Fractional free volume is determined using Equation 7 where $V_{occ} = V_{sp} * h$.

Further analysis of PVT surface data can yield the volumetric thermal expansivity, isothermal compressibility and its inverse, bulk modulus, and the internal pressure. From the PVT surface, volumetric thermal expansivity, $\alpha$, isothermal compressibility, $\beta$, and internal pressure, $P_i$, are determined using

$$\text{Equation 14} \quad \alpha \equiv \frac{1}{V}\left(\frac{\partial V}{\partial T}\right)_p \qquad \beta \equiv -\frac{1}{V}\left(\frac{\partial V}{\partial p}\right)_T$$

$$\text{Equation 15} \quad P_i = T\left(\frac{\alpha}{\beta}\right) - p$$

where $p$ is the applied external pressure. From the PVT surface, the partial derivative $(\partial V/\partial T)_p$ was determined by treating the melt state temperature dependence of $V_{sp}$ as linear for each pressure. To determine $(\partial V/\partial p)_{T,}$ the melt state nonlinear pressure dependence of $V_{sp}$ was fit with a second order polynomial and the partial derivative was determined at each temperature.

As shown briefly here, the analysis of PVT surfaces from a single PVT isothermal run can yield a plethora of information on the volumetric behavior of a system. This cornucopia of volumetric data makes the laborious task of cleaning the sample chamber, dealing with mercury, and running the complex experimental procedure worth the effort for well thought out experiments.

### *Positron Annihilation Lifetime Spectroscopy (PALS)*

Positron annihilation lifetime spectroscopy is a spectroscopic technique that allows the probing of free volume elements in a polymer sample. The decay products of radioactive $Na^{22}$ are a single gamma quanta at 1.28 MeV and a positron, $e^+$. The gamma quanta is detected by a photomultiplier tube (PMT), $BaF_3$ assembly tuned with a constant fraction discriminator (CFD) and is used to signify the "birth" of o-Ps.[45] In a polymer sample, positron couples with an electron to yield an ortho-Positronium atom with a radius similar to that of a hydrogen atom, 0.529 Å. In vacuum, o-Ps has an intrinsic lifetime of 142 ns but in condensed matter, such as polymers, the life time is reduced to a few nanoseconds or less. Upon the decay, or "death" of o-Ps, caused by a pick-off of the positron by an electron in the surrounding medium, two gamma quanta at 0.511 MeV are emitted and detected by a second tuned PMT assembly. The time between the "birth" and "death" signals is recorded using time-to-amplitude converter (TAC) and compiled using a multi-channel analyzer (MCA). The frequency of these lifetime events is plotted as counts as a function of lifetime as shown in Figure 14. Typical spectra are collected over one hour and the instrument is tuned to collect > $10^6$ counts over that period of time. Figure 15 shows a typical PALS setup with temperature control capabilities with the photo multipliers aligned with the sample and a general schematic of the fast-fast coincidence system.

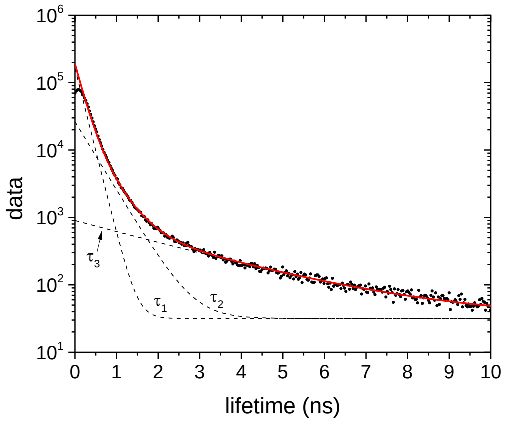

*Figure 14.* Typical PALS spectrum of the frequency of an event v. the lifetime of that event.

Typical samples for PALS are thin films or sheets of polymer of 10 mm in diameter. The minimum sample thickness is estimated to be 1 mm to ensure all

Ps are annihilated within the polymer sample and not in the surrounding media. Two disks are prepared with a final dimension of greater than 1 mm x 10mm diameter. For thin films, multiple films can be stacked together to 1 mm and then wrapped in aluminum foil. A foil wrapped $Na^{22}$ source packet is sandwiched between the two sample disks, held together with a non-adhesive Teflon tape. The sandwich is then placed in the sample chamber, between the PMTs.

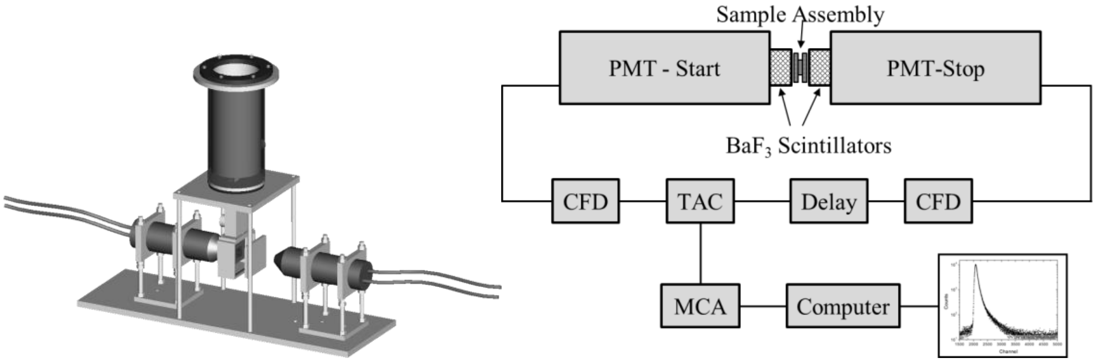

*Figure 15*. Schematic of a typical PALS instrument setup with a dewar for temperature control. The schematic shows the different components of a typical spectrometer.

A typical PALS spectrum includes the lifetime contributions of three different positronium (Ps) events: the short lived para-Positronium, free positron annihilation, and the long lived ortho-Positronium. The deconvolution of the three lifetime contributions from a spectrum is performed using PATFIT-88 software[46] which outputs the average life time and relative fraction of positrons that annihilate from each of these Ps events. The resulting lifetimes ($\tau_1$, $\tau_2$, and $\tau_3$) and intensities ($I_1$, $I_2$, and $I_3$) are reported. Since the first two Ps events occur at lifetimes much shorter than the long lived o-Ps, polymer data analysis focuses on the o-Ps lifetime and intensity, $\tau_3$ and $I_3$. Eldrup and Tao correlated $\tau_3$ with void volumes in zeolite membranes with the assumption that the voids are spherical.

[47,48] The radius of a free volume element, *R*, is predicted using a constant $R_o$ and the experimentally determined $\tau_3$:

$$\text{Equation 16} \quad \tau_3 = \frac{1}{2}\left[1 - \frac{R}{R_o} + \frac{1}{2\pi}\sin\left(\frac{2\pi R}{R_o}\right)\right]^{-1}$$

## Conclusions

The breadth of study covered in this document is evidenced by the broad nature of the background given. This work covers the development of new perfluorinated materials with an aim to impact the transport of light gases through the membrane. Specifically, UV-cured thiol-ene and acrylate networks were developed and studied for their thermal, morphological, transport and free volume properties. Chapters II[29], III[49], IV[50], and V cover UV-cured thiol-ene networks were modified with perfluorinated and silane acrylates to induce high free volume and therefore high gas permeability. Chapters VI[51] and VII[52] explore the side chain liquid crystalline morphology of perfluorinated acrylate polymers for permeability switching behavior through the thermotropic transition.

## References

(1) Baker, R. W. Industrial & Engineering Chemistry Research **2002**, 41, 1393.

(2) Budd, P. M.; McKeown, N. B. Polymer Chemistry **2010**, 1, 63.

(3) Bernardo, P.; Drioli, E.; Golemme, G. Industrial & Engineering Chemistry Research **2009**, 48, 4638.

(4) Mukhopadhyay, A.; Midha, C. K. Journal of Industrial Textiles **2008**, 37, 225.

(5) Gebben, B. Journal of Membrane Science **1996**, 113, 323.

(6) Mukhopadhyay, A.; Vinay Kumar Midha Journal of Industrial Textiles **2008**, 37, 225.

(7) Bondar, V. I.; Freeman, B. D.; Pinnau, I. Journal of Membrane Science **2008**, 313, 263.

(8) Husken, D.; Gaymans, R. J. Journal of Applied Polymer Science **2009**, 112, 2143.

(9) Nicolson, P. C.; Vogt, J. Biomaterials **2001**, 22, 3273.

(10) Dylan, J. B. In Advances in Fluorine-Containing Polymers; American Chemical Society: 2012; Vol. 1106, p 1.

(11) O'Hagan, D. Chemical Society Reviews **2008**, 37, 308.

(12) Riess, J. G. Chemical Reviews **2001**, 101, 2797.

(13) Banks, R. E.; Tatlow, J. C. Journal of Fluorine Chemistry **1986**, 33, 227.

(14) Studer, K.; Decker, C.; Beck, E.; Schwalm, R. Progress in Organic Coatings **2003**, 48, 92.

(15) Decker, C. Polymer International **1998**, 45, 133.

(16) Wight, F. R. Journal of Polymer Science: Polymer Letters Edition **1978**, 16, 121.

(17) Decker, C. Marcel Dekker, Handbook of Polymer Science and Technology. **1989**, 3, 541.

(18) Ligon, S. C.; Husár, B.; Wutzel, H.; Holman, R.; Liska, R. Chemical Reviews **2013**.

(19) Hoyle, C. E.; Lee, T. Y.; Roper, T. Journal of Polymer Science Part A: Polymer hemistry **2004**, 42, 5301.

(20) Hoyle, C. E.; Bowman, C. N. Angewandte Chemie International Edition **2010**, 49, 1540.

(21) Kolb, H. C.; Finn, M. G.; Sharpless, K. B. Angewandte Chemie International Edition **2001**, 40, 2004.

(22) Cramer, N. B.; Scott, J. P.; Bowman, C. N. Macromolecules **2002**, 35, 5361.

(23) Hoyle, C. E.; Bowman, C. N. Angewandte Chemie **2010**, 122, 1584.

(24) Hoyle, C. E.; Lowe, A. B.; Bowman, C. N. Chemical Society Reviews **2010**, 39, 1355.

(25) Nair, D. P.; Podgórski, M.; Chatani, S.; Gong, T.; Xi, W.; Fenoli, C. R.; Bowman, C. N. Chemistry of Materials **2013**.

(26) Kwisnek, L.; Nazarenko, S.; Hoyle, C. E. Macromolecules **2009**, 42, 7031.

(27) Clark, T.; Kwisnek, L.; Hoyle, C. E.; Nazarenko, S. Journal of Polymer Science Part A: Polymer Chemistry **2009**, 47, 14.

(28) Kwisnek, L.; Kaushik, M.; Hoyle, C. E.; Nazarenko, S. Macromolecules **2010**, 43, 3859.

(29) Goetz, J.; Kwisnek, L.; Nazarenko, S. RadTech Report **2012**, 27, 27.

(30) Barrer, R. M.; Rideal, E. K. Transactions of the Faraday Society **1939**, 35, 628.

(31) Hodge, K.; Prodpran, T.; Shenogina, N. B.; Nazarenko, S. Journal of Polymer Science Part B: Polymer Physics **2001**, 39, 2519.

(32) In Springer Handbook of Materials Measurement Methods; Horst Czichos, T. S., Leslie Smith, Ed.; Springer Science+Business Media Inc: 2006; Vol. 1, p 371.

(33) Pye, D. G.; Hoehn, H. H.; Panar, M. Journal of Applied Polymer Science **1976**, 20, 1921.

(34) Lin, H.; Freeman, B. D. Journal of Membrane Science **2004**, 239, 105.

(35) Cohen, M. H.; Turnbull, D. The Journal of Chemical Physics **1959**, 31, 1164.

(36) Dlubek, G.; Stejny, J.; Alam, M. A. Macromolecules **1998**, 31, 4574.

(37) Van Krevelen, D. W.; Te Nijenhuis, K. In Properties of Polymers (Fourth Edition); Krevelen, D. W. V., Nijenhuis, K. T., Eds.; Elsevier: Amsterdam, 2009, p 71.

(38) Buck, W.; Rudtsch, S. In Springer Handbook of Materials Measurement Methods; Czichos, H., Saito, T., Smith, L., Eds.; Springer Berlin Heidelberg: 2006, p 399.

(39) Zoller, B., Pahud, Ackermann Review of Scientific Instruments **1976**, 47, 948.

(40) Utracki, L. A.; Jamieson, A. M. Polymer Physics: From Suspensions to Nanocomposites and Beyond; Wiley, 2011.

(41) Dlubek, G.; Sen Gupta, A.; Pionteck, J.; Krause-Rehberg, R.; Kaspar, H.; Lochhaas, K. H. Macromolecules **2004**, 37, 6606.

(42) Dlubek, G.; Pionteck, J.; Sniegocka, M.; Hassan, E. M.; Krause-Rehberg, R. Journal of Polymer Science Part B: Polymer Physics **2007**, 45, 2519.

(43) Utracki, L. A.; Simha, R. Macromolecular Theory and Simulations **2001**, 10, 17.

(44) Dlubek, G.; Pionteck, J. Acta Physica Polonica A **2008**, 113, 1331.

(45) Pethrick, R. A. Progress in Polymer Science **1997**, 22, 1.

(46) Kirkegaard, P.; Eldrup, M.; Mogensen, O. E.; Pedersen, N. J. Computer Physics Communications **1981**, 23, 307.

(47) Tao, S. J. Journal of Chemical Physics **1972**, 56.

(48) Eldrup, M.; Lightbody, D.; Sherwood, J. N. Chemical Physics **1981**, 63, 51.

(49) Goetz, J.; Wislinsky, E.; Nazarenko, S. In Forty-First Annual International Waterborne, High-Solids, and Powder Coatings Symposium New Orleans, LA, 2014.

(50) Goetz, J.; Greenhoe, B.; Kwisnek, L.; Nazarenko, S. Manuscript in Preparation **2014**.

(51) Goetz, J.; Nazarenko, S. J Coat Technol Res **2013**, 1.

(52) Goetz, J.; Kwisnek, L.; Nazarenko, S. Manuscript in Preparation **2014**.

# CHAPTER II

# FROM GAS BARRIERS TO HIGH GAS FLUX MEMBRANES: UV-CURED THIOL-ENE NETWORKS FOR A BROAD RANGE OF TRANSPORT APPLICATIONS

## Introduction

The success of UV-curing has been largely determined by its inherent advantages such as high reactive efficiency, eco-friendly formulations that do not emit volatiles, and the possibility of using a variety of processing techniques, i.e. spraying, dipping, or rolling of a reactive mixture on a substrate prior to curing which occurs in seconds with UV light. [1,2] The majority of UV-cured materials used commercially today are acrylates which form network polymers via a UV-initiated, free-radical chain-growth polymerization mechanism. However, acrylates typically suffer from two inherent drawbacks: shrinkage and oxygen inhibition. Like in acrylates, network formation in thiol-enes often requires free-radicals which can be UV-initiated. However, the polymerization mechanism is very different. Polymerization of thiol-enes is a step-growth radical reaction as shown in Figure 16 with a chain transfer step in which carbon-centered radicals abstract hydrogen from thiols thus regenerating thiyl radicals which continue the polymerization process.[3,4] Benefiting from this unique mechanism thiol-ene reactions are practically insensitive to oxygen inhibition. It should be noted here that depending on the electronic character of the ene, the thiol-ene reaction may also proceed via a nucleophile-catalyzed anionic mechanism. The nucleophile-catalyzed anionic addition, called thio-Michael addition, proceeds with electron poor double bonds such as acrylates.[5]

Thiol-ene networks have been widely studied and are known for their low shrinkage, narrow glass transitions, and overall uniformity as compared to traditional photopolymerized networks. Modularity is another strong advantage of thiol-ene networks. A variety of commercially-available thiol and ene monomers are available. By mixing and matching these components, properties can be tuned to meet specific requirements. The synthesis of new and chemical modification of the existing monomers open up further possibilities.

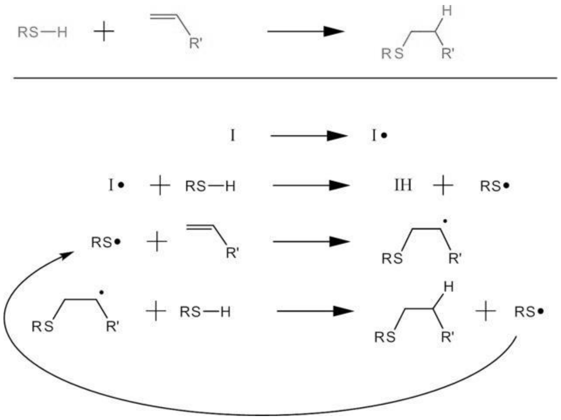

*Figure 16.* Free-radical, step-growth thiol-ene mechanism. This mechanism proceeds for any thiol and any ene, initiated typically with UV light and a photoinitiator (I). Net reaction shown in red/blue.

UV curable materials have a broad range of applications.[2] However most often they have been used as coatings, adhesives, and inks in printing. UV curing has not been widely employed in the gas barrier and membrane fields where the modern market, as never before, has a strong need for advanced food and electronic packaging materials with the bottom line of cost and barrier efficiency, improved protective coatings, as well as high gas permeable polymeric systems which can be employed in the area of gas separation, purification, contact lenses applications, medical related fields, and breathable clothing.[6]

Transport of small gas molecules strongly depends on the amount of free volume. Free volume, or unoccupied void space between molecules, allows hopping of gas molecules through a polymer. In the rubbery or molten state free volume is dynamic, able to get readily redistributed while in the glassy state it is mainly frozen in.  As related to the structure of a polymer, free volume is controlled by chain rigidity and secondary forces. Rigid, high $T_g$ polymers, examples include polyimides,  polysulfones, and polycarbonates exhibit high free volume and often are used as gas separations membranes in which high gas permeability is important in addition to selectivity.[7,8] Polymers with strong secondary forces, i.e. dipole-dipole interactions and hydrogen bonding, are known to exhibit tight packing (low free volume) and listed as high gas barriers: examples include polyacrylonitrile, poly(styrene-co-acrylonitrile), poly(vinylidene chloride), poly(vinyl alcohol), and some polyamides.[9]

Finding a unique material platform based on  similar chemistry route which would allow to control free volume and gas transport characteristics within broad limits has been the goal of our research group for some time. We demonstrated that thiol-ene based chemistries can be conveniently employed to have such control over free volume and gas permeability.[10,11]

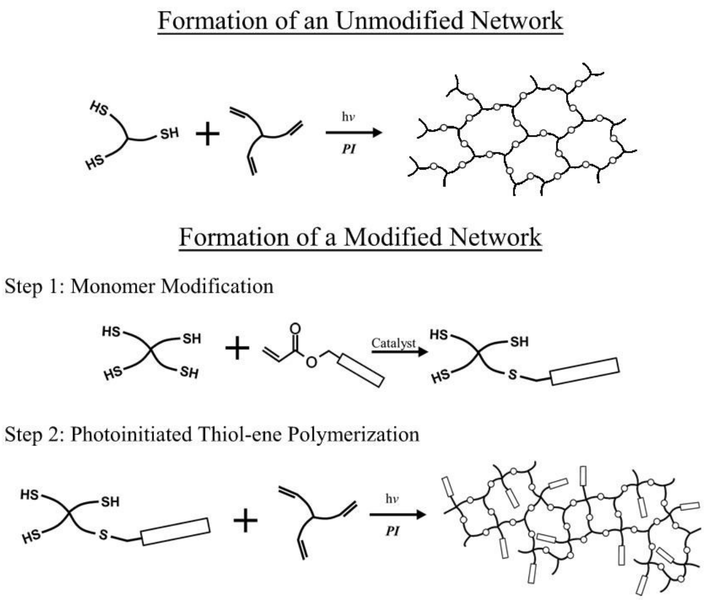

*Figure 17***.** Formation of modified and unmodified networks.

This report aims to highlight the methods and advancements made in the modification of thiol-ene networks for the development of high barrier and high flux materials. A baseline of gas transport properties for commercially-available UV curable thiol-ene networks was established in this project first providing a starting point window of gas permeation in thiol-ene networks. After these initial attempts further efforts were made to expand the window by employing the thiol-acrylate Michael addition reaction. Multifunctional thiols were first derivatized via nucleophile-catalyzed thio-Michael addition reaction using a broad range of commercially available functionalized monoacrylates. Cyano, hydroxyl, amide, as well as n-alkyl and fluoroalkyl chemical moieties were explored. Then modified thiol-ene networks were formed by polymerization of the derivatized thiols with ene monomer under UV-light. Figure 17 shows formation of unmodified and modified thiol-ene networks both displaying trifunctional junction points. Combining the processing simplicity of UV curing and the well-defined and robust thiol-ene modification reactions, this research project reports the first steps toward understanding controlling factors for gas transport in photopolymerized thiol-ene networks.

## Experimental

### *Preparation of Basic and Modified Thiol-Ene Networks*

Commercially available, thiol and ene structures are shown in Figure 18. Tri and tetra functional thiol monomers: trimethylolpropane tris(3-mercaptopropionate) (3T), tris[2-(3-mercaptopropionyloxy)ethyl] isocyanurate (3TI), pentaerythritol tetrakis(3-mercaptopropionate) (4T), and di and tri functional ene monomers: tri(ethylene glycol) divinyl ether (TEGDVE), pentaerythritol allyl ether (TAE), 2,4,6-triallyloxy-1,3,5-triazine (TOT), and triallyl-1,3,5-triazine-2,4,6(1*H*,3*H*,5*H*)-trione (TTT).

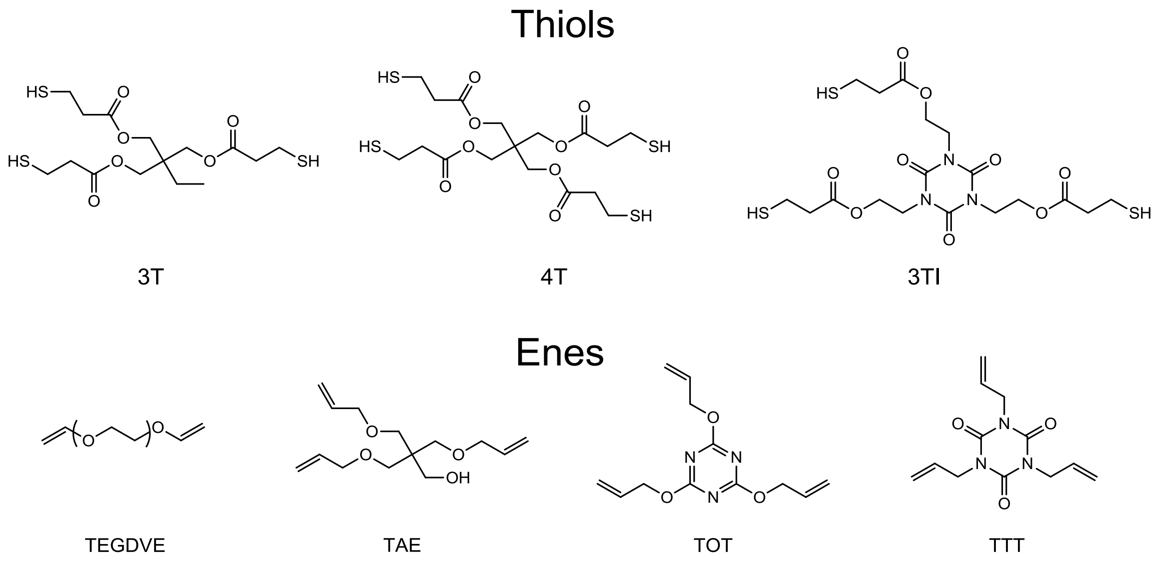

*Figure 18*. Commercially available thiols and enes.

Modified tri-functional thiol monomer was synthesized using an amine-catalyzed (diethylamine or dibutylamine) thio-Michael addition reaction between 4T and various functionalized monoacrylates shown in Figure 19 at a 1:1 molar ratio so as to cap an average of one of the four thiol groups per monomer. The final monomer should be a statistical distribution of structures with the trifunctional monomer being predominant.  It is noted that the distribution could result in small changes in the macroscopic physical properties of the final networks versus networks formed from a purely trifunctional system. Derivatized thiol monomers were characterized by $^1$H NMR.

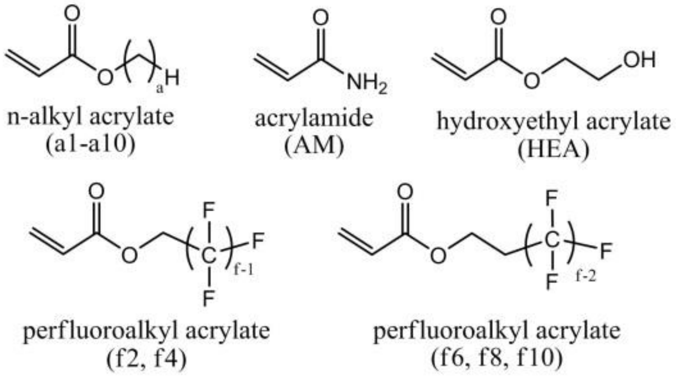

*Figure 19*. Chemical structures of modifying acrylates.

All studied basic and modified thiol monomers were readily miscible with ene monomers with only mild sonication, resulting in optically clear, homogeneous liquid mixtures.  Free-standing thin films of all thiol-ene network formulations were made by dissolving 1 wt% 1,1-dimethoxy-1-phenylacetophenone (Irgacure 651) photoinitiator into the thiol-ene mixture. This homogeneous mixture was then drawn down onto glass substrates using drawdown bars. Films were cured using a Fusion UV curing line with a D bulb (400 W/cm$^2$ with belt speed of 3 m/min and 3.1 W/cm$^2$ irradiance). Network conversion was monitored by FTIR. Change in peak area of thiol –SH groups at 2570 cm$^{-1}$ (S-H stretch) and ene C=C groups at 3080 cm$^{-1}$ (vinyl C-H stretch) were measured. Thiol and ene functional groups proceed in seconds to high conversion (70->90%) at room temperature, and thiol and ene conversions, in all cases, progressed simultaneously, indicative of a predominance of the thiol-ene reactions over the ene homopolymerization. Films shown in Figure 20 were all transparent and free of any defects such as bubbles or pin holes. Narrow tanδ at $T_g$ was indicative of compositional and structural homogeneity of the basic and modified networks.

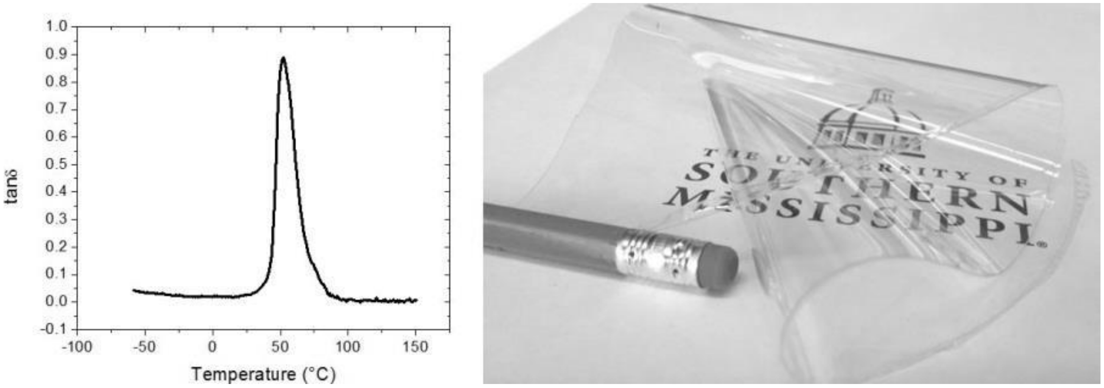

*Figure 20***.** (Left) Narrow Tg of thiol-ene networks measured by DMTA. (Right) UV-Cured thiol-ene films are transparent, robust and malleable.

*Oxygen Barrier and Free Volume Measurements*

Oxygen is the most widely investigated permeant gas in polymeric materials. It is vital contaminant of foods and beverages, a detriment to medical and electronic devices, and an important component in technologies such as air enrichment.[9,12] Oxygen permeation tests were conducted on MOCON OX-TRAN® 2/21 instruments using a continuous-flow testing cell method (ASTM D3985). All measurements were conducted at 23 °C and 0% RH. When oxygen flux was too high to measure with MOCON, a constant volume variable- pressure (ASTM D1434-82) custom built apparatus was employed. The experimental methodologies are described elsewhere.[13,14] Positron annihilation lifetime spectroscopy (PALS) is widely used in the characterization of free volume of polymers.[15] PALS involves measurements of the lifetime of positrons injected into a polymer sample from a positron-emitting nucleus, generally $Na^{22}$. The lifetime ($\tau_3$) of the long-lived orthopositronium (positron/electron pair) o-Ps species were used to extract information about the average size of molecular holes. The o-Ps lifetime ($\tau_3$) can be related to the radius of a spherical cavity. The average free volume of a hole ($V_h$) can then be calculated as $V_h=4/3\pi R^3$.

## Results and Discussion

In order to establish a baseline in properties, the oxygen transport characteristics of basic thiol-ene films were evaluated. These basic networks feature the 3T trifunctional thiol monomer copolymerized with four different ene monomers of varying functionality and rigidity: TEGDVE, TAE, TOT, TTT. TEGDVE, the least rigid monomer, is difunctional, while TAE, also a flexible monomer, is trifunctional. Isomeric TOT and TTT enes have basic triazine and isocyanurate structures and are more rigid trifuctional ene monomers. The trifunctional thiol 3TI and tetrafunctional 4T were also copolymerized with TTT to increase the network rigidity and the glass transition temperature. Oxygen permeability of the basic thiol-ene films measured at room temperature in units cc(STP) cm $m^{-2}$ $day^{-1}atm^{-1}$ varied broadly from 13.8 (3T-TEGDVE) to 0.021 (3TI-TTT). The lowest permeability observed for the basic networks corresponded to the oxygen barrier about tenfold better than that (0.38) for poly(ethylene terephthalate),[16] the most common resin used for carbonated drinks packaging. Oxygen permeability correlated remarkably well with $T_g$ for both the rubbery and glassy networks as shown in Figure 21. This correlation displayed a classic V-shape. The minimum in oxygen permeability was found for samples whose glass transitions were near room temperature. These samples exhibited a minimum in free volume. At room temperature rubbery and glassy networks with subsequently lower and higher $T_g$ in turn were more permeable. These samples exhibited maximums in free volume.

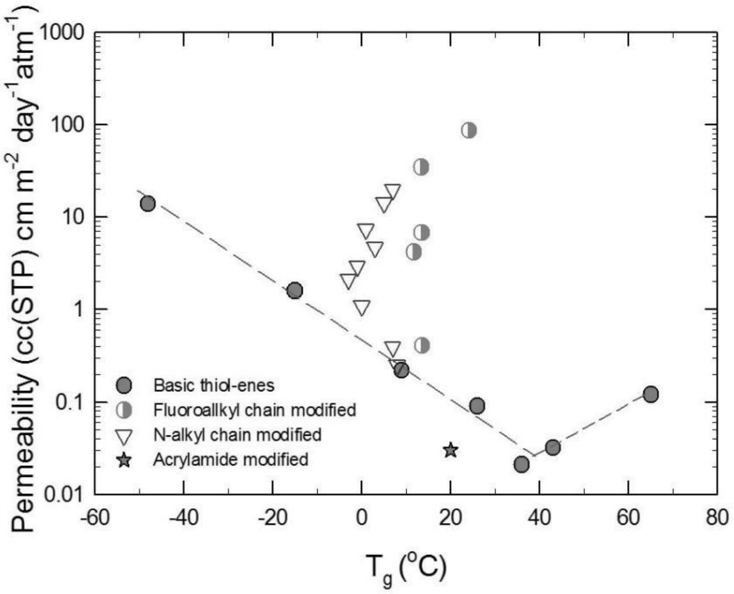

*Figure 21*. Oxygen permeability of basic and chemically modified thiol-ene networks.

Figure 21 also shows oxygen permeability behavior of the modified networks. Acrylamide modification of 4T-TTT network, as expected due to incorporation of strongly "attractive" moieties, led to noticeable (about one order of magnitude) reduction of oxygen permeability as compared to the basic thiol-ene systems with similar $T_g$. In contrast, incorporation of strongly *repulsive* moieties such as n-alkyl, and in particular fluroalkyl functional groups resulted in remarkable increases of oxygen permeability. This behavior was shown to depend strongly on alkyl chain length where the networks with longer alkyl units exhibited larger oxygen permeability. Up-to a three orders of magnitude increase of oxygen permeability was observed in our experiments.  Interestingly the glass transition temperature of the modified networks was practically independent on the alkyl chain length thus mainly defined by the cross link density of the backbone network which was similar in each case.

Probed by PALS, an increase in free volume size was anticipated from incorporation of n-alkyl and in particular fluoroalkyl moieties. Indeed a drastic increase of the molecular free volume size was observed for the modified networks as one can see on Figure 22. Similar to oxygen permeability free volume size showed a correlation with alkyl chain length. More than a twofold increase of free volume size, compared to basic thiol-ene systems, was possible to attain after n-alkyl chain modification and a fivefold increase after the incorporation of maximum length fluoroalkyl chain moieties.

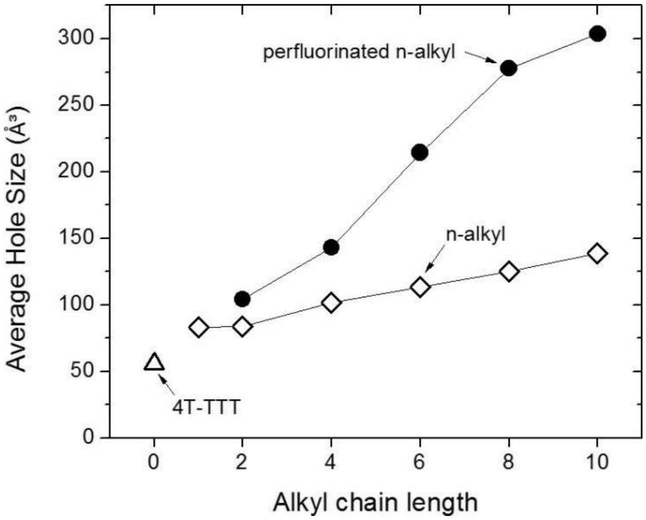

*Figure 22*. Average hole volume versus alkyl chain length for modified thiol-ene networks.

## Conclusions

Oxygen permeability was determined initially for a variety of photopolymerized thiol-ene networks. Such information, until now was absent from the literature despite its importance. Basic thiol-ene network formulations showed a broad range of oxygen permeabilities. Some of the networks were fairly oxygen permeable and some demonstrated an excellent oxygen barrier. Oxygen permeability of basic networks showed a correlation with Tg. Then an interesting approach based on thio-Michael addition of various functionalized acrylates to a tetrathiol monomer was employed to chemically modify the networks. This modification technique enabled a study on how different functional groups embedded in a uniform network affect oxygen barrier properties and free volume. Of particular interest was the introduction of primary amides, n-alkyl, and fluoroalkyl groups as dangling appendages which resulted in especially low and in contrast high gas permeability respectively. The use of thiol-ene networks as a platform to investigate the systematic effect of functional groups on network properties has far reaching implications. This method enables to tailor broadly gas transport characteristics for a variety of applications.

## References

(1) Hoyle Charles, E., Photocurable Coatings, in Radiation Curing of Polymeric Materials. 1990, American Chemical Society. p. 1-16.

(2) Fouassier, J.P., An Introduction to the Basic Principles in UV Curing in Radiation Curing in Polymer Science and Technoloy, J.P.R. Fouassier, J. F., Editor. 1993, Elsevier Applied Science: New York. p. 49-117.

(3) Hoyle, C.E., T.Y. Lee, and T. Roper, Thiol–enes: Chemistry of the past with promise for the future. Journal of Polymer Science Part A: Polymer Chemistry, 2004. 42(21): p. 5301-5338.

(4) Yagci, Y., S. Jockusch, and N.J. Turro, Photoinitiated Polymerization: Advances, Challenges, and Opportunities. Macromolecules, 2010. 43(15): p. 6245-6260.

(5) Hoyle, C.E. and C.N. Bowman, Thiol-En-Klickchemie. Angewandte Chemie, 2010. 122(9): p. 1584-1617.

(6) Koros William, J., Barrier Polymers and Structures: Overview, in Barrier Polymers and Structures. 1990, American Chemical Society. p. 1-21.

(7) Koros, W.J. and G.K. Fleming, Membrane-based gas separation. Journal of Membrane Science, 1993. 83(1): p. 1-80.

(8) Petropoulos J. H., Mechanisms and theories for sorption and diffusion of gases in polymers, in Polymeric Gas Separation Membranes, D.R. Paul, Yampol'skii, Editor. 1994, CRC Press: Ann Arbor. p. 17.

(9) Lange, J. and Y. Wyser, Recent innovations in barrier technologies for plastic packaging—a review. Packaging Technology and Science, 2003. 16(4): p. 149-158.

(10) Kwisnek, L., S. Nazarenko, and C.E. Hoyle, Oxygen Transport Properties of Thiol−Ene Networks. Macromolecules, 2009. 42(18): p. 7031-7041.

(11) Kwisnek, L., et al., Free Volume, Transport, and Physical Properties of n-Alkyl Derivatized Thiol−Ene Networks: Chain Length Effect. Macromolecules, 2010. 43(8): p. 3859-3867.

(12) Lagaron, J.M., R. Catalá, and R. Gavara, Structural characteristics defining high barrier properties in polymeric materials. Materials Science and Technology, 2004. 20(1): p. 1-7.

(13) Lin, H. and B.D. Freeman, Gas Permeation and Diffusion in Cross-Linked Poly(ethylene glycol diacrylate). Macromolecules, 2006. 39(10): p. 3568-3580.

(14) Sekelik, D.J., et al., Oxygen barrier properties of crystallized and talc-filled poly(ethylene terephthalate). Journal of Polymer Science Part B: Polymer Physics, 1999. 37(8): p. 847-857.

(15) Pethrick, R.A., Positron annihilation—A probe for nanoscale voids and free volume? Progress in Polymer Science, 1997. 22(1): p. 1-47.

(16) Pauly, S., Permeability and Diffusion Data, in Polymer Handbook, E.I. J. Brandrup, Editor. 1999, Wiley: New York.

# CHAPTER III

# MODIFICATION OF UV-CURED THIOL-ENE NETWORKS WITH INCOMPATIBLE MOIETIES

## Abstract

Thiol-ene materials have seen great growth in the past decade making them more interesting for various applications. As the field of thiol-ene research grows, the need for broadening the applicability of these materials has increased. Drawing on the advantages of UV-cured thiol-ene polymerizations, this research gives an overview of a two-stage modification technique that has allowed for an increase in the possible applications of thiol-ene networks as a result of covalently incorporating previously incompatible moieties into the network while retaining thermal properties such as Tg and rubbery modulus. The focus of this work will be silane modifications and their impact on properties such as free hole volume, light gas permeability, and static water contact angle. Applications include breathable coatings, contact lenses, and membranes.

## Introduction

Coatings cover a wide range of applications and therefore demand a wide breadth of properties. Breathable coatings require high transport properties whereas barrier coatings require low permeability.[1] Applications of such materials range in scope from medical devices and electronics to photovoltaics and protective garments worn by soldiers and athletes. Highly permeable membranes find utility in contact lenses, industrial mixed gas separation, and dehumidification applications.[2-4] Contemporary processing of thin films such as solution casting and thin film extrusion require high energy manufacturing techniques. Photo polymerization offers the benefit of fast cure times, no side products or waste, dimensional stability, low VOCs and flexibility in application requirements.

Thiol-ene chemistries have shown great growth over the past several years[1,5,6] with applications in optics, adhesives, micro devices, coatings, high impact polymers, liquid crystalline polymers, and polymer functionalization. Thiol-ene networks are a result of the polymerization of multifunctional (functionality greater than two) thiol and vinyl containing "ene" monomers. UV-cured thiol-ene networks have many advantages over traditional UV-cured acrylate polymers including low shrinkage, narrow glass transitions, low oxygen inhibition and near complete conversion of reactive functional groups. Low oxygen inhibition allows for one pot synthesis and solvent free, bulk polymerization. The ability to modify UV-cured thiol-ene networks through various techniques provides endless opportunities for new materials and manufacturing flexibility.

Shin et. al. first explored the chemical modification of thiol-ene networks with n-alkyl moieties using a two-step process.[7] Kwisnek et. al. extended this work and investigated the effect of alkyl chain length on oxygen permeability of thiol-ene networks.[8,9] A two orders of magnitude increase in oxygen permeability was observed as a result of increasing the length of the modifying side chains incrementally from methyl acrylate through hexadecyl acrylate. Further analysis indicated that increased oxygen permeability was a result of an increase of hole free volume as a function of n-alkyl chains length. Further study by our group included the modification of thiol-ene networks using perfluorinated acrylates in an attempt to incorporate incompatible moieties into the network.[10,11] Similar to aliphatic modifications, increased modifier chain length increased free volume and high permeability. While perfluorinated modified networks show great promise for applications such as contact lenses, biocompatibility issues and environmental concerns may limit their applicability. The current research aims to find alternative network modifications to increase oxygen permeability without perfluorinated compounds by introducing silane moieties as the modifier in thiol-ene networks.

## Experimental

### *Materials*

The backbone monomers for the thiol-ene network are shown in Figure 23. Thiol monomers pentaerythritol tetrakis(3-mercaptopropionate) (4T,PETMP) and trimethylolpropane tris(3-mercaptopropionate) (3T, TMPMA) were acquired from Bruno Bock chemical. “Ene” monomer 1,3,5-Triallyl-1,3,5-triazine-2,4,6(1H,3H,5H)-trione (TTT) and the photoinitiator 2,2-Dimethoxy-2-phenylacetophenone (DMPA) was acquired from Aldrich.

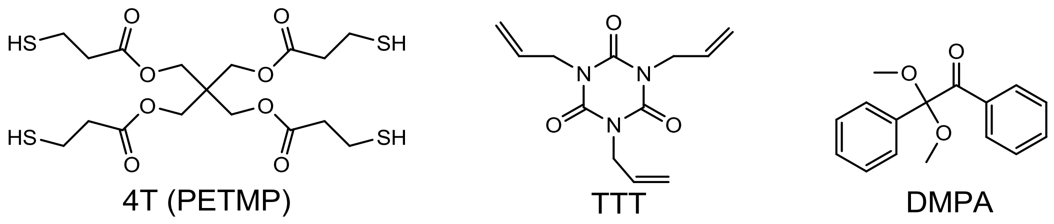

*Figure 23*. Network forming monomers (4T and 3T) and the photoinitiator (DMPA).

Network modifying silane monomers are shown in Figure 24. Acryloxytriisopropylsilane (ISO), (3-acryloxypropyl)methyldiethoxysilane (MDE), acryloxytrimethylsilane (1-TMS), (3-acryloxypropyl)trimethoxysilane (3-TMS) and

(3-acryloxypropyl)tris(trimethylsiloxy)silane (Tris-A) were all acquired from Gelest.

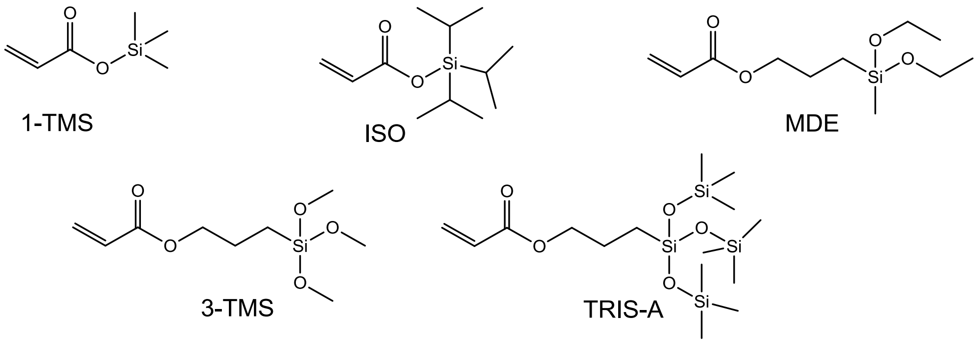

*Figure 24*. Modifying silane acrylates.

*Monomer Modification*

Derivitized monomers were prepared using a nucleophilic catalyzed thio-Michael addition as shown in Figure 25: Step 1. A representative preparation of 1-TMS modified 4T will be described in this text. Tetra functional thiol, 4T (0.01 moles (4.88 g)), was dissolved in 20 ml of acetone and stirred in a round bottom flask for five minutes. One drop (~0.01mL) of dibutylamine (DBA) was added and allowed to stir for five minutes. An equal molar amount of 1-TMS monomer (0.01 moles, 1.44 g) was dissolved in 5 ml of acetone, vortexed, and added dropwise to the 4T-DBA solution using a syringe pump at 0.1 mL/min. The reaction was allowed to mix for 18 hours to ensure complete conversion. The product was placed in a rotary vacuum evaporator for 30 minutes at 70 °C and then placed under high vacuum to remove any remaining acetone and yield the modified product.

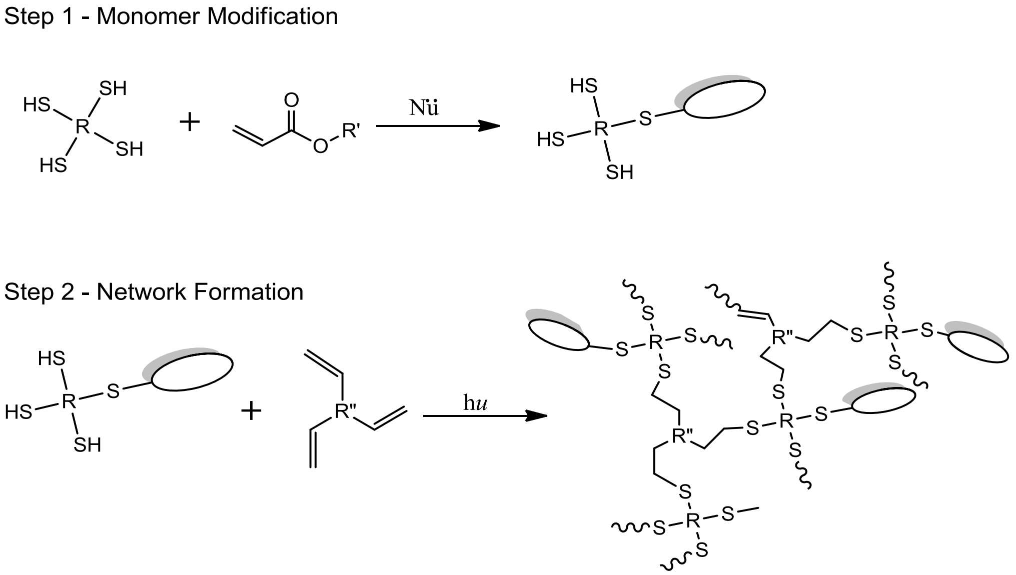

*Figure 25.* Two-step thiol-ene network modification.

### *Network and Film Formation*

Thin films were prepared by adding the perfluorinated acrylate modified 4T monomer to TTT in a 1:1 molar ratio. 1 wt% DMPA was added to the homogeneous mixture, stirred and sonicated for 15 minutes at ambient conditions. The modified monomer mixtures were cast onto a glass plate and sandwiched between a subsequent plate using 0.5 mm spacers for a consistent thickness. Glass-monomer-glass sandwiches were passed ten times through a Fusion UV curing line with a D bulb (400 W/cm$^2$ with belt speed of 3 m/min and 3.1 W/cm$^2$ irradiance). The photoinitated polymerization is shown in Figure 25: Step 2. Films were removed from the glass and equilibrated at room temperature for 2-4 days prior to testing.

### *Characterization*

The derivitization of 4T was confirmed by $^1$H NMR using a Varian Mercury 300 MHz NMR spectrometer in chloroform-d. Conversion of the networks was confirmed using RT-FTIR using Thermo Scientific Nicolet 8700 FTIR irradiated by an OmniCure series 1000 UV lamp with 450 mW/cm$^2$ intensity at 254 nm. Peak areas of the S-H stretch (2570 cm$^{-1}$) and vinyl C-H stretch (3080cm$^{-1}$) were analyzed for conversion.

Oxygen permeability was determined using a constant volume variable pressure (CVVP) instrument, built in-house, as described in our group's previous work[12] and based upon a reported design.[13-16] Thin film thickness was determined by taking the average of nine thickness measurements over the gas exposed film area. Upstream pressures were held constant at 2.3 ± 0.2 atm and temperature was held constant at 23 °C using an immersion circulator. Downstream pressure was recorded as a function of time with a time resolution as low as 0.5 seconds. Steady state permeation, as indicated by a linear pressure increase v. time, was fit using Origin 8.0 software (Northampton, MA) where $R^2$ values were commonly greater than 0.999. Permeability was calculated using

$$\text{Equation 17: } P = \frac{V_d l}{p_2 ART}\left[\left(\frac{dp_1}{dt}\right)_{ss} - \left(\frac{dp_1}{dt}\right)_{leak}\right]$$

where $P$ is permeability, $V_d$ is the downstream volume, $l$ is the film thickness, $A$ is the film area exposed to the permeate gas, $R$ is the gas constant, $T$ is the temperature, and $dp_1/dt$ is the steady state pressure increase in the downstream volume.[12,17]

Differential Scanning Calorimetry was performed on a TA Instruments Q2000 using TA standard aluminum pans with a heating rate of 10 °C/minute from -50°C to 150 °C and a 5 °C/min cooling rate between scans. Film samples were prepared between 7 and 10 mg. Each sample was run twice and the second scans were reported.

Positron annihilation lifetime spectroscopy (PALS) was performed under vacuum (200 millitorr) at 30°C using a fast-fast coincidence system as described in the literature.[11] Thin films were stacked to >1 mm thickness and a stack was placed on either side of a foil wrapped positron-emitting $Na^{22}$ source. Positronium, the product of a positron coupled with an electron, when formed within a polymer material can be used to give an indication of polymer free hole, or defect volume. The lifetime of this long lived positronium is determined by the time between gamma quanta emissions from the birth and death events. Spectra of more than $1.6x10^6$ counts were acquired with a full-width at half maximum of the Gaussian resolution function of 354 ps for the instrument. Lifetime spectra were analyzed and decoupled using PATFIT-88 software[12] to determine the intensity ($I_3$) and $τ_3$. $τ_3$ is used to determine the mean hole free volume of the polymer sample using

$$\text{Equation 18: } \tau_3 = \frac{1}{2}\left[1 - \frac{R}{R_o} + \frac{1}{2\pi}\sin\left(\frac{2\pi R}{R_o}\right)\right]^{-1}$$

where $τ_3$ is the lifetime of the long lived o-Ps, R is the average hole radius and $R_o$ is the sum of R and the empirical constant 0.1656Å. The radius of free holes is then used to calculate the average hole free volume, $\langle V_h \rangle = {}^4/_3 \pi R^3$.

Water contact angle was measured using a Rame-Hart model 200-00 standard goniometer. Deionized water droplets of approximately 5 mm in diameter were applied to thin films via a 0.6 mm diameter syringe; three drops for each film, with ten measurements per drop, were recorded.

Density was measured according to ASTM 1183 based on the Archimedes method. Water was used as the immersion liquid at ambient temperatures. Sample and submerged masses were recorded using a Mettler Toledo XS104 analytical balance equipped with a density determination kit.

## Results and Discussion

### *Verification of the Two Step Method*

As reported in the previous studies, $^1$H NMR was used to confirm the complete consumption of the acrylate during the modification of the tetrafunctional thiol. Shown in Figure 26, the complete disappearance of the peaks, compared to the "acrylate reactant," at 6 ppm indicates the successful consumption of the acrylate.

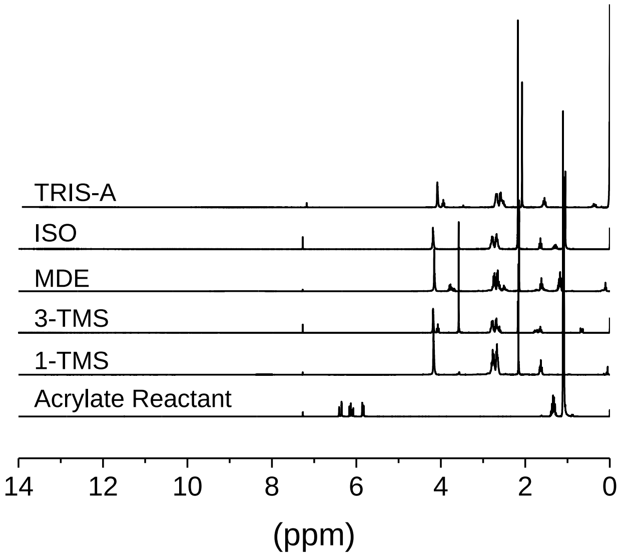

*Figure 26.* NMR spectra of silane modified 4T monomers.

The formation of films was performed, as described in the experimental details, under an industrial scale UV-curing line. To characterize the kinetics of the thiol-ene reaction, Real-Time FTIR spectroscopy was used to quantify the curing of the modified systems. Representative RT-FTIR plots are seen in Figure 27 showing the observed initial and final thiol and  peaks at 2575 cm$^{-1}$ and 3090 cm$^{-1}$ respectively. The near simultaneous conversion of the thiols and the ene double bonds, shown in the conversion v. time plot, demonstrate the rapid cure kinetics of the photoinitiated thiol-ene reaction.

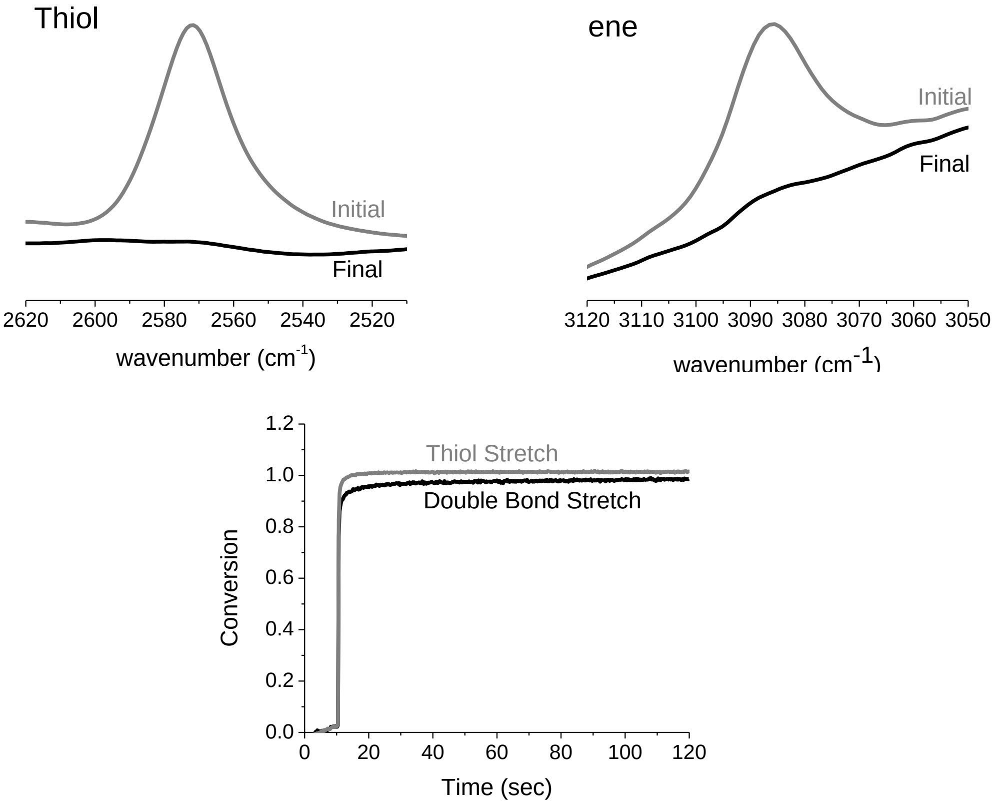

*Figure 27*. Representative RT-FTIR plots of the thiol stretch, ene stretches and conversion versus time.

The final cured films were removed from the glass substrate and observed visually. 1-TMS, ISO, 3-TMS, and Tris-A films were transparent and showed no obvious evidence of phase separation resulting from the modification. MDE did show immediate differences upon removal from the glass. A consistent haze made the material translucent. Ethoxy, and methoxy silanes are known to undergo hydrolytic decomposition in the presence of water, and while there was no evidence of bulk water present during the polymerization of these films, moisture in the ambient environment may have promoted hydrolysis. The presence of hydrolysis products must be further investigated.

### *Network Expansion*

In previous studies of perfluorinated and aliphatic modifications to 4T-TTT systems, the length of the pendent carbon chain provided a reasonable independent variable by which to compare properties because each of the modifications were characterized by the length of the linear side chain. For reference, the structures of the perfluorinated and aliphatic acrylates are shown in Figure 28. In this study, the use of non-linear silane acrylates complicates the independent variable, chain length. Therefore, occupied volumes ($V_{occ}$) were calculated using a Connolly surface applied to each relaxed acrylate using Accelyris Materials Studio 6.1. These occupied volumes will be used as the independent variable used to compare each of the aliphatic, perfluorinated, and silane acrylate modifications. The $V_{occ}$ of each modifying acrylate is listed in Table 1. From this analysis, Tris-A shows the greatest $V_{occ}$. The differences between large, globular moieties, such as Tris-A, and linear moieties are shown in further detail later.

The density of each silane modified network was analyzed to determine the effect of the dangling chain ends on the packing behavior of molecular chains. As seen in Figure 29, linear aliphatic chain ends, from previous work, caused a decrease in the density as the occupied volume of the tethered acrylate increases. A decrease in density is common when increasing the number of dangling chain ends in polymers as the chain ends increase the free volume and mobility. Inversely, fluorinated modifications increase the density as the modification volume increases due to the high density of fluorine. Silane modifications show a decrease in density as larger modifications are tethered into the network. Tris-A, having the largest Vocc, modified networks show the lowest density of the Si modified networks at 1.21 g/cc.

Table 1

*Calculated occupied volumes of the modifying acrylates*

| Perfluorinated Acrylates | | |
|---|---|---|
| Modification | Vocc Å$^3$ | Mw g/mol |
| f2 | 130.16 | 154 |
| f4 | 178.84 | 54 |
| f6 | 237.9 | 318 |
| f8 | 297.08 | 418 |
| f10 | 356.09 | 518 |

| Silyl Acrylates | | |
|---|---|---|
| Modification | Vocc Å$^3$ | Mw g/mol |
| 1-TMS | 163.75 | 144 |
| 3-TMS | 249.28 | 234 |
| ISO | 262.67 | 228 |
| MDE | 276.54 | 246 |
| TrisA | 453.55 | 408 |

| Aliphatic Acrylates | | |
|---|---|---|
| Modification | Vocc Å$^3$ | Mw g/mol |
| a1 | 93.84 | 86.09 |
| a2 | 112.17 | 100.12 |
| a4 | 149.41 | 128.17 |
| a6 | 186.37 | 156.22 |
| a8 | 223.03 | 184.28 |
| a10 | 263.37 | 212.33 |
| a12 | 305.43 | 240.38 |
| a14 | 346.18 | 268.43 |
| a16 | 386.72 | 296.49 |

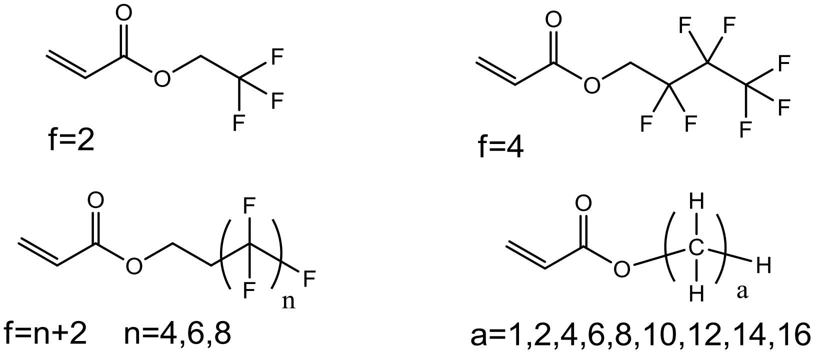

*Figure 28*. Previously studied side chain acrylates with pendent aliphatic (a =) and perfluorinated (f =) chains.

Contact angle, $\theta_c$, was measured to determine the effect of the network modification on surface wettability. As expected, $\theta_c$ of perfluorinated chain modified networks reached the highest values of 108°. Tris-A modified networks has the highest $\theta_c$, 88°. Contact angle as a function of $V_{occ}$ is shown in Figure 30.

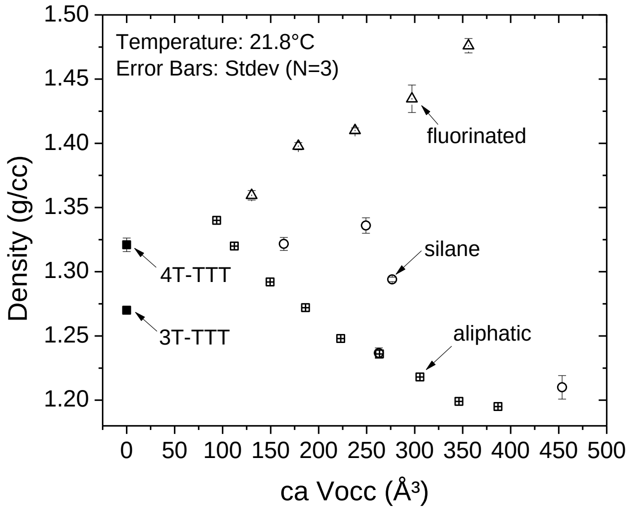

*Figure 29*. Density of fluorinated (Δ), silane (O), aliphatic (⊞) and control (■) networks.

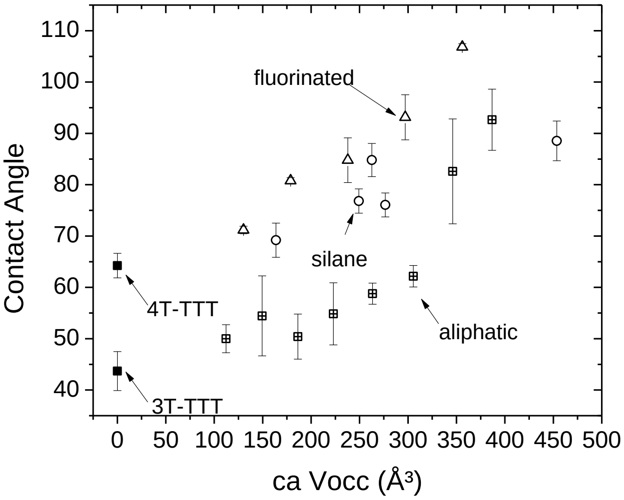

*Figure 30*. Contact Angle of fluorinated (Δ), silane (O), aliphatic (⊞) and control (■) networks.

The glass transition temperature of a polymer system is commonly impacted by the incorporation of small molecule modifiers. Figure 31 shows the glass transition temperature, acquired using DSC, for the three families of modifications. In general, the glass transition shows no major reduction as a result of silane modifications compared to the perfluorinated and aliphatic modifications. Consistent Tg is indicative of a retention of the backbone network. Although the chemical nature of the polymer network changes, the backbone is consistent and the connectivity is theoretically identical. Cooperative long range motions are, in this case, dictated by the network connectivity, not the modification.

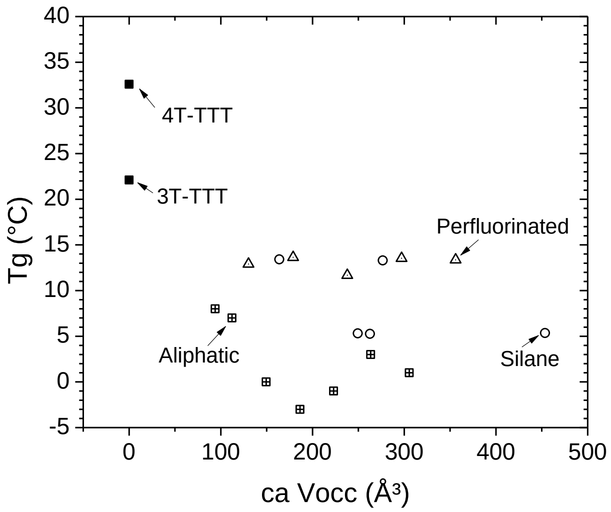

*Figure 31.* Glass transition temperature of fluorinated (Δ), silane (O), aliphatic (⊞) and control (■) networks.

Average free volume hole size was determined by positron annihilation lifetime spectroscopy. Plotted against $V_{occ}$ in Figure 32, the average hole size of modified thiol-ene networks shows a general trend of increasing hole size as the size of the modifier increases. Fluorinated modifications show the largest average free volume; attributed to the high electronegativity and incompatibility of fluorine with other organic moieties causing repulsions within the free volume cavity. Tris-A shows a large average hole size compared to other silane and aliphatic modifications.

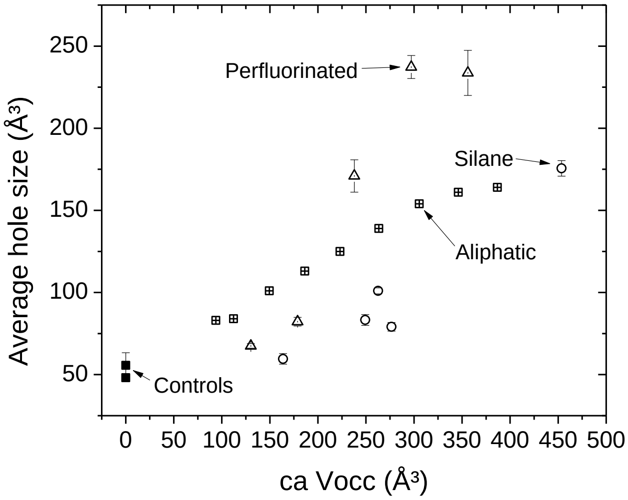

*Figure 32*. Average hole size of fluorinated (Δ), silane (O), aliphatic (⊞) and control (■) networks.

Oxygen permeability was determined for silane modified network and compared to perfluorinated and aliphatic modifications in Figure 33. For fluorinated and aliphatic modifications, there seems to be a dependence on the size of the modification. Perfluorinated modifications show the greatest oxygen permeability at 8.38 Barrer. Tris-A modification has a high $O_2$ permeability at 7.69 Barrer.

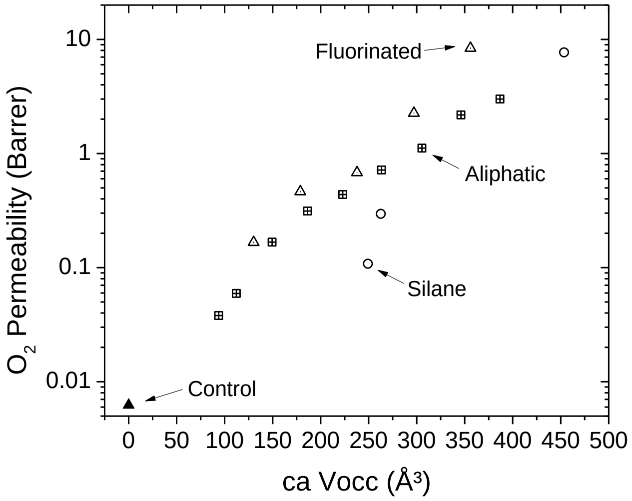

*Figure 33.* Oxygen permeability of fluorinated (Δ), silane (O), aliphatic (⊞) and control (■) networks.

## Conclusion

A large range of properties has been shown for the modification of thiol-ene materials depending on the modification utilized. Silane modifications show great improvements to $O_2$ permeability without the environmental risks of perfluorinated chain modifications. Silane modifications allow for the increase in hole size without the mass increase seen in perfluorinated chain modifications. Further study into larger silane modifications must be performed to push the limits of this modification technique.

## References

(1) Hoyle, C. E.; Lowe, A. B.; Bowman, C. N. Chemical Society Reviews 2010, 39, 1355.

(2) Baker, R. W. Industrial & Engineering Chemistry Research 2002, 41, 1393.

(3) Metz, S. J.; van de Ven, W. J. C.; Potreck, J.; Mulder, M. H. V.; Wessling, M. Journal of Membrane Science 2005, 251, 29.

(4) Gebben, B. Journal of Membrane Science 1996, 113, 323.

(5) Hoyle, C. E.; Lee, T. Y.; Roper, T. Journal of Polymer Science Part A: Polymer Chemistry 2004, 42, 5301.

(6) Hoyle, C. E.; Bowman, C. N. Angewandte Chemie 2010, 122, 1584.

(7) Shin, J.; Nazarenko, S.; Hoyle, C. E. Macromolecules 2009, 42, 6549.

(8) Kwisnek, L.; Nazarenko, S.; Hoyle, C. E. Macromolecules 2009, 42, 7031.

(9) Kwisnek, L.; Kaushik, M.; Hoyle, C. E.; Nazarenko, S. Macromolecules 2010, 43, 3859.

(10) Goetz, J.; Kwisnek, L.; Nazarenko, S. RadTech Report 2012, 27, 27.

(11) Goetz, J.; Greenhoe, B.; Kwisnek, L.; Nazarenko, S. In Thirty-Ninth Annual International Waterborne, High-Solids, and Powder Coatings Symposium New Orleans, LA, 2012.

(12) Kwisnek, L.; Heinz, S.; Wiggins, J. S.; Nazarenko, S. Journal of Membrane Science 2011, 369, 429.

(13) Lin, H.; Freeman, B. D. Journal of Membrane Science 2004, 239, 105.

(14) Lin, H.; Wagner, E. V.; Swinnea, J. S.; Freeman, B. D.; Pas, S. J.; Hill, A. J.; Kalakkunnath, S.; Kalika, D. S. Journal of Membrane Science 2006, 276, 145.

(15) Raharjo, R. D.; Lin, H.; Sanders, D. F.; Freeman, B. D.; Kalakkunnath, S.; Kalika, D. S. Journal of Membrane Science 2006, 283, 253.

(16) In Springer Handbook of Materials Measurement Methods; Horst Czichos, T. S., Leslie Smith, Ed.; Springer Science+Business Media Inc: 2006; Vol. 1, p 371.

(17) Pye, D. G.; Hoehn, H. H.; Panar, M. Journal of Applied Polymer Science 1976, 20, 1921.

# CHAPTER IV

# THIOL-ENE NETWORKS CONTAINING TETHERED PERFLUOROALKYL MOIETIES: SYNTHESIS AND CHARACTERIZATION OF BULK, FREE VOLUME, AND SURFACE PROPERTIES

## Abstract

Tetrafunctional thiol monomers were modified with a series of monofuctional perfluoroalkyl acrylates of increasing length followed by the photopolymerization with a trifunctional ene using a two-step modification technique. Rapid and near complete acrylate, thiol, and ene conversions were observed. The perfluoroalkyl chain length dependence of the glass transition temperature and rubbery plateau modulus suggest that there was not a significant change in the network topology. Free volume analysis using positron annihilation lifetime spectroscopy and high pressure dilatometry analyses indicate an increase in free volume with perfluoroalkyl chain length with an increase in density. Internal pressure data suggests a moderate increase in molecular repulsion of perfluoroalkyl chains caused by incompatible fluorine being covalently bound within the network. Wide angle X-ray data confirms the expansion of the network caused by the perfluoroalkyl chains. The seamless incorporation of fluorine into such thiol-ene networks shows that the kinetics of UV-curing are fast enough to spatially lock into place incompatible chemical structures that are miscible in the monomer mixture but are thermodynamically driven to phase separate after curing causing a molecular scale expansion of free volume holes a redistribution of hole free volume.

## Introduction

Fluorinated polymers possess unique and valuable properties such as hydrophobicity, chemical stability, weather resistance, and high thermal stability. These characteristics arise from the high electronegativity of fluorine and the high carbon-fluorine bond strength. Fluorinated moieties also increase gas solubility and free volume, qualities that are advantageous for gas permeable membranes.[1,2] Indeed, fluorinated polymers exhibit excellent gas permeability and selectivity over their non-fluorinated analogs, challenging Robeson's upper bound in terms of performance.[3] Furthermore, fluorinated polymers such as perfluoro-2,2-dimethyl-l,3-dioxole and tetrafluoroethylene show the highest fractional free volumes, 32 and 37%, among polymers.[4] Unfortunately, fluorinated linear polymers are difficult to process due to high melting temperatures and a strong driving force toward crystallization and phase separation.[5]

In addition to fluorinating linear polymers, attempts have also been made to incorporate perfluorination into photopolymerized (UV cured) networks. These materials are traditionally modified by either mixing fluorinated monomers into monomer blends prior to cure,[5,6] or synthesized and incorporated as short chain fluorinated oligomers[7,8] prior to photopolymerization. Unfortunately, introducing fluorinated monomers leads to phase separation or surface aggregation. This thermodynamically driven aggregation can cause undesirable opacity in films. Furthermore, aggregation severely limits the amount of fluorine that can be incorporated in these materials.[9] New methods that overcome phase separation and allow for the rapid production of high fluorine content polymeric coatings and membranes is therefore sought after.

UV curing, as a processing method for polymer films and coatings, provides numerous advantages over more traditional techniques including thermal processing and emulsions. These advantages include rapid cure rates, spatial and temporal control through the local application of UV irradiation via masks and lasers, solvent free processing, and low manufacturing and infrastructure costs.[10] Much recent attention has been paid to thiol-ene photopolymerization in particular. Compared to acrylates, thiol-enes offer high network uniformity, low oxygen inhibition, and low shrinkage stress owing to the step-growth polymerization mechanism.[11-14] By UV curing combinations of multifunctional thiol and ene monomers, networks with highly tuned characteristics including cross link density, glass transition temperature ($T_g$), modulus, and dangling functionality can be fabricated.

The methodology of incorporating different dangling moieties into the networks via a two-step modification technique was highlighted by our group,[15,16] where a tetrafunctional thiol is modified through the thiol-Michael addition of a monofunctional acrylate in a 1:1 ratio. By consuming the acrylate functionality in the modification step, homopolymerization of the acrylate, which can lead to heterogeneity, is eliminated. These, now trifunctional modified monomers, are then incorporated into the thiol-ene network through photopolymerization with a trifunctional ene monomer. Oxygen permeation was able to be tuned by introducing specific structures into the network. Introduction of hydrogen bonding moieties such as hydroxy terminated acrylates or acrylamides showed increased oxygen barrier compared to unmodified networks.[16] Introduction of alkyl chains showed an increase in oxygen permeability and a decrease in the network bulk density as a function of increased alkyl chain length due to increased hole free volume.[15] The rapid kinetics and near complete functional group conversion~~s~~ of thiol-ene photopolymerizations also provide the potential to “lock-in” morphologies unachievable by the thermal processing of similar polymers.

This two-step modification approach and its advantages are used in the current work to incorporate a large quantity of perfluoroalkyl chains into thiol-ene networks. Despite the typical problems of thermodynamically driven aggregation, surface migration, and fluorine loading limitations, the resulting perfluoroalkyl-modified thiol-ene films are transparent, malleable, and exhibit dramatically different surface and bulk properties compared to the unmodified network. Here we characterize the cavity size and quantity of free volume elements in perfluoroalkyl acrylate modified thiol-ene networks to show that there is stretching of the backbone network leading to changes in free volume distribution caused by the repulsion of fluorine from the alkyl network structure.

## Experimental

### *Materials*

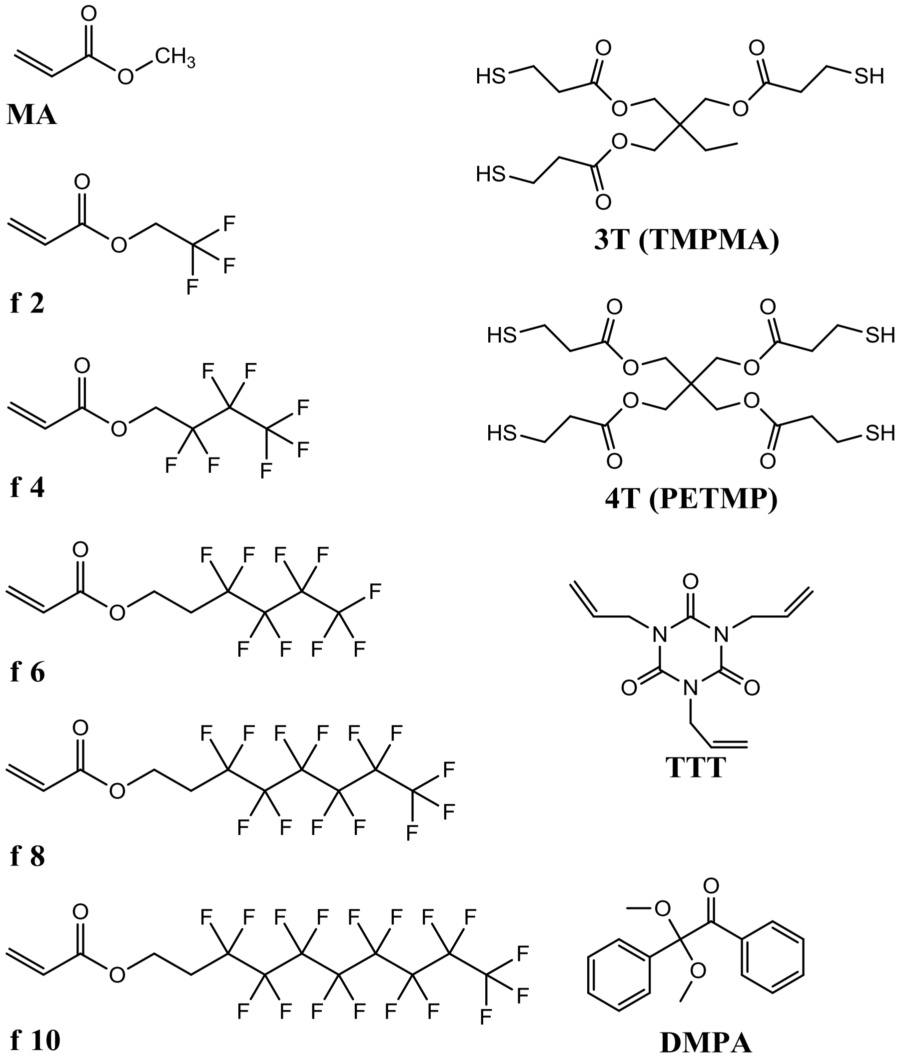

*Figure 34*. Chemical structures of modifying acrylates MA, f2, f4, f6, f8, and f10, network monomers 3T, 4T, TTT and the photoinitator, DMPA used in this work.

Multifunctional thiol monomers pentaerythritol tetrakis(3-mercaptopropionate) (4T) and trimethylolpropane tris(3-mercaptopropionate) (3T) were supplied by Bruno Bock ThioChemicalS (Marschacht, Germany). Multifunctional ene monomer 1,3,5-Triallyl-1,3,5-triazine-2,4,6(1H,3H,5H)-trione (TTT), modifying monomer methyl acrylate (MA), photoinitiator 2,2-Dimethoxy-2-phenylacetophenone (DMPA), and nucleophilic catalyst, di-n-butyl amine (DBA), were acquired from Sigma-Aldrich. Perfluoroalkyl acrylates 2,2,2 trifluoro ethyl acrylate (f2) and1H,1H heptafluoro butyl acrylate (f4) were acquired from SynQuest Labs (Alachua, FL) and 2-perfluorobutyl ethyl acrylate (f6), 2-perfluorohexyl ethyl acrylate (f8), and 2-perfluorooctyl ethyl acrylate (f10) were acquired from Fluoryx, Inc. (San Leandro, CA). These chemical structures are outlined in Figure 34. For convention, perfluoroalkyl acrylates are described by “fX” where X is the number of carbons pendent to the acrylate ester. Modified films are referenced as 4TfX-TTT where 4T is the tetrafunctional thiol, TTT is the trifunctional ene and X, as described, is the number of carbons pendent to the acrylate ester.

*Monomer Modification and Film Preparation*

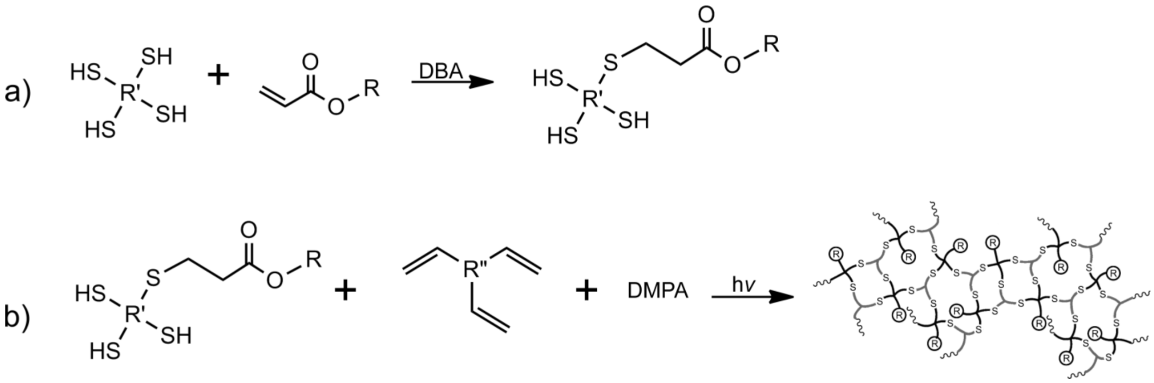

*Figure 35*. Two-step process of modifying a thiol-ene network with perfluoroalkyl acrylates. a) Modification of tetrafunctional thiol (4T) with a monofunctional acrylate possessing a perfluoroalkyl chain end yields an average structure of a single modified, trifunctional thiol monomer with a perfluoroalkyl chain end. b) Photopolymerization of the modified, now trifunctional, thiol and trifunctional ene (TTT) yields a network with covalently bound perfluoroalkyl groups.

*Monomer Modification*

Modified thiol monomers were prepared using the two-step method demonstrated previously,[15-18] as shown in Figure 35. The modified monomer was synthesized using a thiol-Michael addition catalyzed by the nucleophilic dibutyl amine. For all samples, 0.1 moles of tetrafunctional thiol (4T) were vigorously stirred in 20 ml of acetone for five minutes to completely disperse the 4T in solution. Two drops of dibutyl amine catalyst were then added to the solution. Using an addition funnel, an equimolar amount of the desired modifying monoacrylate in 10ml of acetone was added at a constant drop rate over a 10 minute period. The reaction vessel was sealed and left to react overnight. Acetone was rotovaped from the modified monomer at 40°C under vacuum. The residual acetone was removed from the modified monomer under high vacuum at room temperature for two hours. The modified thiol monomer was used as prepared, without purification. As discussed in prior work,[15] the product of the one-to-one addition of the monoacrylate to the tetrafunctional 4T, in fact, yields a distribution of modified monomers. This mixture of modified thiol products is assumed to have a statistical average of single addition, tri functional, 4T thiol monomers with a small population of other components. In future work we plan to isolate the ideal product, a trithiol with one acrylate modifier and study the differences between networks with this ideal monomer and networks with the statistical mixture.

*Film Preparation*

Control sample films, 4T-TTT and 3T-TTT, were prepared by mixing thiol and TTT monomers in a 1:1 functional group ratio. All modified 4T monomers were mixed with an equal-molar amount of TTT to match thiol and ene content in the bulk mixture. 1 wt% DMPA photoinitiator was added to each bulk mixture. Monomer mixtures were briefly vortexed and then sonicated for 15 minutes at ambient conditions to completely dissolve and disperse the photoinitiator. With the exception of 4Tf10-TTT, all of the modified monomers readily mixed into the TTT monomer and the mixtures were transparent at room temperature. 4Tf10-TTT mixtures required heating to 40 °C to ensure the mixtures were transparent prior to curing. Smooth, scratch free glass plates were cleaned with acetone and used as the film substrates. For the unmodified, two component control samples, glass plates were cleaned with acetone and treated with Rain-X(Galena Park, TX) to aid in the removal of the final film from the glass substrate. Homogeneous monomer mixtures were poured onto glass plates and sandwiched with a second glass plate using shims to ensure consistent thickness of ~500 µm. Each glass sandwich was passed ten times under a Fusion UV Systems EPIQ 6000 high intensity UV line where the average UV exposure time was 29 seconds with an irradiance of 3.1 W/cm$^2$at a belt speed of 0.23 m/s. Films were then removed from the glass substrates and left at ambient conditions for at least 24 hours before testing.

### *Characterization*

Conversion of the acrylate functionality from the modifying perfluoroalkyl acrylate attached to the thiol was confirmed via $^1$H NMR spectroscopy with a Varian Mercury 300 MHz NMR spectrometer in acetone-$d_6$. A Bruker Tensor 37 FTIR was used to confirm monitor the real time conversions of thiol and ene groups at 2570 and 3085 cm$^{-1}$, respectively. Peak area was calculated as a function of time. Mixtures of the modified thiol, trifunctional ene and photoinitiator were sandwiched between salt plates and the salt plates were arranged coincident to the IR laser. Acquisition was started and FTIR spectra were collected in 0.25 second intervals. After ten seconds of acquisition, the sample was irradiated with UV light by an OmniCure series 1000 UV lamp equipped with a fiber optic guide directed at the salt plates. The light intensity was 450 mW/cm$^2$ at a wavelength of 254 nm. Each sample was studied under irradiation for 60 seconds. Real-time disappearances of the area under thiol and ene peaks were calculated as each peak approached the baseline. Conversion was calculated as the relative peak area loss at a given time.

The glass transition temperature, $T_g$, of each film was determined from differential scanning calorimetry thermograms using a TA DSC Q2000. A heat-cool-heat program was employed where 8-10 mg samples were heated from room temperature to 100 °C at 10 °C/min, cooled to -70 °C at 5 °C/min and heated again to 100 °C at 10 °C/min in a nitrogen purged atmosphere. $T_g$ was resolved from the second heating thermograms at the inflection point of the step change. The breadth of the glass transition was determined as the difference between the onset and endset of the glass transition according to reported methods.[19]

The $T_g$, rubbery plateau modulus, and glassy modulus of each film was determined by performing dynamic mechanical thermal analysis using a Rheometric Scientific DMTAV at a frequency of 1 Hz, with a strain rate of 0.05%, and a heating rate of 5 °C/min from -50 to 200 °C. The $T_g$ was determined by the peak of the tan δ versus temperature plot.

Wide angle X-ray Diffraction was performed using a Rigaku Ultima III diffractometer (Cu Kα radiation, $\lambda = 1.542$ Å). The diffractometer, set up with a Bragg-Brentano parafocusing geometry, was programmed with a step size of

0.20 2θ at a scan rate of 0.25 steps/min, and a diffractogram range of 2 to 40 degrees 2θ.

Water contact angle was measured using a Rame-Hart model 200-00 standard goniometer. Sample films were cleansed with ethanol and allowed to dry for 15 minutes prior to testing in order to remove any dust or oils. Deionized water droplets with a diameter of approximately 5 mm were applied to the thin films using a 0.6 mm diameter syringe. An average of ten measurements from three drops on each sample was recorded using Rame-hart DROPimage Standard software. The average of these thirty measurements is reported for each film. The refractive index of the sample films was determined using a Reichert ARIAS 500 refractometer (Depew, NY, USA), with an LED light source at a wavelength of 589 nm and a glass prism heated to 25 °C.

Density was determined according to Archimedes' displacement method using a Mettler Toledo XS104 analytical balance equipped with a density determination kit. Using deionized water as the immersion fluid, masses were collected at ambient conditions (21.5 °C) in triplicate with an accuracy of 0.001 g yielding an experimental error of less than 1%.

Specific volume versus temperature measurements were determined using a Gnomix high pressure mercury dilatometer (Gnomix, Boulder, CO) as detailed by Zoller.[20] Sections of thin films were precisely stacked for a total volume greater than one cubic centimeter and these stacks were loaded into a rigid cell and evacuated for five minutes under vacuum. The remaining cell volume was filled with mercury; encapsulating the sample. Internal flexible bellows were connected to alinear variable differential transducer, LVDT, and the cell was secured within the pressure vessel. These bellows allow for volumetric expansion of the sample and mercury under an applied heat and pressure. The expansion of the mercury and sample inside the calibrated volume was detected as a linear displacement by the LVDT. Temperature and pressure were controlled using a standard isothermal (ITS) protocol which was performed from 30 °C to 180 °C in increments of 25°C with a pressure range from 10 MPa to 150 MPa. To obtain data near ambient conditions (0.1 MPa), conventional Tait extrapolations from the high pressure data to 0.1 MPa were performed within the Gnomix v8.06 software.

The average free volume hole size and relative intensity measurements of o-Ps formation were determined from positron annihilation lifetime spectroscopy (PALS) experiments on a fast-fast coincidence system based on an Ortec Positron Lifetime System (Advanced Measurement Technology Oak Ridge, TN) which has been described.[21] The spectrometer had an average resolution FWHM of 385 ps. Thin film sample discs were stacked to achieve a total thickness greater than one millimeter and each sample stack was contained in aluminum foil packets. An aluminum foil wrapped Na-22 radio nucleotide source was sandwiched between the two sample packets. The sample-source sandwich assembly was then placed in a custom, sealed, thermal vacuum chamber. Photomultiplier tube assemblies (Hamamatsu H3378-50) – equipped with $BF_3$scintillation crystals – were then aligned coincident to the sample stack. Positron and positronium annihilation coincidence events were compiled as a function of lifetime using a multichannel analyzer. Each spectrum required the collection of coincidences over one hour to acquire greater than $10^6$ lifetime events. Sample temperature was controlled within ± 0.1 °C using a Lakeshore 331 temperature controller. PALS spectra were collected from -32.5°C to 127.5°C in increments of 5°C. The samples were allowed to equilibrate for 15 minutes prior to beginning spectrum collection at each temperature. Three temperature sweeps were performed on each sample. Spectra were analyzed for three discrete lifetimes and intensities using PATFIT-88 software.[22] In polymers, three lifetime components are commonly observed where the free volume holes are probed by the long lived, third component caused by ortho-positronium formation and annihilation. Four component fits were utilized where two different o-Ps probeable hole sizes were expected. Here, we attempted both three and four component fits but found no strong evidence of a fourth component in any of the studied samples.

## Results and Discussion

### *Monomer Modification and Characterization*

Multifunctional thiol monomers were modified using the thiol-Michael addition procedure outlined in the Experimental section. $^1$H-NMR spectroscopy confirmed quantitative conversion of the acrylate double bonds. Figure 36 shows the $^1$H-NMR spectra for the series of modified 4TfX and 4TMA modified monomers. For reference, the spectrum for an unreacted f8 acrylate with peaks at 6 ppm is shown. Full disappearance of the vinylic peaks, around 6 ppm, indicated complete consumption of the acrylic double bonds. Complete conversion showed that the modification was unaffected by the length of the perfluoroalkyl chain.

As mentioned in the Experimental section, previous work in our group[15] acknowledged that modifying 4T with monoacrylates results in a distribution of products. For the purpose of developing structure-property relationships, we assume the average product is a mono-derivitized thiol. With this assumption, cross link density is considered to be uniform and the modifying groups, i.e. perfluoroalkyl chains, are randomly dispersed.

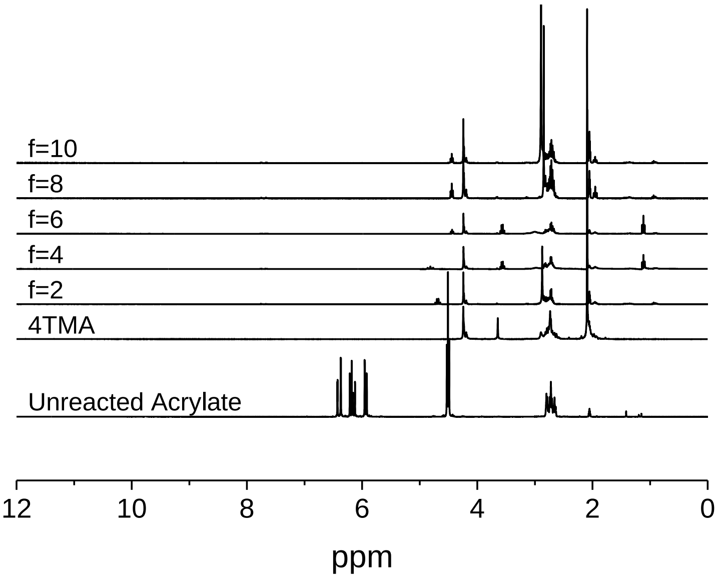

*Figure 36*. NMR spectra of modified 4T monomers displaying the disappearance of vinylic hydrogen peaks at 6 ppm for all modifications. For reference, an unreacted f8 acrylate is included to display the presence of targeted vinylic peaks at 6 ppm.

*Film Preparation*

To confirm that the perfluoroalkyl chains did not hinder the overall conversion of the network or impact the cross linking, conversion of the thiol and ene functional groups was monitored in real time with FTIR spectroscopy. Figure

37 shows representative spectra excerpts for the thiol stretch (2525-2600 $cm^{-1}$) and ene CH and $CH_2$ stretches (3020-3100 $cm^{-1}$), before and after UV irradiation, for the networks with the shortest and longest 4T modifications, 4Tf2-TTT and 4Tf10-TTT, respectively. Peak areas were monitored as a function of cure time and representative conversion as a function of time is shown in Figure 38 for 4Tf2-TTT and 4Tf10-TTT. Near complete peak disappearance was observed for all modified networks. Conversion of both thiol and ene groups was rapid and simultaneous, approaching conversions greater than 90% in less than 10 seconds. Prior to sample irradiation, a small amount of thiol and ene conversion was observed. This small amount of conversion before curing was expected to have played a negligible role in the formation of the final films as thiol-enes are known to have a late gelation point,[13] and the final films were cured within minutes of mixing the thiol and ene monomers. These conversion results are consistent with previous work[15] and indicate that the modifications do not have a measurable effect on conversion of perfluoroalkyl acrylate modified thiol-ene networks.

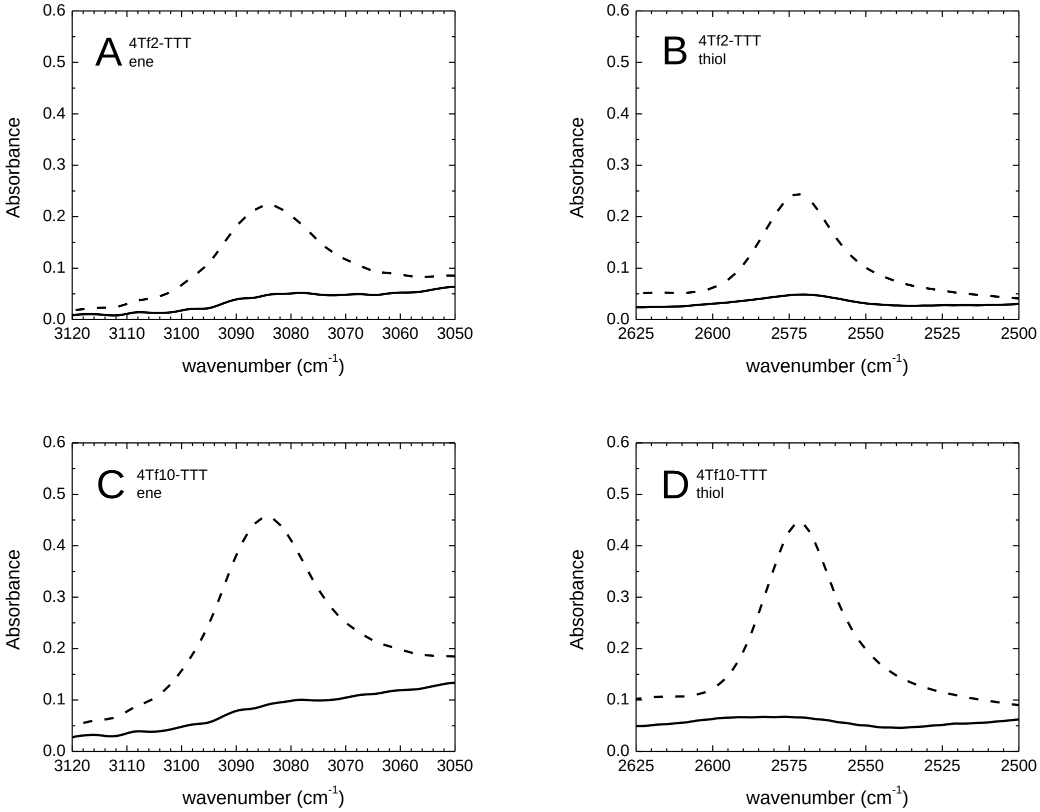

*Figure 37*.–Excerpts of real time FTIR spectra of thiol (B and D) and ene (A and C) stretches for 4Tf2-TTT and 4Tf10-TTT formulations before (dashed line) and after (solid line) UV irradiation.

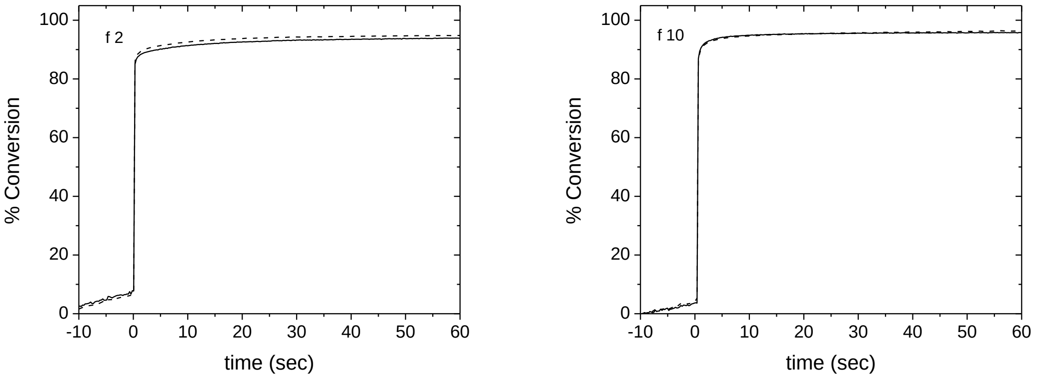

*Figure 38*. Real time conversion versus time plots of the thiol (dashed line) and ene (solid line) for 4Tf2-TTT and 4Tf10-TTT systems irradiated under UV light.

Films were cured according to procedures outlined in the Experimental section. After curing, films were removed from the glass substrates and thicknesses were determined to be ~500 µm. All modified thiol-ene films were optically transparent with fluorine atom loadings as high as 26% (w/w) for 4Tf10-TTT films. Typically perfluoroalkyl chains in polymer networks cause opacity or a haze from macroscopic phase separation of the perfluoroalkyl moieties. Previous work on bisphenol-A diacrylates suggested that the upper loading limit of perfluoroalkyl acrylates to be near 0.8% (w/w) before macroscopic evidence of phase separation occurred.[23] This phase separation occurred because the fluorinated chains were not covalently bound to other components, allowing them to aggregate and phase separate before and during photopolymerization. In contrast to that method, the two-step approach used in this work prevents phase separation because the perfluoroalkyl additive is covalently bound to a multifunctional thiol, restricting its mobility and providing misicibility in the monomer mixture.

There may be a certain degree of aggregation of the perfluoroalkyl chains on the surface of these modified thiol-ene networks. However, we have no direct evidence of this and it would require further study. The near complete functional group conversion, along with the transparency of the final networks suggest that there was sufficient mixing in the unreacted mixture prior to curing to retain a dispersion of thiol and ene functionality throughout the bulk of the mixture. It is postulated that the rapid kinetics of UV-curing allows for the network to form fast enough to lock the tethered perfluoroalkyl groups in the bulk before any phase separation and aggregation into macroscopic sized domains can occur. The effect of locking these perfluoalkyl groups into the network on the network topology, bulk properties, and free volume is investigated in further detail below.

*Thermal Properties*

In addition to the potential impact of perfluoroalkyl additives on the conversion and phase separation during photopolymerization, the thermal properties of the films may also be affected. It was anticipated that cross link density or segment mobility may be disturbed by introducing bulky perfluoroalkyl chains into the networks. Thermal analysis was therefore performed on each network as a principal assessment of these potential effects. DSC and DMTA experiments were performed to study the effect of covalently bound perfluoroalkyl modifications on the network topology by analyzing the glass transition temperature and rubbery plateau modulus for each network. $T_g$ was expected to decrease with the incorporation of modifications relative to the unmodified tetrafunctional control, 4T-TTT, because of the decrease in cross link density caused by the addition of the acrylate modification. DSC thermograms are plotted in Figure 39A and glass transition temperatures are plotted in Figure 39B with error bars representing transition width. Each network, including modified and control networks, show a typical amorphous behavior with a single step change. The perfluoroalkyl modified networks all show similar $T_g$s between 12 °C and 15 °C and similar transition breadths between 14 °C and 24 °C across the modification range.

Two unmodified networks, each made up of two-components, 4T-TTT and 3T-TTT, and one modified network 4TMA-TTT, were used as reference networks. Each network aimed to address different aspects of the possible changes that are inherent with the addition of modifications such as added chemical structures and decreases in cross link density. The 4T-TTT network utilized the same backbone monomers as in the modified networks but inherently had a higher cross link density due to the tetrathiol functionality of the 4T monomer. The 3T-TTT network eliminated the tetrafunctional junction points of 4T-TTT network. 3T-TTT networks, therefore, were assumed to have the same network topology without the contribution of a long free end. Since the primary goal of this work is to study the effect of fluorine on network properties, minimizing the chemical difference between the control and the modified networks was important. The described control networks had the same backbone chemical structure as the modified systems but differed from the modified networks as the dangling chain ends of the modified network contained both a thio-ether and ester linkages.  As a third control, a methylacrylate (MA) modified network, 4TMA-TTT, was used to contrast the effect of a single terminal methylene unit to the modified fluorine networks while including the thioether and ester linkages. 4TMA-TTT, therefore, most accurately mimicked the network modification due to the presence of the thioether and ester linkages of the modification chain end.

The magnitude of the step change at $T_g$, $\Delta C_p$, decreased with increasing perfluoroalkyl chain length. $\Delta C_p$ values are tabulated in Table 1. $\Delta C_p$ is a measure of the energy needed for long range translational motions, typically associated with the glass transition. Decreased $\Delta C_p$ from increased perfluoroalkyl chain lengths indicated that the input energy requirement to cause long range motions in longer perfluoroalkyl chain modified networks was lower. This decrease in $\Delta C_p$ suggested that the perfluoroalkyl chains increased the free energy in the glassy state; the longer the perfluoroalkyl chain, the closer in energy to the disordered, mobile melts state.

DSC results also suggest that $T_g$ was controlled primarily by the connectivity and architecture of the backbone thiol-ene network, not the perfluoroalkyl modifications. This effect was similar to the incorporation of alkyl chains in thiol-ene networks in previous work.[15] To determine if the network connectivity changed as a function of perfluoroalkyl chain modification, storage modulus and tan δ were analyzed using DMTA.

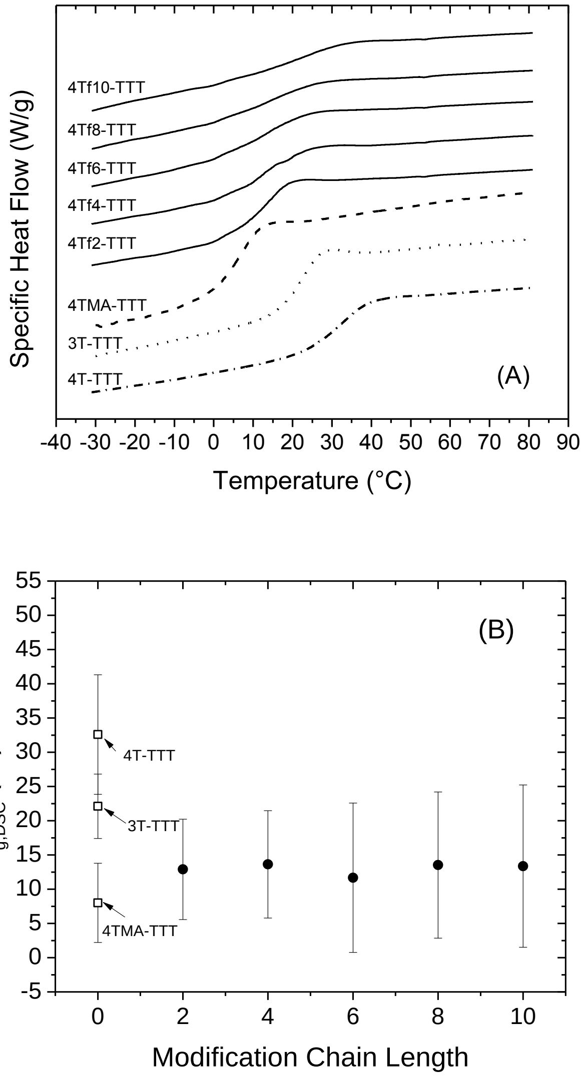

*Figure 39*. (A) DSC thermograms for all networks. Perfluoroalkyl modified networks are shifted to show details and are denoted with solid lines and the 4TMA-TTT, 3T-TTT, and 4T-TTT networks are displayed with dashed, dotted, and dash-dot lines, respectively. (B) Glass transition temperatures for each control and modified network. Error bars signify the breadth of the transition.

Similar to DSC analysis, DMTA also confirmed little effect of perfluoroalkyl length on $T_g$. DMTA storage modulus and tan δ versus temperature for all networks are plotted in Figure 40. Glass transition temperatures are plotted as a function of modification length in Figure 41 with error bars representing the standard deviation of three runs. E’ in the rubbery plateau region at 100°C was found to be similar for all modifications within a range of 3.6 MPa. Similar modulus suggested similar network connectivity in the backbone structure of the network across all modified networks. $T_g$ from the tan δ peak did not show a considerable change across the range of modifications. Consistent with previous work, DMTA shows about a 10 °C higher $T_g$ than DSC.[15]

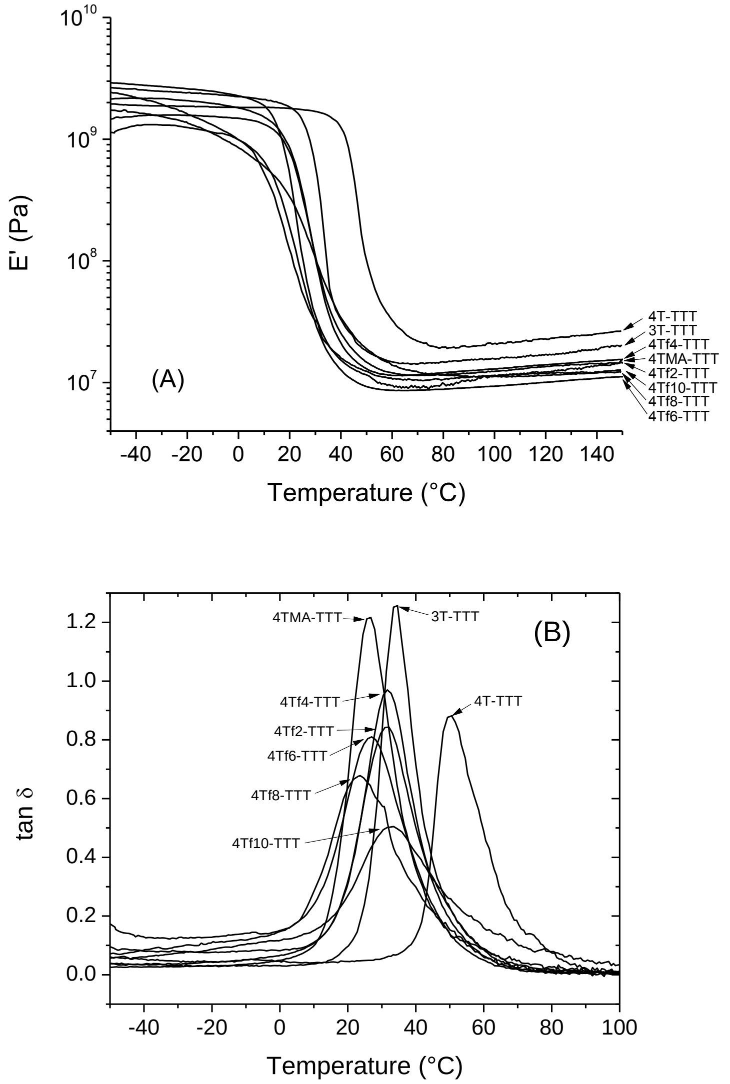

*Figure 40*. Representative E' versus temperature (A) and tan δ data versus temperature (B) data for all networks and controls.

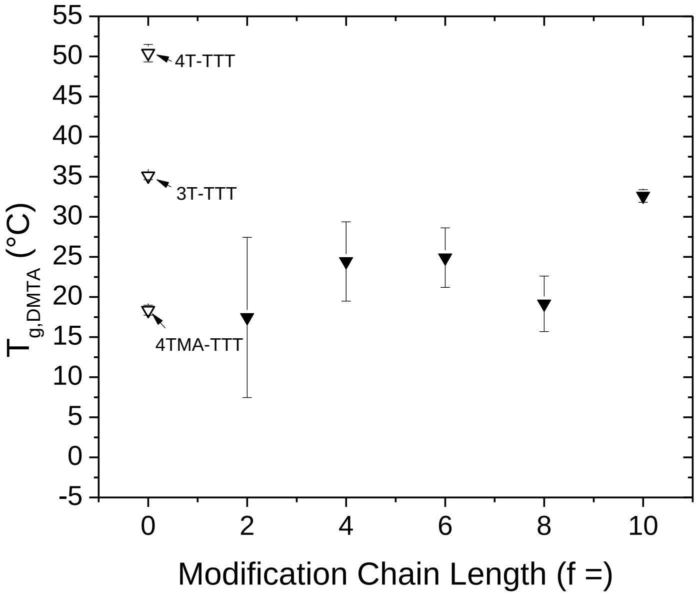

*Figure 41*. Glass transition temperatures measured by DMTA as a function of modification length, X, in 4TfX-TTT networks. DMTA error bars signify a single standard deviation of three tests.

*Bulk Properties*

Fluorine content in polymers and networks is known to impact various physical properties including refractive index, water contact angle and density. Table 2 lists these properties along with the mass and molar fractions of fluorine for all networks. PTFE is included as a reference. In other cross linked networks, refractive index decreased as fluorine content increased.[24,25] Likewise, increased fluorine content in the modified thiol-ene networks caused a gradual decrease in the refractive index. Increased fluorine content also led to a gradual increase in water contact angle as the perfluoroalkyl chain length increased. It would be expected that if perfluoroalkyl groups migrated to the surface, maximum water contact angle would be achieved with short, f2 or f4, perfluoroalkyl chains. Instead, the observed gradual progression in water contact angle suggests that perfluoroalkyl groups did not aggregate on the surface enough to impact water contact angle drastically. Water contact therefore increased as a result of an overall increase in perfluoroalkyl content. The 4Tf10-TTT modified network achieved a contact angle of 107°, approaching that of PTFE, with only 26% w/w% of fluorine. These results show how the two-step thiol-ene approach can achieve some of the desired properties of PTFE with the advantages of thiol-ene photopolymerization.

Table 2

*Fluorine weight and molar fractions, Refractive Index, Density, and Contact Angle Data for all control networks, modified networks, and PTFE for reference*

| Material | Fluorine Weight Fraction | Fluorine Mole Fraction | Refractive Index, n | Density ρ g/cc | Water Contact Angle ° |
|---|---|---|---|---|---|
| 4Tf2-TTT | 0.064 | 0.030 | 1.542 | 1.359 | 71 |
| 4Tf4-TTT | 0.134 | 0.065 | 1.531 | 1.387 | 81 |
| 4Tf6-TTT | 0.162 | 0.080 | 1.518 | 1.395 | 85 |
| 4Tf8-TTT | 0.214 | 0.109 | 1.502 | 1.425 | 93 |
| 4Tf10-TTT | 0.257 | 0.136 | 1.495 | 1.476 | 107 |
| 4T-TTT | - | - | 1.557 | 1.270 | 61 |
| 3T-TTT | - | - | 1.565 | 1.321 | 64 |
| 4TMA-TTT | - | - | 1.551 | 1.310 | 45 |
| PTFE | 0.760 | 0.667 | - | 2.23[26] | 108[27] |

Previously, alkyl chain modification of thiol-ene networks was reported to decrease the bulk density as a result of an increase in hole free volume.[15] It was predicted that perfluoroalkyl chains would have a similar effect on free volume but, as shown in Table 1, the density of each network increased in accord with the length of the perfluoroalkyl chain. Other authors have reported similar behavior and stated that the bulk density was not a good predictor of free volume behavior or intermolecular spacing[2] due to fluorine's high density. Since density data alone cannot elucidate structural and free volume behavior, we proceed to investigate the molecular and free volume behavior of these modified networks using PALS, WAXD, and PVT.

*Free Volume Behavior*

Previous work showed that the addition of long aliphatic chains to a thiol-ene network increased the free volume hole size as the perfluoroalkyl chain length increased. Perfluoroalkyl chains were expected to show a similar effect. Hole free volume, $v_h$, was determined by PALS as described in the Experimental section. Assuming spherical holes, the average ortho-Positronium lifetime, $\tau_3$, was used to calculate the radius, $R$, of the free volume holes according to Tao[28] and Eldrup[29]

$$\text{Equation 19} \quad \tau_3 = 0.5\left[1 - \frac{R}{R+\Delta R} + \frac{1}{2\pi}\sin\left(\frac{2\pi R}{R+\Delta R}\right)\right]$$

where $R$ is the radius of the cavity, and $\Delta R$ is a constant 1.656 Å describing the penetration of o-Ps into the electron bulk. The average volume of the spherical hole was then calculated using the following relationship: $\langle v_h \rangle = \frac{4}{3}\pi R^3$.

PALS data was collected at five degree intervals from -33 °C to 128 °C for each network, and the results are shown in Figure 42. An increase in $<v_h>$ is apparent as the perfluoroalkyl chain length increases. Each of the $<v_h>$ versus temperature plots, for modifications greater than 4Tf2-TTT, showed a decrease in the temperature coefficient above 75 °C. This decrease in temperature coefficient has been discussed in previous work as o-Ps bubbling which occurs when the time scale of segmental motions and the lifetime of o-Ps are comparable,[30] which suggests an upper limit to the longest detectable lifetimes for polymeric samples using positron annihilation. The average hole sizes for 4Tf4-TTT and 4Tf6-TTT show a plateau beginning near 60 °C. With the data in Figure 42, there seems to be an upper limit for the detectable size of free volume cavities in these modified thiol-ene networks.

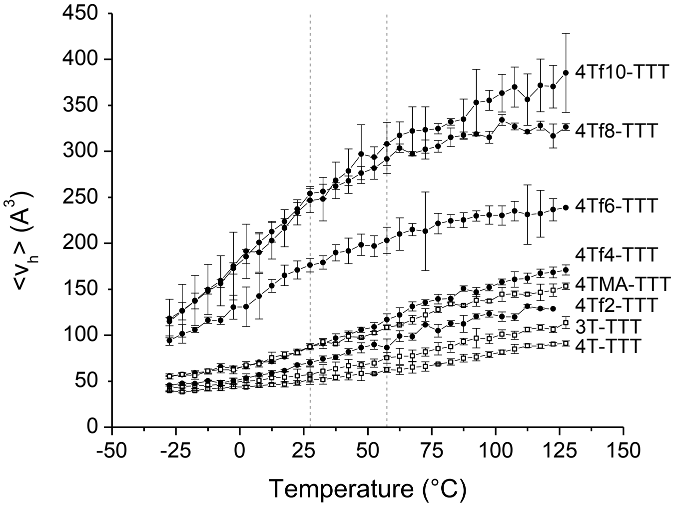

*Figure 42*. <*$v_h$*> versus temperature for all perfluoroalkyl networks and control networks. Vertical lines at 27.5 °C and 57.5 °C indicate the range above $T_g$ and below the bubbling onset, or knee temperature $T_k$.

Due to the possibility of o-Ps bubbling in 4Tf6-TTT, 4Tf8-TTT, and 4Tf10-TTT, it is important to consider the scale of the changes in hole size for the unmodified networks and the fluorinated networks from 4Tf2-TTT to 4Tf10-TTT at temperatures below the onset of bubbling. To understand the effect of modification length on the mean hole free volume, <*$v_h$*> at 22.5 °C is plotted against modification chain length in Figure 43 for all control and modified networks. Here, <*$v_h$*> shows a threefold increase across the series of modifications. The largest <*$v_h$*> increases occur in 4Tf6-TTT through 4Tf10-TTT. In the case of these modified perfluoroalkyl systems, the true hole size of 4Tf10-

TTT may also be underestimated as a result of positronium bubbling as the o-Ps lifetimes became very long, on the order of 4.5 ns. Regardless, the PALS data suggests an increased hole size for 4Tf8-TTT and 4Tf10-TTT networks, as a result of the modification, compared to the shorter modifications and the control networks. The gradual increase in hole size is suggested to be due to the rigid rod nature of perfluoroalkyl chains as well as the hydrophobic and lipophobic nature of fluorine, creating a repulsive effect in the network. We suggest that the long perfluoroalkyl chains were energetically driven toward phase separation but were covalently bound to the backbone network causing a thermodynamic "frustration," repelling the backbone and increasing hole free volume in the network.

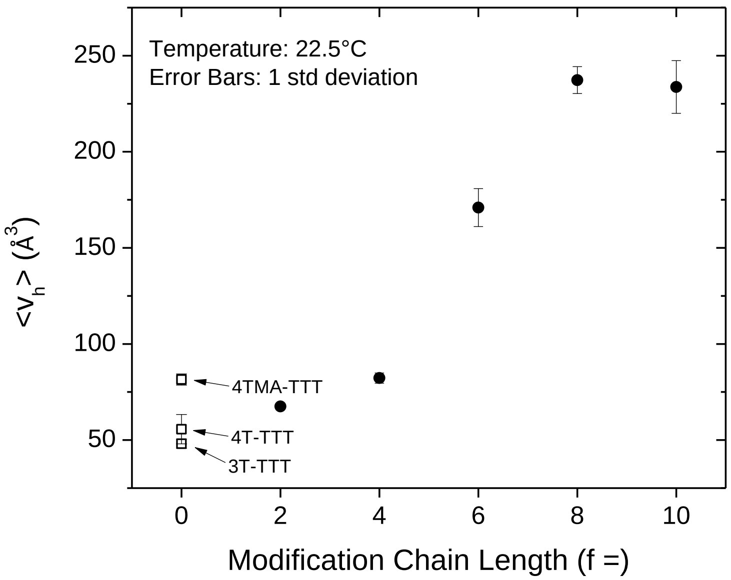

*Figure 43*. Average free volume hole size as a function of modification length at ambient conditions. Error bars represent one standard deviation.

The increase in $<v_h>$ proved interesting considering the large increases in film density observed with the increased fluorine content. Fluorine, as stated, has a high mass to volume ratio and is known for its incompatibility with other organic atoms resulting from high electronegativity and low polarizability. Here we suggest that the incompatibility of fluorine with the network backbone induced a thermodynamic “frustration” where fluorinated tails are driven to, but cannot phase separate, causing the free volume hole around the fluorinated chain end to expand. Unlike structural frustrations or the non-equilibrium glassy state, caused by quenching to temperatures below $T_g$, the observed thermodynamic “frustration” is apparent in these networks in the melt state. This concept is further demonstrated in the wide angle X-ray data shown in Figure 44 where the amorphous halo can be seen to shift toward lower diffraction angles as the length of the fluorinated tail increases. Slutsker et. al. have suggested that during thermal expansion, a shift in the 2θ angle of an amorphous halo, from higher angles to lower angles, results from an increase in the spacing between backbone atoms.[31] Furthermore, O’Brien suggested that permeability of light gases, evidence of changes in free volume, correlates to the average intersegmental separation evidenced by WAXD amorphous halo peaks in polyimides.[32] Hullums also displayed the shifting of the amorphous halo as a result of substituting the $CH_3$ hydrogens with fluorine in bisphenol-A based polycarbonate.[2] The WAXD diffractograms for these networks containing the tethered perfluoroalkyl groups behave in a manner analogous to linear polymers undergoing thermal expansion. The shift of the amorphous halo toward small angles suggests an increase in inter-chain distance or expansion of the backbone occurred as the length of the perfluoroalkyl tail was increased.

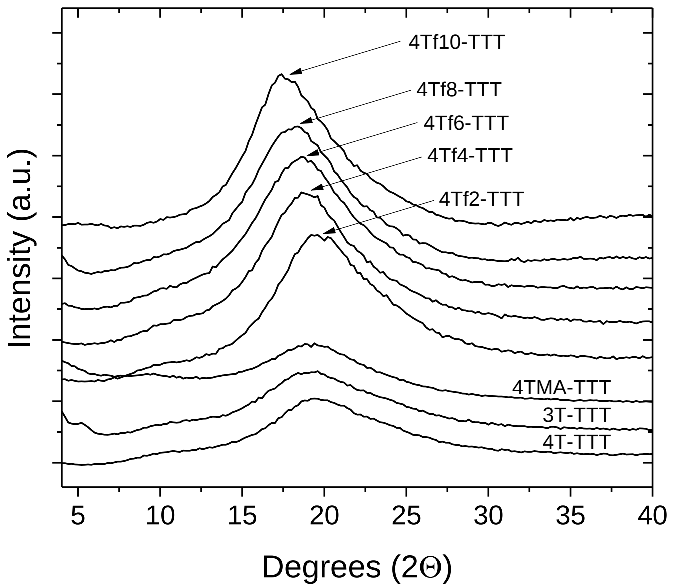

*Figure 44*. Wide angle X-ray diffractograms for control, 4T-TTT, 3T-TTT, and 4TMA-TTT and modified networks 4Tf2-TTT through 4Tf10-TTT.

The increases in free volume can be further supported by investigating the internal pressure of the network determined from a PVT surface which describes the dependence of specific volume, $V_{sp}$, on temperature and pressure. Figure 45 is a representative plot of typical $V_{sp}$ data from an isothermal PVT experiment for 4Tf2-TTT. From the PVT surface, volumetric thermal expansivity, $\alpha$, isothermal compressibility, $\beta$, and internal pressure, $P_i$, were determined at 30 °C using

Equations 20 $$\alpha \equiv \frac{1}{V}\left(\frac{\partial V}{\partial T}\right)_p$$

Equation 21 $$\beta \equiv -\frac{1}{V}\left(\frac{\partial V}{\partial p}\right)_T$$

Equation 22 $$P_i = T\left(\frac{\alpha}{\beta}\right) - p$$

where $p$ is the applied external pressure. From the PVT surface, the partial derivative $\left(\frac{\partial V}{\partial T}\right)_p$ was determined by treating the melt state temperature dependence of $V_{sp}$ as linear for each pressure. To determine $(\partial V/\partial p)_T$, the melt state nonlinear pressure dependence of $V_{sp}$ was fit with a second order polynomial and the partial derivative was determined at each temperature. *α* and *ß* at ~0 MPa and 300 K are plotted in Figure 46 and both increased gradually as the perfluoroalkyl length increased. These increases in *α* and *ß* are reasonable as free volume is more compressible than the occupied volume in the network. Therefore, increasing the amount of free volume or the size of these free volume holes, inherently increases *α* and *ß*.

By definition, internal pressure describes the change in internal energy in the event of a volume change at a given temperature and decreases in internal pressure suggest an internal repulsion of chemical structures. Figure 47 shows the internal pressure decreases as a function of modification length which can be attributed to the fluorinated chains, that, although covalently bonded to, are otherwise incompatible with the network, causing increased repulsion and decreased internal pressure.

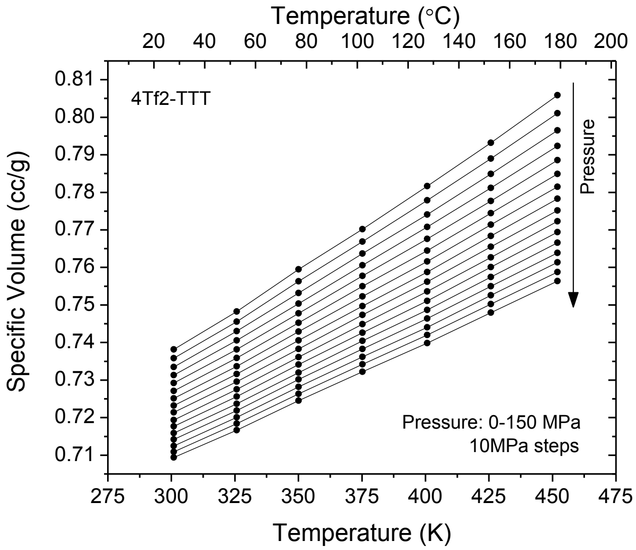

*Figure 45*. Vsp as a function of temperature and pressure data from a standard isothermal PVT experiment for 4Tf2-TTT from 0 to 150 MPa in 10 MPa steps.

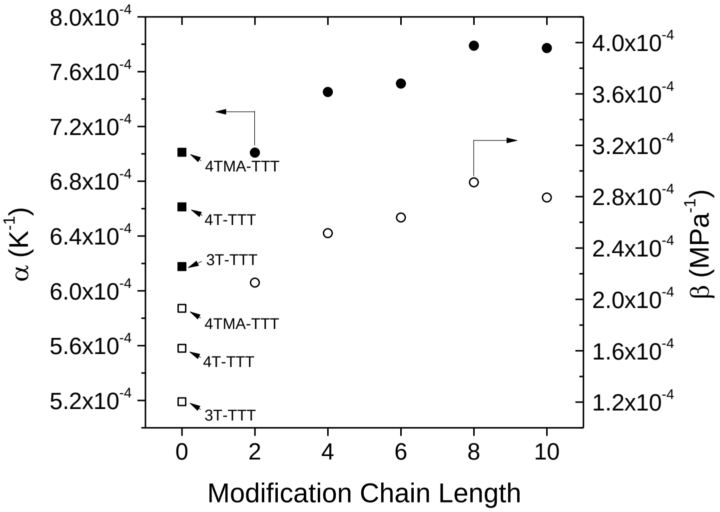

*Figure 46*. Volumetric thermal expansivity, α (●), and isothermal compressibility, ß (○), as a function of perfluoroalkyl chain length.

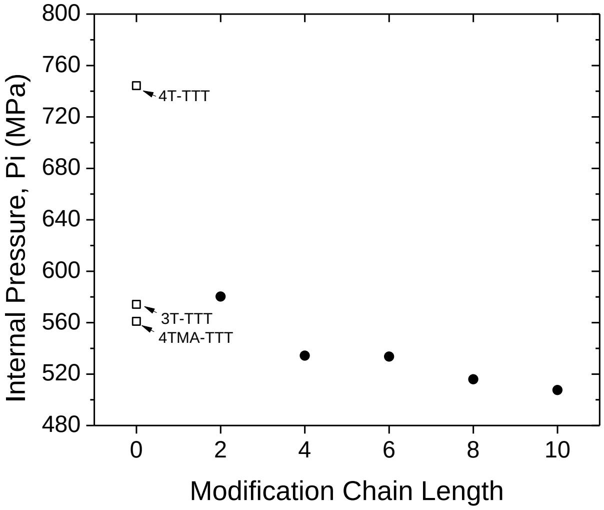

*Figure 47*. Internal pressure as a function of modification length.

The suggestion of an expansion of the network as a result of repulsive forces between the fluorinated substituents and the backbone, where free volume aggregates around the fluorinated chain ends, must result in a redistribution of free volume, and therefore, the concentration of holes per unit mass, $N'_h$, must decrease with an overall increase in the fractional free volume. As seen through PALS data, the hole size increases with increased fluorinated chain length all while the network backbone structure, probed by DMTA, was retained across all modifications. To study the concentration of holes in the modified networks, two approaches were utilized and compared. The first method was first reported by Dlubek where the total specific volume is a sum of the occupied and free volumes[33]

Equation 23 $V_{sp} = V_{occ} + V_f$

where $V_{occ}$ is the occupied volume and $V_f$ is the specific free volume. Furthermore, $V_f$, can be described by a concentration and size of free volume holes:

Equation 24 $V_{sp} = V_{occ} + N_h' \langle v_h \rangle$

$V_{sp}$ and $<v_h>$ were determined using PVT and PALS, respectively. The fractional free volume can then be determined from

Equation 25 $FFV = \frac{(V_{sp} - V_{occ})}{V_{sp}}$

$V_{sp}$ versus $<v_h>$ for the determination of $V_{occ}$ and $N'h$ is plotted in Figure 48. Vertical lines in Figure 42 at 27.5 °C and 57.5 °C indicate the melt state temperature prior to the onset of o-Ps bubbling at the knee temperature, $T_k$, described by Winberg.[30] This finite range of temperatures set the limits to the fit $V_{sp}$ v. $<v_h>$ data. The lower temperature limit for this analysis was set to be greater than $T_g$ and the lower limit of PVT. Upper limits were determined to be lower than $T_k$ to negate any effects of o-Ps bubbling. From these linear regressions, $V_{occ}$ and $N'_h$ were determined using Equation 24. Results from these calculations are shown in Table 4.2. It is readily apparent that $N'_h$, acquired from the slope of $V_{sp}$ v. $<v_h>$ decreased as perfluoroalkyl chain length increased. The fit of 4T-TTT data also shows the impact of higher cross link density on $N'_h$ as 4T-TTT has a considerably greater $N'_h$ than the remainder of the studied networks.

The second method to determine the concentration of holes used Simha-Somcymsky equations of state. To determine the occupied volume, $V_{occ}$, using PVT, $V_{sp}$ data is analyzed using Simha-Somcymsky equations of state. The equations of state consider a lattice model, with 12 degrees of freedom, to describe the behavior of a liquid where sites are either occupied or considered vacant. Determination of the relative quantity of vacant lattice sites, h, or holes, allows for the determination of FFV. Further analysis of the lattice parameters allow for the evaluation of lattice point mass and volume. These parameters give more insight into the molecular scale behavior of the network and free volume distribution.

Table 3

*Network volumetric data and analysis from Dlubek and SS-EOS equations. Occupied volume,* $V_{occ}$*, hole concentration,* $N'_h$*, specific free volume,* $V_f$*, and fractional free volume, FFV.*

| | | **Dlubek Analysis** | | | | **SS-EOS** | | |
|---|---|---|---|---|---|---|---|---|
| **Material** | **$V_{sp}$ (cc/g)** | **$V_{occ}$ (cc/g)** | **1000 * N'h (mol/g)** | **$V_f$ (cc/g)** | **FFV (Dlubek)** | **$V_{occ}$ (cc/g)** | **$V_f$ (cc/g)** | **FFV (SS-EOS)** |
| 4Tf2-TTT | 0.736 | 0.703 | 0.85 | 0.034 | 0.046 | 0.634 | 0.102 | 0.138 |
| 4Tf4-TTT | 0.721 | 0.682 | 0.71 | 0.035 | 0.049 | 0.619 | 0.102 | 0.142 |
| 4Tf6-TTT | 0.717 | 0.650 | 0.60 | 0.061 | 0.086 | 0.614 | 0.103 | 0.144 |
| 4Tf8-TTT | 0.702 | 0.632 | 0.47 | 0.068 | 0.097 | 0.599 | 0.103 | 0.147 |
| 4Tf10-TTT | 0.678 | 0.644 | 0.27 | 0.037 | 0.054 | 0.577 | 0.100 | 0.149 |
| 4T-TTT | 0.787 | 0.711 | 1.58 | 0.046 | 0.061 | 0.688 | 0.099 | 0.126 |
| 3T-TTT | 0.757 | 0.753 | 1.11 | 0.037 | 0.047 | 0.662 | 0.095 | 0.125 |
| 4TMA-TTT | 0.763 | 0.716 | 0.97 | 0.051 | 0.066 | 0.662 | 0.102 | 0.133 |

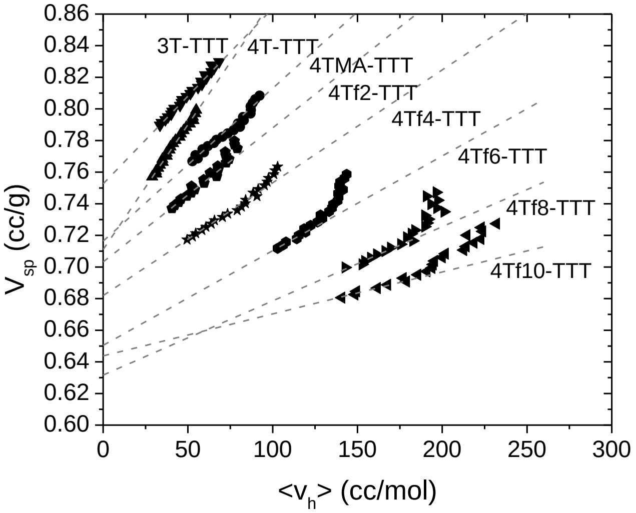

*Figure 48*. $V_{sp}$ from PVT and SS-EOS are plotted against <$v_h$> from PALS from 30 °C to 125°C.

The PVT behavior of many amorphous fluorinated linear polymers[34,35] has been described by a simplified equation of state by Utracki and Simha[36] in the equilibrium melt state using

Equation 26 $$V(P,T) = V^* * exp\left(a_0 + a_1(\tilde{T})^{\frac{3}{2}} + (\tilde{P})\left[a_2 + \left(a_3 + a_4(\tilde{P}) + a_5(\tilde{P})^2\right) * (\tilde{T})^2\right]\right)$$

Equation 27 $$\tilde{P} = \frac{P}{P^*} \quad \tilde{T} = \frac{T}{T^*} \quad \tilde{V} = \frac{V}{V^*}$$

where $\tilde{P}$, $\tilde{T}$, and $\tilde{V}$ are reduced parameters and $P^*$, $T^*$, and $V^*$ are fit parameters.[34] Table 4 shows the $P^*$, $T^*$, and $V^*$ used in all of the fits for all studied films. Constants $a_0$ through $a_5$ are described by Utracki and Simha as: $a_0$= -0.10346, $a_1$= 23.854, $a_2$= -0.1320, $a_3$= -33.7, $a_4$= 1032.5, $a_5$= -1329.9.[36] The conventional method to fit $V_{sp}$ data from PVT experiments at ambient conditions is to consider $P$ = 0 MPa and therefore $\tilde{P}$ = 0 reducing SS-EOS to[36,37,38]

Equation 28 $$V(P,T) = V^* * exp\left(a_0 + a_1 \left(\frac{T}{T^*}\right)^{\frac{3}{2}}\right)$$

Figure 49 shows the *ln(V)* dependence on the reduced temperature, $T^{3/2}$, for all of the control and modified networks. T*, a function of the slope of *ln(V)* versus $T^{3/2}$ relationships, is similar for all modified networks but was noticeably different for the higher cross linked 4T-TTT system.

While the SS-EOS model has been used to study linear polymers and elastomers,[34] here we attempt to apply the established methodology to these highly cross linked thiol-ene networks. All PVT data was collected in the melt state, well above the $T_g$ as shown for 4Tf2-TTT in Figure 45. The temperature dependence of $V_{sp}$ and the SS-EOS fits for all samples at 0 MPa are plotted in Figure 50. All fits showed sufficient agreement with the model with $R^2$ being greater than 0.99. To determine P*, both T* and V* were held constant across all high pressure isobars and a least squares fit was applied to Equation 28. As performed by Dlubek[34], an average P* was determined from individual P* least squares fits and applied to all isobars. P* is listed for each material in Table 4.

Table 4

*SS-EOS reduced parameters V*, T*, and P* used to fit $V_{sp}$ data. $M_0$ and $V_0$ are the molecular weight and volume of lattice points respectively.*

| **Material** | **V*** | **T*** | **P*** | **$M_0$ (g/mol)** | **$V_0$ (Å³)** |
|---|---|---|---|---|---|
| 4Tf2-TTT | 0.7391 | 11271 | 1126 ± 13 | 37.52 | 45.86 |
| 4Tf4-TTT | 0.7203 | 10853 | 1036 ± 31 | 40.32 | 48.29 |
| 4Tf6-TTT | 0.7144 | 10707 | 1015 ± 18 | 40.99 | 48.81 |
| 4Tf8-TTT | 0.6974 | 10474 | 962 ± 26 | 43.26 | 50.43 |
| 4Tf10-TTT | 0.7066 | 10582 | 910 ± 34 | 46.50 | 52.34 |
| 4T-TTT | 0.7638 | 11846 | 1151 ± 46 | 37.30 | 46.90 |
| 3T-TTT | 0.8034 | 12585 | 1048 ± 31 | 41.42 | 54.17 |
| 4TMA-TTT | 0.7716 | 11704 | 1146 ± 15 | 36.49 | 46.27 |

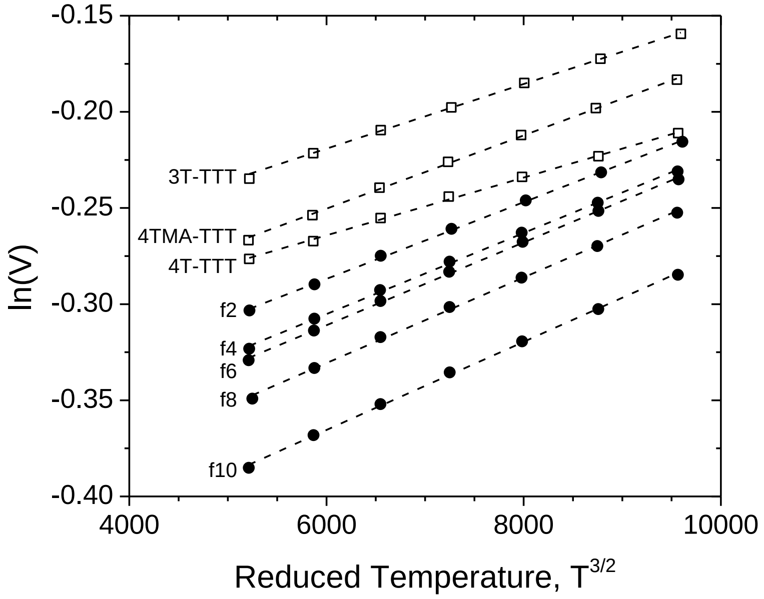

*Figure 49*. 0 MPa fits of the temperature dependence of $V_{sp}$ were determined by plotting ln(V) as a function of $T^{3/2}$.

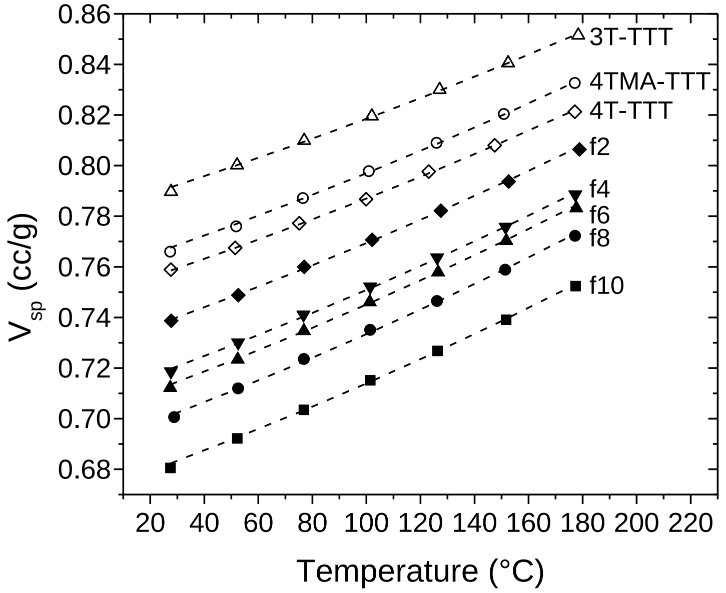

*Figure 50*. $V_{sp}$ versus temperature data with SS-EOS fits.

Using the SS-EOS, it was possible to estimate the occupied fraction of lattice sites in these networks using[34]

Equation 29 $$\frac{\tilde{P}\tilde{V}}{\tilde{T}} = \left[1 - y\left(2^{\frac{1}{2}}\, y\, \tilde{V}\right)^{-\frac{1}{3}}\right]^{-1} + \frac{y}{\tilde{T}}\left[2.002\left(y\, \tilde{V}\right)^{-4} - 2.409\left(y\, \tilde{V}\right)^{-2}\right]$$

where y is the fraction of occupied lattice sites. Fractional free volume was determined using Equation 25 where $V_{occ} = V_{sp} * h$. Table 3 shows the $V_{occ}$, $V_f$, and *FFV* determined from SS-EOS. The reported values suggest a gradual increase in fractional free volume as a function of modification length. This increase in free volume was not evident in density measurements as the increase in the mass of a unit volume had a large impact on density than the increase fractional free volume.

As shown in Table 3, there is a disagreement between the Dlubek *FFV* and that acquired by SS-EOS. This difference can be a result of the different methods of determination and the dependence on PALS data for the Dlubek analysis. As discussed previously, the PALS data for nearly all of the networks show o-Ps bubbling at temperatures greater than $T_k$. Considering the possibility of bubbling, the $V_{sp}$ dependence on $<v_h>$ may be under estimated here. Data acquired from PVT measurements and SS-EOS give reasonable supporting data showing an increase in fractional free volume as chain length increases using a methodology that is not prone to the limits of o-Ps formation and lifetime. Also, considering 3T-TTT and the modified networks 4TMA-TTT, 4Tf2-TTT, and 4Tf4-TTT that do not show the o-Ps plateau in PALS data, $N'_h$ decreased and the *FFV* increased as the perfluoroalkyl chain length increased.

The relative intensity of o-Ps determined from PALS data has been suggested to be an indicator of hole concentration in polymeric systems[39] and also affected by the chemical environment of the probed void.[40] Since the meaning of the relative intensity has been subject to scrutiny, is dependent on various chemical and experimental factors, and its utility as an indicator of hole concentration has been debated,[41] we approached the meaning of $I_{o\text{-}Ps}$ delicately and only show the effect of perfluoroalkyl modifications on $I_3$. Figure 51 displays the relative intensity of $I_3$ as a function of perfluoroalkyl modification length and suggests that the concentration of holes decreases as the tethered modification length increases.

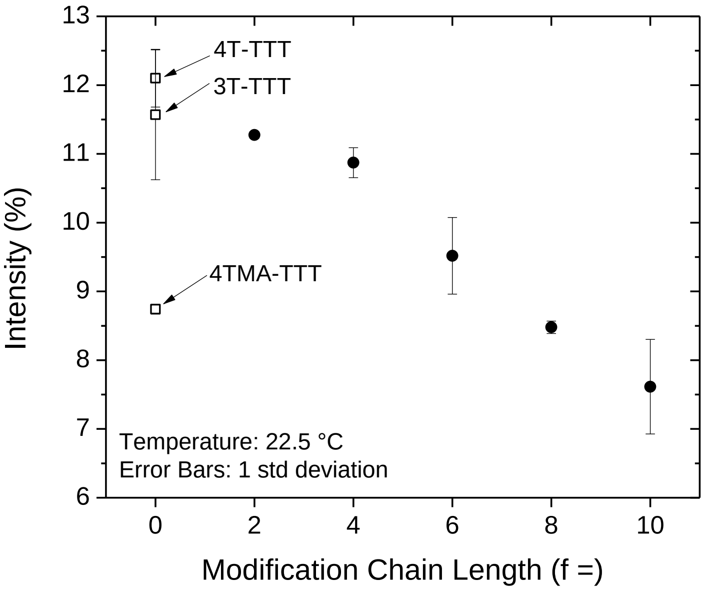

*Figure 51*. The relative intensity of o-Ps as a function of perfluoroalkyl modification, X for all 4TfX-TTT networks and controls shown at a modification length of 0.

For linear polymers, the molecular weight of each SS-EOS lattice point, $M_0$, can be determined using the reduction parameters *V**, *T**, and *P** and the equation:

$$\text{Equation 30} \quad M_0 = R\frac{T^*}{3P^*V^*}$$

where *R* is the universal gas constant. Here we applied this model to estimate the volume of each lattice site at ambient conditions using $M_0$ and the bulk density, $\rho$, of the network. The volume of the lattice points, $V_0$, was therefore estimated using[42]

$$\text{Equation 31} \quad V_0 = \frac{M_0}{\rho}$$

$M_0$ and $V_0$ are listed in Table 3. These lattice site dimensions are comparable in scale to those found in fluorinated elastomers investigated by Dlubek.[42] We see that the molecular weight of the lattice points increase along with the volume of the lattice points with increased perfluoroalkyl length. Considering the increase in bulk network density as a function of increased perfluoroalkyl chain length discussed earlier, the observation of an increased lattice site volume suggests that there was a molecular scale expansion of the network occurring as longer chain ends were incorporated.

The volume of individual lattice points, $V_o$, and the size of free volume elements probed by PALS, $<v_h>$, suggest the free volume elements actually occupy several adjacent lattice points. For example $V_0$ for 4Tf2-TTT is 45.8 Å³ and $<v_h>$ is 67 Å³ and 4Tf10-TTT has a lattice point volume estimated to be 52 Å³ with a $<v_h>$ of 233 Å³. Therefore, the average number of adjacent vacant lattice sites increases with increasing modification chain length from 1.47 free lattice sites per hole in 4Tf2-TTT and 4.70 and 4.46 sites per hole in 4Tf8-TTT and 4Tf10-TTT respectively. With the increase in perfluoroalkyl chain length, it seems that the free volume redistributed from the backbone network to increase the free volume around the tethered, perfluoroalkyl chains.

## Conclusions

The modification of a tetrafunctional thiol with monofuctional perfluoroalkyl acrylates of increasing length via a thiol-Michael addition followed by the photopolymerization with a trifunctional ene showed fluorine modifications had no measureable effect on the overall cure of the network. As the length of the perfluoroalkyl chain was increased, the PALS probed free volume hole size was increased over 2.5 times while the networks retained similar DSC probed glass transition temperatures. Rubbery modulus and $T_g$ data suggest that there was not a significant change in the network topology as the perfluoroalkyl length was increased. Free volume analysis using PVT dilatometry indicates that the fractional free volume increases slightly with increased fluorinated chain length all while density increased as a result of the high density of fluorinated atoms. Internal pressure data suggests a moderate increase in repulsion of atoms in the network as the modification length was increased caused by incompatible fluorine being covalently bound within the network. Wide angle X-ray data confirms the expansion of the network caused by the perfluoroalkyl chains as the intersegmental distance between neighboring network atoms increased as evidenced by an amorphous halo shift toward higher d-spacings. The seamless incorporation of fluorine into such thiol-ene networks shows that the kinetics of UV-curing are fast enough to spatially lock into place incompatible chemical structures that are miscible in the monomer mixture but are thermodynamically driven to phase separate after curing causing a molecular scale expansion of free volume holes a redistribution of hole free volume.

## References

(1) Riess, J. G. Chemical Reviews 2001, 101, 2797.

(2) Hellums, M. W.; Koros, W. J.; Husk, G. R.; Paul, D. R. Journal of Membrane Science 1989, 46, 93.

(3) Robeson, L. M. Journal of Membrane Science 2008, 320, 390.

(4) Alentiev, A. Y.; Yampolskii, Y. P.; Shantarovich, V. P.; Nemser, S. M.; Platé, N. A. Journal of Membrane Science 1997, 126, 123.

(5) Sangermano, M.; Bongiovanni, R.; Malucelli, G.; Priola, A.; Pollicino, A.; Recca, A. Journal of Applied Polymer Science 2003, 89, 1524.

(6) Bongiovanni, R.; Malucelli, G.; Pollicino, A.; Priola, A. Journal of Applied Polymer Science 1997, 63, 979.

(7) Hwang, H.-D.; Kim, H.-J. Journal of Colloid and Interface Science 2011, 362, 274.

(8) Priola, A.; Bongiovanni, R.; Malucelli, G.; Pollicino, A.; Tonelli, C.; Simeone, G. Macromolecular Chemistry and Physics 1997, 198, 1893.

(9) Mukerjee, P.; Yang, A. Y. S. The Journal of Physical Chemistry 1976, 80, 1388.

(10) Glöckner, P. Radiation Curing: Coatings and Printing Inks ; Technical Basics, Applications and Trouble Shooting; Vincentz Network, 2008.

(11) Hoyle Charles, E. In Radiation Curing of Polymeric Materials; American Chemical Society: 1990; Vol. 417, p 1.

(12) Hoyle, C. E.; Lowe, A. B.; Bowman, C. N. Chemical Society Reviews 2010, 39, 1355.

(13) Hoyle, C. E.; Lee, T. Y.; Roper, T. Journal of Polymer Science Part A: Polymer Chemistry 2004, 42, 5301.

(14) Hoyle, C. E.; Bowman, C. N. Angewandte Chemie 2010, 122, 1584.

(15) Kwisnek, L.; Kaushik, M.; Hoyle, C. E.; Nazarenko, S. Macromolecules 2010, 43, 3859.

(16) Kwisnek, L.; Nazarenko, S.; Hoyle, C. E. Macromolecules 2009, 42, 7031.

(17) Shin, J.; Nazarenko, S.; Hoyle, C. E. Macromolecules 2009, 42, 6549.

(18) Clark, T.; Kwisnek, L.; Hoyle, C. E.; Nazarenko, S. Journal of Polymer Science Part A: Polymer Chemistry 2009, 47, 14.

(19) Cheng, S. Z. D.; Cao, M. Y.; Wunderlich, B. Macromolecules 1986, 19, 1868.

(20) Zoller, B., Pahud, Ackermann Review of Scientific Instruments 1976, 47, 948.

(21) Olson, B. G.; Lin, J.; Nazarenko, S.; Jamieson, A. M. Macromolecules 2003, 36, 7618.

(22) Kirkegaard, P.; Eldrup, M.; Mogensen, O. E.; Pedersen, N. J. Computer Physics Communications 1981, 23, 307.

(23) Ameduri, B.; Bongiovanni, R.; Lombardi, V.; Pollicino, A.; Priola, A.; Recca, A. Journal of Polymer Science Part A: Polymer Chemistry 2001, 39, 4227.

(24) Gaynor, J.; Schueneman, G.; Schuman, P.; Harmon, J. P. Journal of Applied Polymer Science 1993, 50, 1645.

(25) Miyasaka, M.; Koike, N.; Fujiwara, Y.; Kudo, H.; Nishikubo, T. Polym J 2011, 43, 325.

(26) Starkweather, H. W.; Zoller, P.; Jones, G. A.; Vega, A. J. Journal of Polymer Science: Polymer Physics Edition 1982, 20, 751.

(27) Fox, H. W.; Zisman, W. A. Journal of Colloid Science 1950, 5, 514.

(28) Tao, S. J. Journal of Chemical Physics 1972, 56.

(29) Eldrup, M.; Lightbody, D.; Sherwood, J. N. Chemical Physics 1981, 63, 51.

(30) Winberg, P.; Eldrup, M.; Maurer, F. H. J. The Journal of Chemical Physics 2012, 136.

(31) Slutsker, A. I.; Filippov, V. E. Polymer Science U.S.S.R. 1988, 30, 2556.

(32) C. O'brien, K.; Koros, W. J.; Husk, G. R. Journal of Membrane Science 1988, 35, 217.

(33) Dlubek, G.; Stejny, J.; Alam, M. A. Macromolecules 1998, 31, 4574.

(34) Dlubek, G.; Sen Gupta, A.; Pionteck, J.; Krause-Rehberg, R.; Kaspar, H.; Lochhaas, K. H. Macromolecules 2004, 37, 6606.

(35) Dlubek, G.; Pionteck, J.; Sniegocka, M.; Hassan, E. M.; Krause-Rehberg, R. Journal of Polymer Science Part B: Polymer Physics 2007, 45, 2519.

(36) Utracki, L. A.; Simha, R. Macromolecular Theory and Simulations 2001, 10, 17.

(37) Utracki, L. A.; Jamieson, A. M. Polymer Physics: From Suspensions to Nanocomposites and Beyond; Wiley, 2011.

(38) Dlubek, G.; Pionteck, J. Acta Physica Polonica A 2008, 113, 1331.

(39) Kobayashi, Y.; Zheng, W.; Meyer, E. F.; McGervey, J. D.; Jamieson, A. M.; Simha, R. Macromolecules 1989, 22, 2302.

(40) Zhang, R.; Robles, J.; Kang, J.; Samha, H.; Chen, H. M.; Jean, Y. C. Macromolecules 2012, 45, 2434.

(41) Consolati, G.; Quasso, F.; Simha, R.; Olson, B. G. Journal of Polymer Science Part B: Polymer Physics 2005, 43, 2225.

(42) Dlubek, G.; Wawryszczuk, J.; Pionteck, J.; Goworek, T.; Kaspar, H.; Lochhaas, K. H. Macromolecules 2004, 38, 429.

# CHAPTER V

# THIOL-ENE NETWORKS CONTAINING TETHERED PERFLUOROALKYL MOIETIES: TRANSPORT PROPERTIES AND THE THERMODYNAMICS OF MOLECULAR INTERACTIONS

## Abstract

$H_2$, $O_2$, $N_2$, $CO_2$, $CH_4$ transport data is reported for thiol-ene networks modified with tethered perfluoroalkyl acrylates. Increasing modification length of perfluorinated acrylate modified thiol-ene network increases permeability of light gases based on the increase of diffusivity. Gas solubility increases with the gas critical temperature but is not affected by the network modification. A brief discussion is introduced on the internal pressure contribution to the activation energy of diffusion, cohesive energy density, specific heat capacity, and the energy of cavity formation.

## Introduction

Using gases as molecular probes to study polymer morphology has been suggested since the early 1960s.[1,2] Studying diffusion gives another route to estimate the dynamic free volume available which is a result of local fluctuations within a system. Diffusion is dependent on the size of the penetrant, $d$, and the size of, $\langle v_h \rangle$, and distance, $\alpha$, between individual free volume elements. The energy requirement for diffusion jumps can be modeled as

$$\text{Equation 32} \quad E_D = \frac{1}{4}\pi d^2 \alpha \, CED \, N_A$$

where $E_d$ is the activation energy for a penetrant to diffuse to a hole with a given cross sectional area in a system with a given cohesive energy density, $CED$.[2]

Considering CED is driven by intermolecular interactions, the increase in fluorine in previously studied thiol-ene systems, which causes repulsion within the network, would be expected to decrease the activation energy of diffusion.

This Chapter is a continuation of the work highlighted in Chapter II[3] and the work described in Chapter IV.[4] Here, the gas transport properties; specifically permeability, diffusivity, and solubility are quantified. This Chapter also introduces a brief discussion on the role of internal pressure on the diffusion process in regards to the cohesive energy density and the energy of cavity formation.

## Experimental

Sample films were prepared as described in Chapter IV.[4] Test samples were required to be free of pin holes and other abnormalities. Each film was cast with a target thickness of 500 µm and was measured individually in nine locations over the test area, eight around the periphery and one measurement in the center. The thicknesses used for data analysis were the averages of the nine measured thicknesses.

Light gas flux was measured using a custom diffusion lag, constant volume variable pressure setup as described earlier by our group[5] which is based on prior reports of this setup.[6-8] The upstream volume was pressurized to 3.5 atma for $H_2$, $O_2$, $N_2$, $CO_2$, $CH_4$. Tests were initiated by opening a valve between the upstream volume and the film causing a slight drop in the recorded upstream pressure. This slight drop in pressure marked the start of the test and the zero time of the test. Pressure increase from vacuum in the downstream volume was measured with a MKS 226A Baratron differential capacitance manometer with the reference port connected to a vacuum. Data was collected with time resolutions of 0.25 seconds and 1.0 second for fast and slow gases, respectively, until there was an observed steady state pressure increase with time. Tests were performed at 23 °C and measured with a thermocouple located near the sample film. Films were equilibrated at a prescribed temperature while being evacuated for greater than 12 hours prior to testing.

## Results and Discussion

Raw diffusion lag, pressure increase versus time, curves were collected at 23°C. Sample films were measured for thickness yielding an average thickness of 390 µm for the series with a variation of ± 21 µm. Each film was analyzed with its own thickness taken into consideration. Diffusion lag data was collected for $H_2$, $O_2$, $N_2$, $CO_2$, $CH_4$ and each modified thiol-ene network. Figure 52 shows the raw data plots for each of the five materials. Increased perfluoroalkyl chain length drastically shows an improvement in the slope at steady state indicative of increased permeability. Diffusion lag values also show an apparent decrease as a function of increased perfluoroalkyl chain length, evidence of an increased diffusivity.

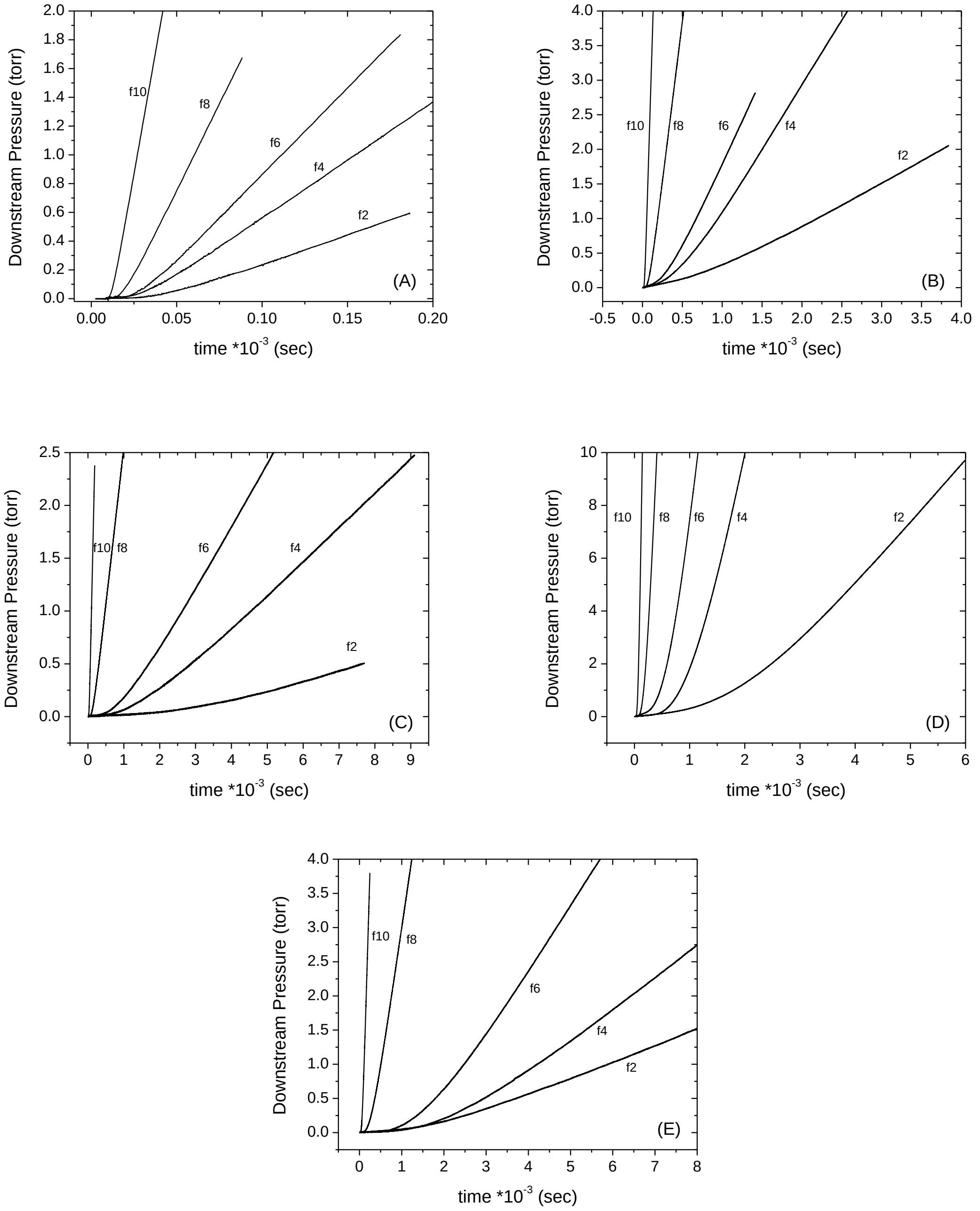

*Figure 52.* Raw diffusion lag plots for all gases $H_2$(A), $O_2$ (B), $N_2$ (C), $CO_2$ (D), $CH_4$ (E) and modification lengths. Note the scales are different for each plot to show sufficient detail of all experiments.

Transport parameters were calculated from time lag diffusion pressure increase versus time data collected according to conventional diffusion lag techniques.[9] Permeability (P) was determined from the results of a linear regression of the steady state pressure increase versus time, $(dp_1/dt)_{ss}$, and calculated using,

$$\text{Equation 33:}\quad P_A = \frac{V_d l}{p_2 ART}\left[\left(\frac{dp_1}{dt}\right)_{ss} - \left(\frac{dp_1}{dt}\right)_{leak}\right]$$

where $V_d$ is the downstream volume, $l$ is the film thickness, $p_2$ is the upstream pressure, A is the exposed area of the film, $R$ is the universal gas constant, $T$ is the absolute temperature of the downstream volume, and $(dp_1/dt)_{leak}$ is the leak slope determined prior to exposing the test gas to the film.[6] For all tests, $(d_{p1}/d_t)_{leak}$ was less than 0.005 torr/minute and considered negligible. The steady state pressure increase regression was extrapolated to zero pressure using Origin 8.6 software. The x-intercept was defined as the time lag, $\theta$. The time lag was used to calculate the diffusivity, $D$ utilizing Equation 33.[10] Using permeability and diffusivity, solubility was calculated using $S = P / D$.

$$\text{Equation 34}\quad D = \frac{l^2}{6\theta}$$

Light gas permeability is plotted in Figure 53. The size dependence of permeability was immediately apparent in this plot as $H_2$, the smallest of the studied gases, shows a change of an order of magnitude but $N_2$ and $CH_4$ permeability shows a change of two orders of magnitude in 4Tf10-TTT compared to the 4Tf2-TTT. The gradual increase in the permeability as a function of perfluoroalkyl chain length suggested that there was not a drastic change in morphology, packing or free volume, rather, the change was sequential as the size of the modification increased.

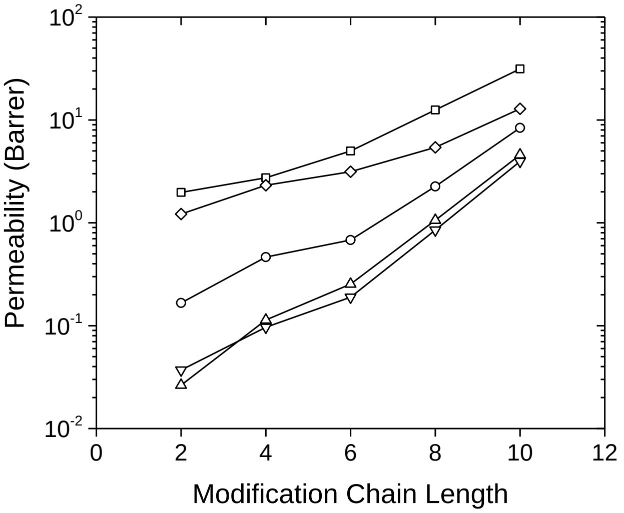

*Figure 53.* Permeability of $H_2$(◇), $O_2$ (○), $N_2$ (▽), $CO_2$ (□), $CH_4$ (△) in modified thiol-ene networks.

Analyzing the differences in gas sizes, shown in Table 5, and the knowledge of the free volume hole size from Chapter IV, the trend toward the merging of permeability values suggest that the hole size was approaching a critical maximum value where transport was no longer selective based on size alone. Diffusivity data reflects this as all gas diffusivities increase over the studied modification range except for $H_2$ which was less affected by the change in free volume. Diffusivity is plotted in Figure 54 and shows that $H_2$ increases half an order of magnitude where all other gases increase nearly one and a half orders.

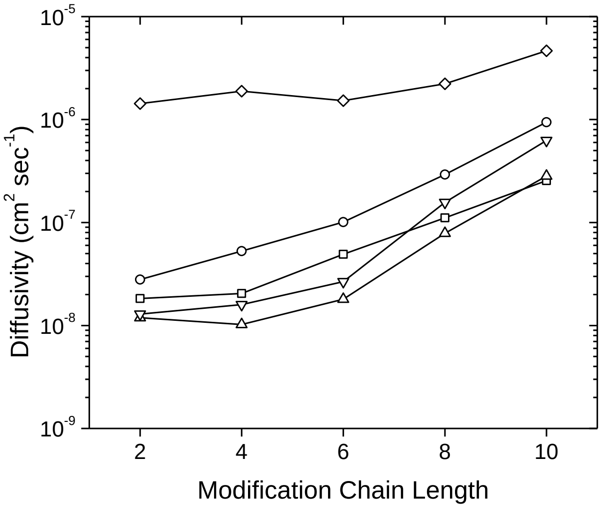

*Figure 54.* Diffusivity of $H_2$(◇), $O_2$ (○), $N_2$ (▽), $CO_2$ (□), $CH_4$ (△) in modified thiol-ene networks.

Reexamining Equation 34, the diffusion coefficient can be rewritten as

Equation 35 $$D = \frac{1}{6}\omega\alpha^2$$

where ω is the effective jump frequency.[2] With this understanding, and making the assumption that all diffusion jumps are the same length based on the consistency of the network shown in Chapter IV, the jump frequency increases as the modification length increases. Furthermore, an increase in jump frequency suggests a decrease in the activation energy for diffusion, $E_d$, and therefore a decrease in *CED* as expressed in Equation 32. This was supported by the decrease in internal pressure, $p_i$, shown in Chapter IV, where *CED* and internal pressure are related by[11]

Equation 36 $\widetilde{CED} = \frac{\tilde{U}}{\tilde{T}}$

Equation 37 $\tilde{p_\iota} = \left(\frac{\partial \tilde{U}}{\partial \tilde{V}}\right)_{\tilde{T}}$

Equation 38 $p_i = T\left(\frac{\alpha}{\beta}\right) - p$

The “~” indicates reduced parameters of *CED,* internal energy, *U*, temperature, *T*, and volume, *V*. *α* and *ß* are the volumetric thermal expansivity and isothermal compressibility, respectively. Ramos suggests that the internal pressure plays a fundamental role in the determination of the energy of cavity formation in liquids.[12] If we extend this rationale to these polymer systems, it suggests that the decrease in internal pressure causes a decrease in the energy of cavity formation. A decrease in the energy of cavity formation may also be related to the hole size of free volume cavities which was shown to increase drastically with modifications shown in Chapter IV. This concept must be explored further.

Table 5

*Kinetic diameters and critical temperatures of the studied penetrant gases*

| Gas | Critical Temperature $T_C$ (K) | Kinetic Diameter $d_k$[14] (Å) |
|---|---|---|
| $H_2$ | 33.2 | 2.89 |
| $N_2$ | 126.2 | 3.64 |
| $O_2$ | 154.6 | 3.46 |
| $CH_4$ | 190.6 | 3.8 |
| $CO_2$ | 304.2 | 3.3 |

In Chapter IV we also see a change in $\Delta c_p$ as a result of increasing modification length along with a very slight change in thermal expansivity, $\alpha$, of the system. The change internal energy must be large enough to cause a decrease in the $\Delta c_p$ to overcome the contributions of an increase in thermal expansivity when considering the specific heat capacity, $c_p$, according to[13]

$$\text{Equation 39} \quad c_p = \left(\frac{\partial(U+pV)}{\partial T}\right)$$

The study of the combination of these theories will be continued in further work.

Shown in Figure 55, the solubility was not impacted by the series of modifications. $CO_2$ has the highest solubility as a result of its high critical temperature compared to the other gases. The solubility actually scales very well with the critical temperature of each gas. Critical temperatures are shown in Table 5.1. Changes in permeability can therefore be attributed to the change in diffusivity primarily, suggesting the modifications expand the network.

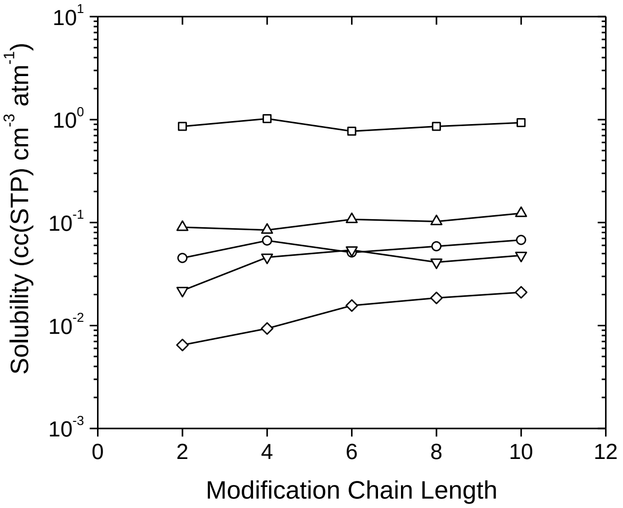

*Figure 55*. Solubility of $H_2$(◇), $O_2$ (○), $N_2$ (▽), $CO_2$ (□), $CH_4$ (△) in modified thiol-ene networks.

## Conclusions

Transport properties of perfluorinated acrylate modified thiol-ene networks are reported for $H_2$, $O_2$, $N_2$, $CO_2$, and $CH_4$. An increase in permeability was realized for all gases as the modification length increased from f2 to f10. Larger gases showed nearly two and a half orders of magnitude increases in permeability as a result of increased diffusivity in the system. Solubility remained nearly constant across all modifications for all gases. A discussion was raised on the relationship of internal pressure and activation energy of diffusion, cohesive energy density, specific heat capacity, and the energy of cavity formation.

## References

(1) Michaels, A. S.; Bixler, H. J. *Journal of Polymer Science* **1961**, *50*, 413.

(2) Hiltner, A.; Liu, R. Y. F.; Hu, Y. S.; Baer, E. *Journal of Polymer Science Part B: Polymer Physics* **2005**, *43*, 1047.

(3) Goetz, J.; Kwisnek, L.; Nazarenko, S. *RadTech Report* **2012**, *27*, 27.

(4) Goetz, J.; Greenhoe, B.; Kwisnek, L.; Nazarenko, S. *Manuscript in Preparation* **2014**.

(5) Kwisnek, L.; Heinz, S.; Wiggins, J. S.; Nazarenko, S. *Journal of Membrane Science* **2011**, *369*, 429.

(6) Lin, H.; Freeman, B. D. *Journal of Membrane Science* **2004**, *239*, 105.

(7) Lin, H.; Wagner, E. V.; Swinnea, J. S.; Freeman, B. D.; Pas, S. J.; Hill, A. J.; Kalakkunnath, S.; Kalika, D. S. *Journal of Membrane Science* **2006**, *276*, 145.

(8) Raharjo, R. D.; Lin, H.; Sanders, D. F.; Freeman, B. D.; Kalakkunnath, S.; Kalika, D. S. *Journal of Membrane Science* **2006**, *283*, 253.

(9) Lin, H.; Freeman, B. D. *Macromolecules* **2006**, *39*, 3568.

(10) Daynes, H. A. *Proceedings of the Royal Society of London. Series A* **1920**, *97*, 286.

(11) Utracki, L. A.; Jamieson, A. M. *Polymer Physics: From Suspensions to Nanocomposites and Beyond*; Wiley, 2011.

(12) Ramos, J. J. M. *J Solution Chem* **1989**, *18*, 957.

(13) Van Krevelen, D. W.; Te Nijenhuis, K. In *Properties of Polymers (Fourth Edition)*; Krevelen, D. W. V., Nijenhuis, K. T., Eds.; Elsevier: Amsterdam, 2009, p 109.

(14) Breck, D. W. *Zeolite molecular sieves: structure, chemistry, and use*; Wiley, 1973.

# CHAPTER VI

# THERMOTROPIC, SIDE-CHAIN ORDERED POLYMERIC COATINGS: GAS PERMEABILITY SWITCHING VIA A THERMAL STIMULUS

## Abstract

Rapid access to large areas of stimuli responsive materials is attractive in the field of membrane science for purification systems and molecular valves. Thermotropic liquid crystalline (LC) systems show sharp property changes through the smectic-LC transition induced by temperature. Comparison of similar amorphous and liquid crystalline systems allows for the elucidation of the characteristics of LC phase. Lightly cross linked $C_6F_{13}$ and $C_8F_{17}$ perfluorinated side-chain acrylate networks were UV cured as thin films resulting in amorphous and thermotropic liquid crystalline thin films, respectively. Thermal and morphological characterization indicates a restructuring of the liquid crystalline phase through the isotropic transition giving rise to increase in transport and free volume properties. The amorphous film showed no dramatic change in transport or free volume properties.

## Introduction

Stimuli responsive materials change physical properties under stimuli such as temperature, pH, or light. Stimuli responsive materials are attractive for protective coatings and provide unique property advantages. Specifically, the ability to tailor surface and transport properties is important in the application of food packaging,[1] small gas purification and permeation switches, breathable clothing, and controlled small molecule release.[2]

Side chain molecular order provides a means to develop thermally responsive materials. In particular, in aliphatic comb-shaped polymers, when temperature is increased above the side-chain melting temperature, a transition in the morphology takes place. In aliphatic comb-shaped materials, the disruption of side-chain arrangement gave rise to an increase in small gas permeability of more than an order of magnitude.[3,4] Yet, little is known about the responsive nature of transport properties in materials that display side-chain liquid crystalline morphologies.

Rigid rod, perfluorinated comb-shaped acrylate materials have been of great interest for the past few decades for their unique surface and transport properties.[5-7] At a critical perfluorinated chain length,[5] the rigid rod structure in the side chain causes a well-defined, smectic ordered structure.[7] At elevated temperatures, a disruption of side chain order occurs as the morphology transitions from smectic order to isotropic. This transition has shown to considerably increase the permeability of liquid water/organic mixtures,[8] but small molecule transport property changes have not been explored.

This investigation will study two chemically similar elastomers prepared using UV polymerization, one amorphous and one side chain liquid crystalline elastomer. Previously, liquid crystalline perfluorinated materials have been polymerized radically and solvent cast.[5-8] UV polymerization will be explored to take advantage of the characteristic rapid kinetics and solvent free preparation. This study will focus on the morphological, thermal, free volume, and small gas transport properties of perfluorinated acrylate amorphous and liquid crystalline elastomer thin films below and above the thermotropic transition. By comparing the liquid crystalline phase of $C_8F_{17}$ based polymer films to an amorphous C6F13 analog, the effect of the LC phase can be observed and quantified.

## Experimental

### *Material Preparation*

Mesogenic monomer, 2-perfluorooctyl ethyl acrylate (LC-PFDA), and amorphous monomer, 2-perfluorohexyl ethyl acrylate (A-PFOA), were acquired from Fluoryx, Inc (San Leandro, CA). Cross linking monomer, 1H,1H,6H,6H-perfluorohexyldiacrylate, (OFHD) was acquired from Oakwood Products (West Columbia, SC) and the photo initiator, IRGACURE 2020 (PI), was acquired from Ciba Specialty Chemicals. All materials are shown in Figure 56 and were used as received.

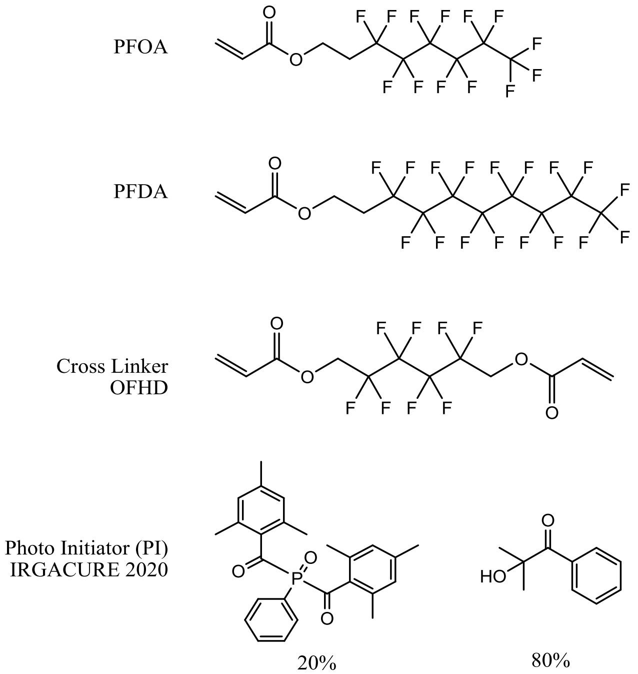

*Figure 56*. Structures of amorphous PFOA, mesogenic PFDA monomers and di-functional OFDA cross linker.

Slightly cross linked polymer thin films were prepared using a UV-initiated radical polymerization. Monomer mixtures of 98 wt% actylate monomer, 1 wt% OFHD, and 1 wt% PI, were prepared in 5 g batches and sonicated for 15 minutes at ambient conditions to ensure complete dispersion of photo initiator and cross linker. Homogeneous mixtures were poured onto clean glass sheets and a subsequent glass sheet was placed on top to yield a consistent liquid mixture thickness. Glass shims were used to define the ultimate thickness the film. Glass, monomer, glass stacks were fed through a Fusion UV Systems EPIQ 6000 high intensity UV line. Each sample was exposed to ten passes under a lamp with an irradiance of 3.1 W/cm$^2$ at a speed of 3 m/min.

Under high intensity UV exposure, monomers conversion occurred rapidly. Slight oxygen inhibition was observed near the edges of the film causing some low molecular weight liquid to be left on the glass. These areas were exposed to ambient air during curing allowing for oxygen inhibition but the bulk of the material, covered by glass, was able to fully cure. Areas around the perimeter of the sample were removed and only the fully cured material was used for the remainder of this study. Figure 57 displays the physical difference between the two materials at ambient conditions. The LC-PFDA sample was an opaque, rigid, glassy thin film and the A-PFOA sample was a transparent, very flexible elastomer. To aid in sample removal, A-PFOA samples were chilled at -35 °C in a freezer for 15 minutes and then lifted from the glass substrate. Thin film thickness was measured between 370 and 550 microns depending on the sample.

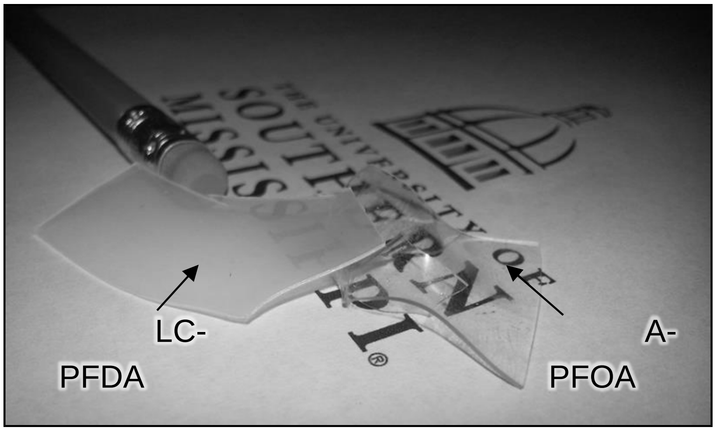

*Figure 57.* LC-PFDA and A-PFOA films at ambient conditions.

*Characterization*

Wide angle X-Ray Diffraction (WAXD) was performed on thin films using a Rigaku Ultima III diffractometer (Cu Kα radiation, λ = 1.542Å) with a step size 0.2 degrees 2θ at a rate of 0.25 steps/min in the range of 2 to 40 degrees 2θ. WAXD spectra were collected at ambient conditions (21°C). Differential scanning calorimetry (DSC) was performed using a TA Instruments DSC Q2000. Thermograms were collected at a heating rate of 10 °C/min and a cooling rate of 5°C/min with a minimum and maximum temperature of -70 °C to 175 °C respectively. The glass transition temperature was determined using a mid-point, average slope method where the thermogram in the melt and glassy regions was fit with a linear line. The average of the melt and glassy state fits was used to find Tg at the intersection of the mid-line and the raw thermogram.

$CO_2$ permeability was determined using a constant volume variable pressure (CVVP) instrument, built in-house, as described in our group's previous work[9] and based upon a reported design.[10-12] Thin film thickness was determined by taking the average of nine measurements over the area available for gas permeation. Upstream pressures were held constant at 2.5 ± 0.2 atm and temperature control was achieved using a fluid circulator used to heat and cool the permeation cell. Permeability was determined from 25°C to 80°C in 5° increments. Downstream pressure was recorded as a function of time with a time resolution as low as 0.5 seconds. Steady state permeation, as indicated by a linear pressure increase v. time, was fit using Origin 8.0 software (Northampton, MA) where $R^2$ values were commonly greater than 0.99997. Permeability was calculated using

Equation 40: $$P = \frac{V_d l}{p_2 ART}\left[\left(\frac{dp_1}{dt}\right)_{ss} - \left(\frac{dp_1}{dt}\right)_{leak}\right]$$

where $P$ is permeability, $V_d$ is the downstream volume, $l$ is the film thickness, $A$ is the film area exposed to the permeate gas, $R$ is the gas constant, $T$ is the temperature, and $dp_1/dt$ is the steady state pressure increase in the downstream volume.[12,18]

Positron annihilation lifetime spectroscopy (PALS) was performed on a fast-fast coincidence system based on a setup described by Jamieson et. al[13] with an average resolution FWHM of 285 ps and a time/channel resolution of 0.0048 ns/channel. Thin film samples were stacked to a total thickness >1mm and contained in aluminum foil packets. The foil wrapped Na22 source was sandwiched between two sample packets. The sandwiched assembly was placed in a vacuum chamber and photomultiplier assemblies (Hamamatsu H3378-50), equipped with $BF_3$ scintillation crystals, were aligned coincident with the sample stack. Spectra were collected, using a system based on an Ortec Positron Lifetime Picosecond Timing System (Oak Ridge, TN ), over 1 hour at each temperature collecting greater than $10^6$ incidences. Incidences were compiled using a multichannel analyzer to generate PALS spectra. Temperature was controlled using a Lakeshore 331 temperature controller (LakeShore Cryotronics, Westerville, OH). PALS spectra were collected from -30 °C to 125 °C in increments of 5 °C. Spectra were analyzed using PATFIT-88[14] software to determine long lived ortho positronium lifetimes and intensities.

## Results and Discussion

### *Solid State Structure*

The thermograms for liquid crystalline, LC-PFDA, and amorphous, A-PFOA, polymers are shown in Figure 58. A well-defined glass transition can be noticed for amorphous A-PFOA network at about -2.7 °C. The corresponding inset of Figure 58 displays how Tg was determined. In the first heating scan of LC-PFDA films, a very well defined liquid crystalline endotherm appears at 71 °C along with a second overlapping peak at about 54 °C. The low temperature peak was not observed in the second heat. Similar double melting phenomena have been indicated in several materials including poly(trimethylene terephthalate),[15] PEEK,[16] and PET,[17] and the double peak has been attributed to different lamellar structures and thicknesses, and secondary crystallization. It is speculated here that the low temperature peak is a result of formation of less perfect LC fraction, perhaps a transient LC form, which is kinetically trapped during UV-curing. Residing in the isotropic melt above the transition temperature allows molecular motion, giving rise to a more complete and uniform LC phase to be formed upon cooling. Secondary melting peaks have been shown to increase in magnitude upon annealing[17] prompting further study of the first endothermic peak at 54°C.

An annealing DSC heating experiment was performed where the sample was heated twice from -70°C to 200°C and then quenched to 54°C and left at isothermal conditions for 120 minutes. After the anneal, the sample was quenched to -70°C and heated for the third time to 200 °C at 10 °C/min. The reappearance or shifting of the double peak would be expected if the phenomena that is responsible for this peak was reversible. The results of the three heating cycles are shown in Figure 59 where there is no evidence of the development of this second peak after annealing confirming that this peak is a result of a molded in, kinetically locked in ordered phase.

The temperature width of LC-isotropic transition thus has been estimated from the second scan, and it was found to be about 12°C. Interestingly the width of LC-isotropic phase transition is about the same as for the crystalline –isotropic transition in the case of side chain crystallizable comb-shaped polymers. LC-PFDA samples, sharing the same backbone acrylic structure as the A-PFOA films, did not show any evidence of the glass transition temperature near -2 °C. No measurable jump in the heat capacity at $T_g$ can be noticed on the corresponding first and second heat LC-PFDA thermograms. This result clearly implies that perhaps only a very small fraction of an amorphous phase is present in LC-PFDA sample below LC-isotropic transition. Practically the entire polymer, prior to transition, can be considered to be in the ordered LC state. Attempts were made to vary the amount of side chain order by quenching from the melt at different rates. Using DSC, cooling rates of 1, 5, 10 and 40 °C/min were used to cool from 200°C to -70°C. Endotherm integration between 25°C and 150°C were performed and did not show a difference beyond experimental scatter.

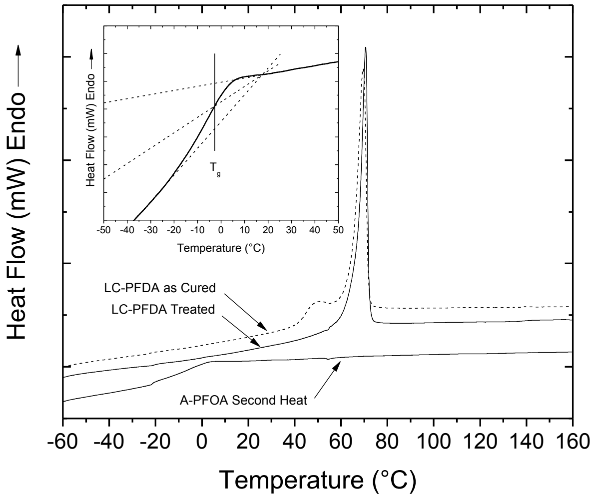

*Figure 58*. DSC thermograms of A-PFOA, LC-PFDA films. Each thermogram is shifted to show details. The inset plot illustrates the midpoint method used to determine the glass transition temperature of A-PFOA.

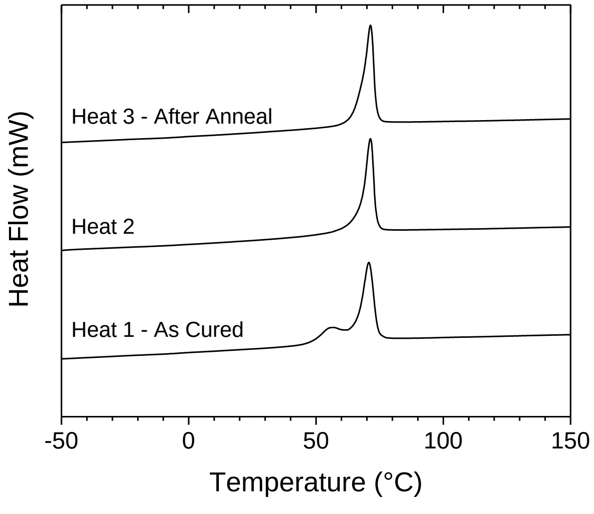

*Figure 59.* DSC annealing thermograms of as cured, 2$^{nd}$ heat, and annealed heating scans of LC-PFDA showing the disappearance of the 54 °C peak.

WAXD spectra of A-PFOA and LC-PFDA film samples were collected at room temperature and shown in Figure 60. As expected, A-PFOA films displayed a typical amorphous halo with a broad peak situated at 17 degrees 2θ. As cured and thermally treated (heated above LC-istropic transition and cooled) LC-PFDA samples exhibited fairly similar diffractograms. This implies that there is no any structural difference of the ordered LC phase in these two cases. Exceptionally well defined, sharp peaks were observed at 2.8, 5.5, 8.1, and 18 degrees 2θ. The diffractogram for LC-PFDA system was virtually identical to that reported by Volkov et. al[7] who used the same pefluorinated mesogen moieties in the case of his comb-shaped acrylic polymer. Based on Volkov's convincing structural analysis we agree here that there is the presence of smectic-B LC structure which is characterized by an additional hexagonal order of mesogens in the interlayers. Several related references devoted to this subject can be found elsewhere.[5,7,18] A schematic of this hexagonal, smectic structure is shown in Figure 61.

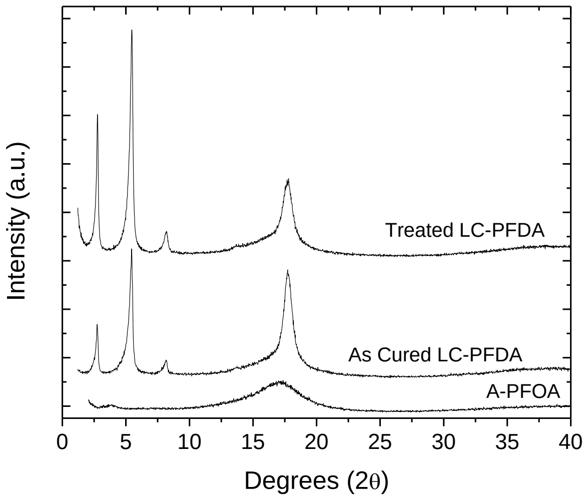

*Figure 60*. Wide angle X-Ray diffraction patterns for A-PFOA and LC-PFDA thin films. As cured and thermally treated samples are shifted vertically to show the details of each diffractogram.

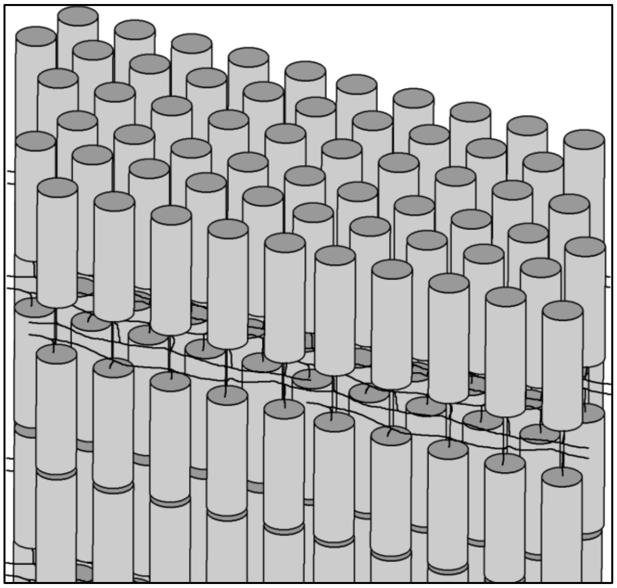

*Figure 61*. Schematic of hexagonal, smectic ordering of LC-PFDA where rigid cylinders represent the perfluorinated side chain mesogen.

*Transport and Free Volume Behavior*

Figure 62 illustrates typical downstream pressure versus time plots for LC-PFDA collected during CVVP tests at 23 °C and 80°C. Figure 63 shows $CO_2$ permeability versus temperature for A-PFOA and LC-PFDA films determined in the range 23-85$^{o}$C. The two films showed very different behavior. Gas permeability of A-PFOA displayed a gradual increase with temperature through the whole temperature range. In turn, gas permeability of LC-PFDA, in addition to expected gradual increase, exhibited a fairly sharp increase of permeability in the vicinity of LC-isotropic transition. The temperature width of this transition as measured via gas permeation experiment was about 8$^{\circ}$C which was in accord with DSC measurements described earlier. Carbon dioxide permeability was raised by a factor of two within the transition temperature range from about 200 to 400 Barrer. The changes of permeability at the point of thermotropic transition thus appeared to be smaller than in the case of side chain crystallizable comb-shaped polymers. This result implied that this smectic-B ordered phase was more permeable and soluble for small gas molecules than the side-chain crystalline phase. As expected, being amorphous, A-PFOA film exhibited gas permeability larger than LC-PFDA. At room temperature $CO_2$ permeability of A-PFOA was found to be about 300 Barrer while LC-PFDA film showed permeability about 100 Barrer. At 75 $^{o}$C, the end point of LCP-isotropic transition, A-PFOA showed $CO_2$ permeability about 600 Barrer and LC-PFDA about 400 Barrer. If the difference in gas permeability for these two systems was expected below LC-isotropic transition, a question can be posed asking why gas permeability for these two systems remained quite different above this point. We believe that the chemical difference between these two systems, the degree of fluorination, can also play the role. Studying this factor however was beyond the scope of this manuscript. As gas permeability is closely related to free volume, it was interesting to explore the free volume behavior.

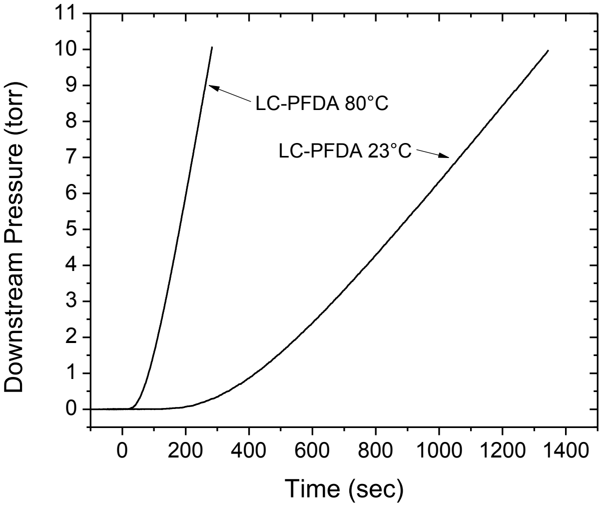

*Figure 62.* Representative curves illustrating the development of the steady state pressure increase in the downstream volume of the CVVP apparatus for a LC-PFDA film at 23 °C and 80 °C.

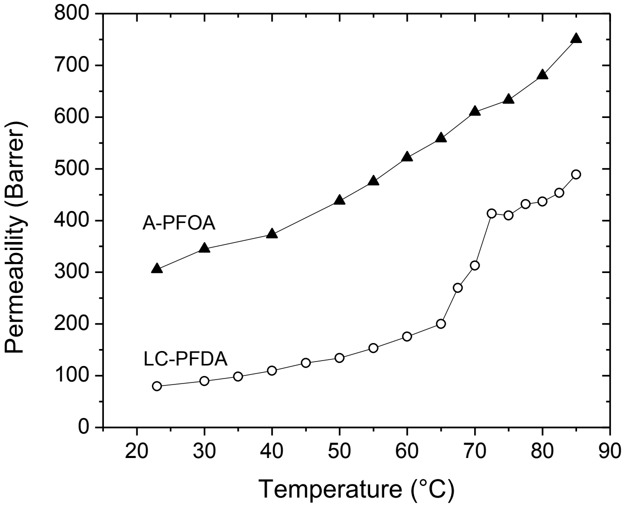

*Figure 63.* $CO_2$ Permeability of A-PFOA and LC-PFDA thin films as a function of temperature.

The average hole free volume, was determined using PALS from a minimum temperature of -35° C to a maximum of 125 °C in increments of 5 °C. Long lived o-Ps lifetimes were collected over one hour and fit using PATFIT-88. An empirical model has been used to correlate the third lifetime component, $\tau_3$, to the radius of free volume holes, R. The Tau-Eldrup equation, as shown in Equation 41, is commonly employed for spherical free volume elements:[19]

$$\text{Equation 41: } \tau_3 = \frac{1}{2}\left[1 - \frac{R}{R_o} + \frac{1}{2\pi}\sin\left(\frac{2\pi R}{R_o}\right)\right]^{-1}$$

where $R_o$ is an empirical constant from studies of porous solids.[20] The average volume of holes, $<V_h>$, can then be calculated using: $<V_h> = 4/3\ \pi R^3$ and is reported in the units of Å³.

A minimum of three spectra were collected for each material at each temperature. A representative spectrum is shown in Figure 64, along with the multiparameter fit, of LC-PFDA at 30°C. Average o-PS intensity and $<V_h>$ are seen in Figures 65 and 66, respectively with error bars indicating the standard deviation of the three spectra. $I_3$ represents the total fraction of positrons that form o-Ps and has been correlated with the concentration of free hole elements in some polymer systems.[13]

The A-PFOA sample exhibited a gradual increase of $<V_h>$ and o-Ps intensity, $I_{3,}$ as a function of temperature. In the case of LC-PFDA, both $<V_h>$ and $I_3$ exhibited a rapid increase at the point of thermotropic transition. $I_{3,}$ in A-PFOA and LC-PFDA systems, show identical values at temperatures below the LC-PFDA transition suggesting the concentrations of holes is similar in the two materials. At the transition, LC-PFDA is seen to increase in intensity indicating an increase in the concentration of free volume elements. The combination of an increased hole size, along with the increase in hole concentration causes the observed increase in small molecule diffusion at the thermotropic transition in LC-PFDA polymer films.

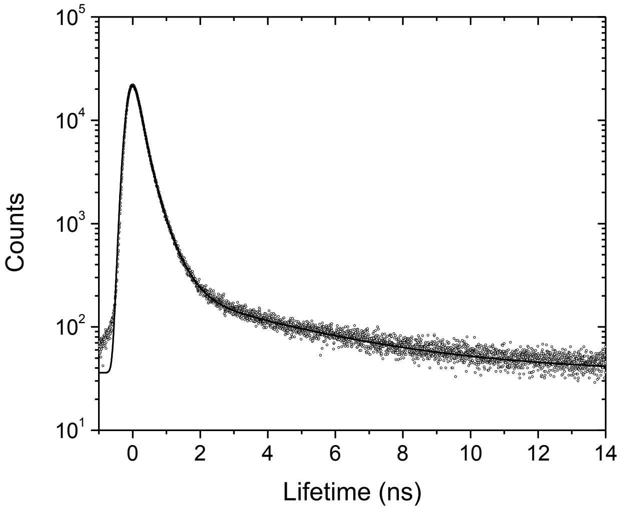

*Figure 64.* A representative PALS spectra and multicomponent fit of LC-PFDA at 30 °C.

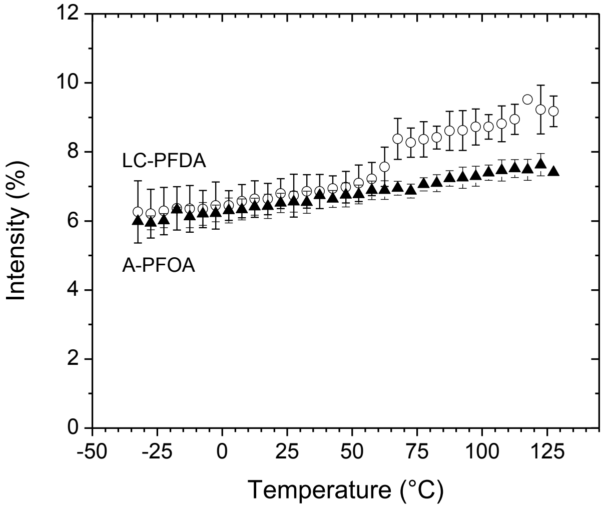

*Figure 65.* Long lived o-Ps relative intensity, $I_3$, for A-PFOA and LC-PFDA.

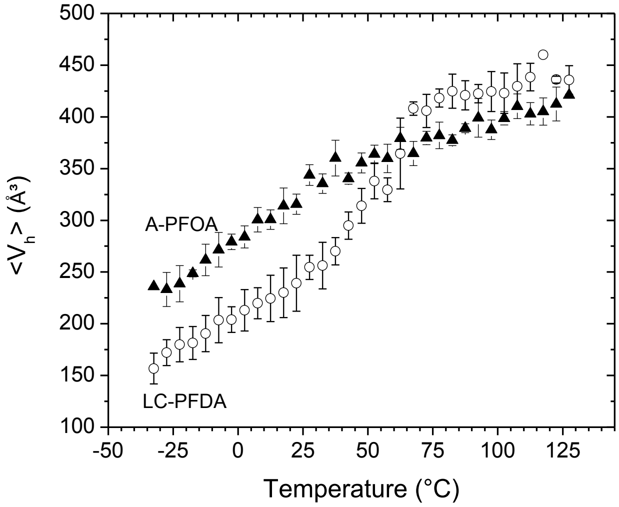

*Figure 66*. Average hole free volume $<V_h>$ calculated from $\tau_3$ for A-PFOA and LC-PFDA.

## Conclusions

The feasibility of developing a permeation switch through the UV curing of lightly cross linked mesogenic perfluorinated acrylates was shown and compared to a similar amorphous perfluorinated acrylate cross linked system. X-ray diffraction confirms the presence of well-defined smectic ordering in films prepared via UV-curing with 1 wt% cross linker. DSC thermograms of mesogen containing films displayed a distinct endothermic peak at 71°C indicating the transition from smectic ordering to an isotropic morphology. The absence of a detectable glass transition indicates a high degree of order in these liquid crystalline systems. An increase in $CO_2$ permeability at 71 °C is shown to be a result of an increase in the average size of free volume elements and an increase in the hole concentration upon heating through the smectic-isotropic transition.

# References

(1) Stewart, RF, Mohr, JM, Budd, EA, Phan, LX, Arul, J, In Polymeric Delivery Systems; American Chemical Society 520 (1) 232 (1993)

(2) Greene, L.; Phan Loc, X.; Schmitt Ed, E.; Mohr Judy, M. In Polymeric Delivery Systems; American Chemical Society: 1993; Vol. 520, p 244.

(3) Mogri, Z, Paul, DR, “Gas sorption and transport in side-chain crystalline and molten poly(octadecyl acrylate)” Polymer, 42 (6) 2531-2542 (2001)

(4) Mogri, Z, Paul, DR, “Gas sorption and transport in poly(alkyl (meth)acrylate)s. I. Permeation properties. Polymer, 42(18) 7765-7780 (2001)

(5) Honda, K., et al., “Molecular Aggregation Structure and Surface Properties of Poly(fluoroalkyl acrylate) Thin Films.” Macromolecules, 38(13) 5699-5705 (2005)

(6) Honda, K, Morita, M, Sakata, O, Sasaki, S, Takahara, A. “Effect of Surface Molecular Aggregation State and Surface Molecular Motion on Wetting Behavior of Water on Poly(fluoroalkyl methacrylate) Thin Films.” Macromolecules 43(1) 454-460 (2009

(7) Volkov, V.V., et al., “Aggregation state and mesophase structure of comb-shaped polymers with fluorocarbon side groups.” Polymer, 33(6) 1316-1320 (1992)

(8) Volkov, V.V., et al., “Effect of thermal molecular motion on pervaporation behavior of comb-shaped polymers with fluorocarbon side groups.” Polymer Bulletin, 32(2) 193-200 (1994)

(9) Kwisnek, L, Heinz, S, Wiggins, J. S, Nazarenko, S. “Multifunctional thiols as additives in UV-cured PEG-diacrylate membranes for CO2 separation.” Journal of Membrane Science, 369 (1–2) 429-436. (2011)

(10) Lin, H, Freeman, B. D., “Gas solubility, diffusivity and permeability in poly(ethylene oxide).” Journal of Membrane Science, 239(1) 105-117 (2004)

(11) Lin, H, Wagner, E. V, Swinnea, J. S, Freeman, B. D, Pas, S. J, Hill, A. J, Kalakkunnath, S, Kalika, D. S. “Transport and structural characteristics of crosslinked poly(ethylene oxide) rubbers.” Journal of Membrane Science,276(1–2) 145-161 (2006)

(12) Raharjo, R. D, Lin, H, Sanders, D. F, Freeman, B. D, Kalakkunnath, S, Kalika, D. S. “Relation between network structure and gas transport in crosslinked poly(propylene glycol diacrylate).” Journal of Membrane Science, 283(1–2) 253-265. (2006)

(13) Kobayashi, Y, Zheng, W, Meyer, E. F, McGervey, J. D, Jamieson, A. M, Simha, R. “Free volume and physical aging of poly(vinyl acetate) studied by positron annihilation.” Macromolecules, 22(5) 2302-2306. (1989)

(14) Kirkegaard, P, Eldrup, M, Mogensen, O. E, Pedersen, N. J. “Program system for analysing positron lifetime spectra and angular correlation curves.” Computer Physics Communications, 23(3) 307-335 (1981)

(15) Zeng, W.; Li, H.; Liu, T.; Yan, S. “A study on the double melting behavior of poly(trimethylene terephthalate)” Chin. Sci. Bull., *53*, 2145-2155 (2008).

(16) Lee, Y.; Porter, R. S.; Lin, J. S. “On the double-melting behavior of poly(ether ether ketone)” Macromolecules, *22*, 1756-1760 (1989)

(17) Roberts, R. C. “Poly(ethylene terephthalate) II—Morphological changes on annealing” Polymer, 10, 117-125 (1969)

(18) Katano, Y, Tomono, H, Nakajima, T. “Surface Property of Polymer Films with Fluoroalkyl Side Chains.” Macromolecules, 27(8) 2342-2344 (1994)

(19) Eldrup, M, Lightbody, D, Sherwood, J. N. “The temperature dependence of positron lifetimes in solid pivalic acid.” Chemical Physics, 63(1–2) 51-58 (1981)

(20) H. Nakanishi, S. J. W., Y.C. Jean Positron Annihilation Studies of Fluids; World Scientific, Singapore, 1988.

# CHAPTER VII

# UV-CURED PERFLUORINATED SIDE CHAIN LIQUID CRYSTALLINE NETWORKS FOR PERMEABILITY SWITCHING AND HE/$H_2$ GAS SEPARATION

## Abstract

The rigid rod structure of side chain acrylates of a given length gives rise to an ordered morphology that has a well-defined crystalline order and melting temperature. Melting of the ordered domains gives rise to “switching” behavior of light gas transport properties can be utilized as a molecular valve for certain applications. The well-defined order of $C_8F_{17}$ and $C_{10}F_{21}$ side chain acrylates was characterized and shown to develop a mesophase upon UV-curing that was irreversible unless rapidly quenched. The well-defined melting temperature of $C_8F_{17}$ (f10) at 72 °C was exploited in the study of gas transport properties that traversed this melting temperature showcasing the permeability switching. Permeability gains across the melting of the ordered morphology for several gases were shown to be due to solubility increases alone. Contrary to standard two-phase systems, where ordered phases increase tortuosity and decrease diffusivity in the semicrystalline systems, these systems show no detectable switch in diffusivity across the transition temperature. Analysis of both the free volume hole size and volume contributions are also reported. Furthermore, the side chain morphology lends itself to high He/$H_2$ separation performance.

## Introduction

Comb-shaped, mesogenic perfluorinated acrylate materials have been of great interest for the past few decades for their unique surface and transport properties.[1-3] Disruption of side chain order through a mesogenic-isotropic transition has been shown to increase the flux and decrease the selectivity of water/acetone and water/ethanol mixtures in pervaporation studies.[4] This permeation switching behavior, which occurs sharply at the isotropic transition, has been studied in long alkyl acrylate side chain polymers where sharp permeability jumps occur at the melting point of side chain crystalline morphology.[5,6]

The melting behavior of perfluorinated alkyl side chain acrylates has been briefly described in a previous publication.[7] Here we further study the effects of photopolymerization on the morphology of the films. We also investigate the light gas transport properties as a function of temperature and elucidate the thermal "switching" behavior as a function of the side chain ordered morphology and the free volume characteristics of the network. Specifically, we present light gas permeability, solubility, and diffusivity of a range of gases and expand free volume analysis beyond the materials studied in the previous work.[7]

## Experimental

### *Materials and Film Preparation*

Figure 67 shows all chemicals used in this work. Perfluoroinated acrylate monomers 2-perfluorohexyl ethyl acrylate (f8), 2-perfluorooctyl ethyl acrylate (f10), and 2-perfluorodecyl ethyl acrylate (f12), were acquired from Fluoryx, Inc (San Leandro, CA). Perfluorinated cross-linker, 1H,1H,6H,6Hperfluorohexyldiacrylate was acquired from Oakwood Product (West Columbia, SC). Photo initiator (PI), IRGACURE 2020, was acquired from CIBA Chemicals. All monomers were used as received. Industrial grade light gasses He, $H_2$, $O_2$, $N_2$, Ar, $CO_2$, and $CH_4$ were acquired from Airgas. $CF_4$ was acquired from Praxair.

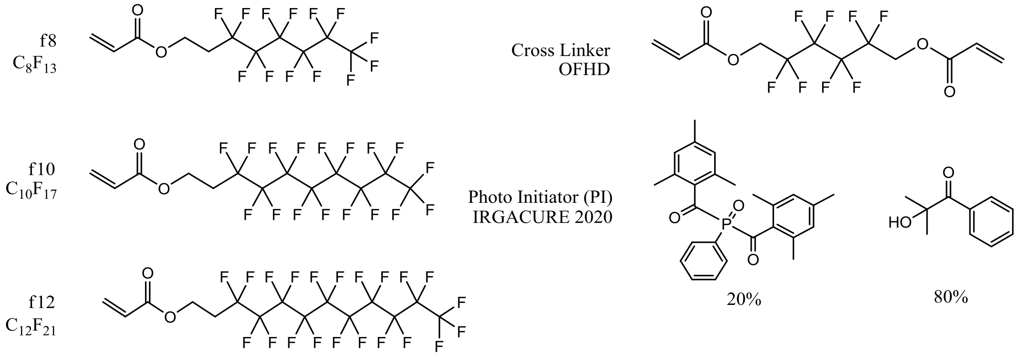

*Figure 67*. Chemical structures used in this work.

All films were prepared by mixing 98 wt% acrylate monomer, 1 wt% PI, and 1 wt% cross-linker and sonicating the miscible monomer mixtures for 15 minutes to ensure complete mixing. Monomer mixtures had a yellow tint from the photo initiator. Glass plates were cleaned with acetone and coated with Rain-X to aid the removal of the final film from the glass substrate. All monomer mixtures, except f12, were poured onto glass plates and sandwiched with a second glass plate using shims to ensure consistent thickness. Each glass sandwich was passed ten times under a Fusion UV Systems EPIQ 6000 high intensity UV line where the total UV exposure time was 29 seconds with an irradiance of 82 $mW/cm^2$ at a belt speed of 0.23 m/s. Films were removed from the glass plates and the outer edges of the film was removed as unreacted monomer was present near the exposed areas of the film, most likely due to oxygen inhibition. The bulk films did not show any evidence of uncured monomers.

F12 monomer is a crystalline solid at ambient conditions. To process f12 monomer, a heat gun was used to heat the monomer above 55 °C during mixing and film preparation. Glass plates were prepared as described earlier and were heated using two IR lamps. The glass temperature was monitored using a thermocouple. Heated f12 monomer mixtures were poured onto the heated (>55°C) glass plates, sandwiched with a second glass plate and irradiated using a medium pressure mercury UV lamp at an intensity of 16 $mW/cm^2$ for five minutes. The glass and film sandwich was allowed to slowly return to ambient conditions before the film was removed.

*Characterization*

Crystalline structure was characterized with wide angle X-Ray diffraction using a Rigaku Ultima III diffractometer (Cu Kα radiation, $\lambda = 1.542$Å) programmed with a step size of 0.2 degrees 2θ at a scan rate of 0.25 steps/min, and a diffractogram range of 2 to 40 degrees 2θ. Thermal transitions were determined via differential scanning calorimetry using a TA DSC Q2000. Heating scans were recorded on 8-10 mg samples heated from ambient conditions to 150 °C at 10 °C/min, cooled to -70 °C at 5 °C/min and heated again to 150 °C at 10 °C/min. When detectable, glass transition temperatures were determined at the intersection the heat capacity and the average slope calculated from linear fits of specific heat capacities below $T_g$ and above $T_g$.[8]

Light gas flux was measured using a custom diffusion lag, constant volume variable pressure setup as described earlier by our group[9] which is based on prior reports of this setup.[10-12] The upstream volume was pressurized to 3.5 atma for all gasses. Tests were initiated by opening a valve between the upstream volume and the film causing a slight drop in the recorded upstream pressure. This slight drop in pressure marked the start of the test and the zero time of the test. Pressure increase from vacuum in the downstream volume was measured with a MKS 226A Baratron differential capacitance manometer with the reference port connected to a vacuum. Data was collected with time resolutions of 0.25 seconds and 1.0 second for fast and slow gases, respectively, until there was an observed steady state pressure increase with time. Cell temperature was controlled with a water/ethylene glycol mixture pumped through the cell and measured with a thermocouple located near the sample film. Films were equilibrated at a prescribed temperature while being evacuated for greater than 12 hours prior to testing.

Hole free volume properties were studied via positron annihilation lifetime spectroscopy (PALS) using a fast-fast coincidence system based on a system described by Jamieson et. al [13] with an average resolution FWHM of 500 ps. Thin film samples were stacked to achieve a total thickness greater than 1 mm and contained in aluminum foil packets. An aluminum foil wrapped Na22 source was sandwiched between two sample packets. The sandwiched assembly was placed in a custom thermal vacuum chamber and photomultiplier assemblies (Hamamatsu H3378-50), equipped with $BF_3$ scintillation crystals, were aligned coincident to the sample stack. Spectra were collected using a system based on an Ortec Positron Lifetime System (Advanced Measurement Technology Oak Ridge, TN) over one hour to collect greater than $10^6$ incidences. Incident lifetimes were compiled using a multichannel analyzer with 2047 channels with resolution of 0.0292 ns/channel. Sample chamber temperature was controlled using a Lakeshore 335 temperature controller. Samples were allowed to equilibrate at the prescribed temperature for 15 minutes prior to collecting each spectrum. PALS spectra were collected from 0 °C to 190 °C in increments of 5 °C. Spectra were analyzed using PATFIT-88 software with fits of the resolution Gaussian followed by a positron fit of three components. Specifically, $\tau_3$ and $I_3$, the lifetime and intensity of the long lived ortho-Positronium, respectively, are reported.

Density was measured using an immersion displacement method using a Mettler Toledo XS104 analytical balance equipped with a density determination kit with water as the immersion fluid. Specific volume as a function of temperature and pressure was determined using a Gnomix dilatometer (Gnomix, Boulder, CO) which is described by Zoller.[14] Samples between 1.0 and 2.0 g were loaded into the rigid cell and evacuated for five minutes under vacuum. The remaining cell volume was filled with mercury. The internal flexible bellow was connected to the LVDT and the cell was secured within the pressure vessel. Standard isothermal (ITS) runs were performed from 30 °C to 200 °C in increments of 5 °C with a pressure range of 10 MPa to 150 MPa. Tait equation extrapolations to 0.1 MPa were performed within the Gnomix v8.06 software.

## Results and Discussion

The structural, thermal, transport, and free volume properties of side chain (SC) polymers are presented to compare the SC order to the amorphous state in the described polymer systems. F8 is accepted as a reasonable amorphous analog to the f10 and f12 SC ordered polymers. The authors acknowledge the chemical differences between the SC ordered polymers and the assumed amorphous analog as the addition of tetrafluoroethylene units on the side chain and aim to mention possible differences in properties that were expected throughout the results section. These results expand on the knowledge base of transport phenomena in side chain polymer systems presented by Paul.[5,6,15,16]

*Investigation into Annealing and the Cured-in Mesophase*

DSC thermograms were collected from the second heat of f8, f10, f12, films and are shown in Figure 68. F8 shows a glass transition at -3 °C indicating that f8 is in the rubbery state at room temperature. F10, and f12 show well defined endotherms at 72 °C, and 116 °C, respectively.

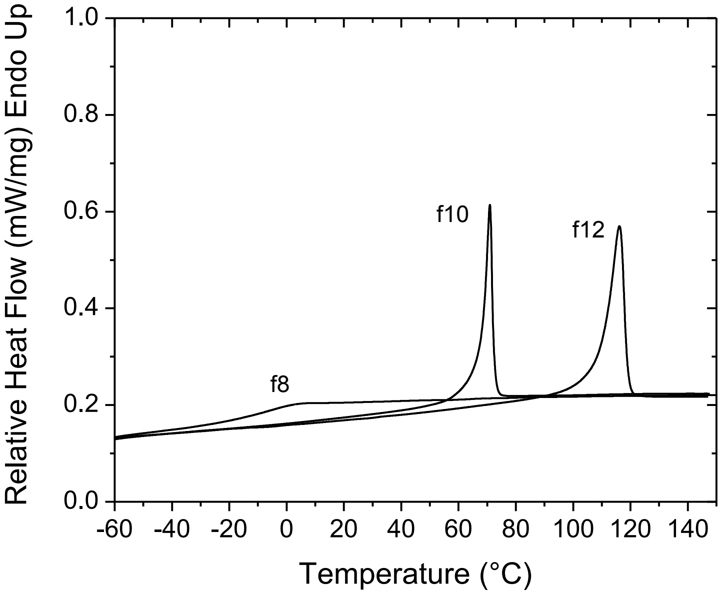

*Figure 68.* DSC thermograms for f8, f10, f12.

Analysis of first heat scans revealed a second peak at 50 °C for f10 and a shoulder at 56 °C for f12 samples. The peak found in f10 was discussed in the previous work[7] and similar behavior was found for f12. Rapid cure kinetics of photopolymerization kinetically traps a transient liquid crystalline mesophase morphology that is allowed to form a more uniform crystalline structure upon annealing. In an attempt to realize the nature of the photopolymerization quenching, further study toward understanding the secondary peak was performed by first annealing an f10 film at 80°C for 15 minutes and cooled to room temperature. Films were heated above the isotropic transition temperature and rapidly quenched by immersing the sample in liquid nitrogen. Figure 69 shows the DSC thermograms from an As-Cured sample, a 2$^{nd}$ heat annealed sample, and a heated and LN$_2$ quenched sample. The secondary peak present in both the LN$_2$ quenched and as cured samples suggests an imperfect morphology developed as a result of rapid quenching of the side chain mesogens, from rapid photopolymerization or rapid thermal quenching freezing of the mesophase.

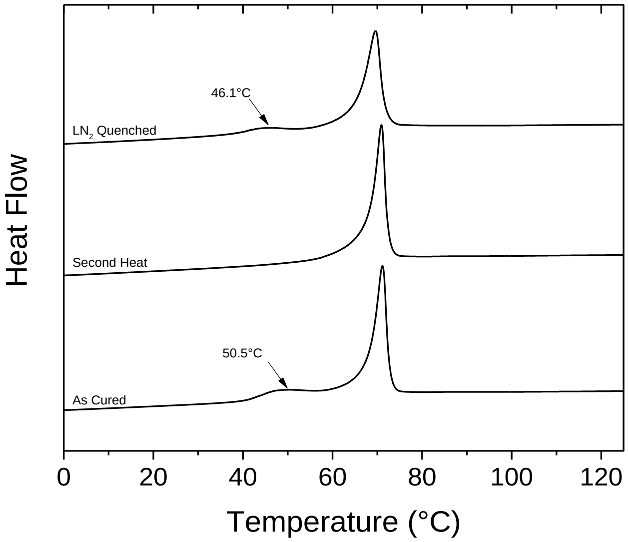

*Figure 69.* Thermograms of f10 as cured, after a second heat and after quenching with liquid nitrogen.

The development of a crystalline structure in semicrystalline polymers is very sensitive to cooling rates. The effect of cooling rate is commonly observed via DSC where the change in the crystalline melting peak can be used to quantify the change in crystalline content. Here we used DSC to examine the quench rate dependence of the melting endotherm. First scans were cooled to -70 °C and heated at 10 °C/min to show the secondary peak. Heating endotherms were collected after subsequent scans quenching from the melt at 1, 5, 10 and 40 °C/min.  Figure 70 displays the thermograms for f10 and f12 at the described cooling rates. A decrease in total enthalpy of the two peaks was shown after annealing from the UV cured mesophase for both f10 and f12. There was not a significant change in the melting peak area as a function of cooling rate after the initial heating up to the instrument limit of 40 °C/min. Cooling at 40 °C/min seems to allow sufficient mobility of the side chain in the melt to arrange into the well-defined order, eliminating the transient mesophase. This data showed that it was necessary to anneal the sample after UV curing and allow the sample to return to ambient conditions slowly but the annealing rate, within reason, did not impact the amount of ordered phase.

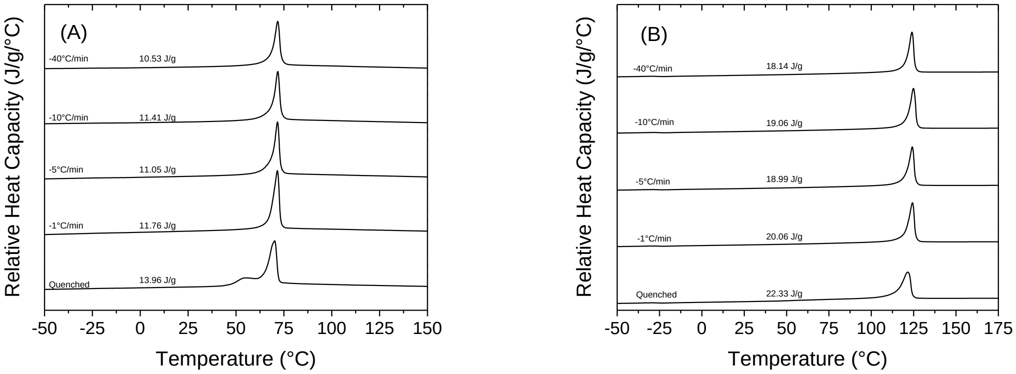

*Figure 70*. DSC quench rate results of f10 (A) and f12 (B) melting peaks as cured and at quenching rates of 1°, 5°, 10°, 40 °C/min.

Secondary peaks can also be the result of aging. Aging can be explored by holding the sample at the temperature corresponding to the secondary peak and quenching after holding. If aging occurs, the peak would reappear after the hold temperature. This did not occur and was shown in our previous paper.[17]

Wide angle X-Ray diffraction was used to determine the changes in morphology resulting from the annealing and quenching processes. The changes were briefly discussed previously.[7] Well-defined peaks with dimensions representative of the side chain dimensions of the respective polymers suggest smectic B ordering as described by Volkov.[3] Reflection angle did not show a change as a result of quenching but peak intensity did change after annealing. Furthermore, there was no evidence of a secondary structure from any cured in mesophase. Figure 71 shows the As Cured and $LN_2$ quenched samples showing lower peak intensities for the hexagonal packing peak at 18 degrees $2\theta$ suggesting a relatively larger population of hexagonal packing after annealing. Similarly, the side chain order peaks below 10° show an increase in relative intensity. The peak locations of annealed f10 and f12 diffractograms correlate very well with literature reported diffractograms.[1,3] This evidence suggests that the cured-in mesophase is not an ordered structure. Rather, the secondary peak from DSC is evidence of a reordering from an unordered, quenched in transient LC form.

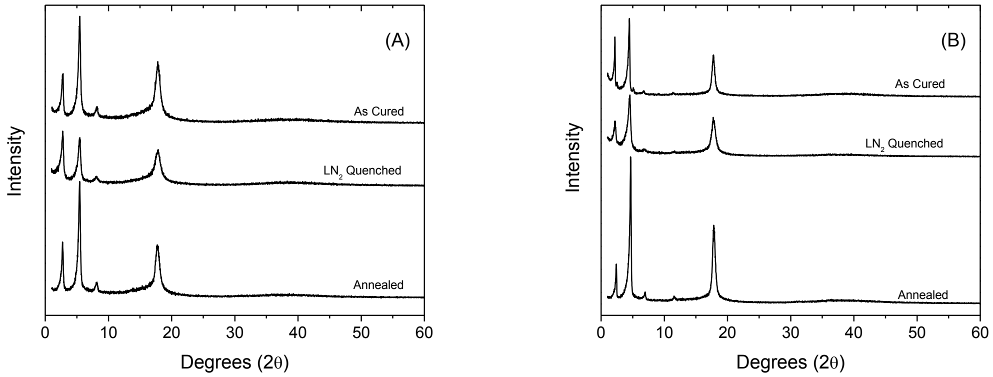

*Figure 71.* WAXD diffractograms of f10 (A) and f12 (B) thin films as cured, annealed and after annealing and $LN_2$ quenching.

Several attempts were made to determine the quantity of the ordered phase. Currently, a heat of fusion has not been reported making the determination of percent crystallinity from DSC data nearly impossible. Ordered content using X-ray data was not considered as a truly amorphous analog was not achievable.

Specific volume data was collected in attempt to determine crystalline content for f10 and f12. Figure 72 shows specific volume temperature data for f8, f10, and f12. The estimated amorphous density was determined using Simha-Somcymsky equations of state (SS-EOS) extrapolations from the melt state to ambient conditions. The PVT behavior of many amorphous fluorinated linear polymers[18,19] has been described by a simplified equation of state by Utracki and Simha[20] in the equilibrium melt state using

Equation 42: $$V(P,T) = V^* * exp\left(a_0 + a_1(\tilde{T})^{\frac{3}{2}} + (\tilde{P})\left[a_2 + \left(a_3 + a_4(\tilde{P}) + a_5(\tilde{P})^2\right) * (\tilde{T})^2\right]\right)$$

Equation 43 $$\tilde{T} = \frac{T}{T^*} \qquad \tilde{P} = \frac{P}{P^*} \qquad \tilde{V} = \frac{V}{V^*}$$

where $\tilde{P}$, $\tilde{T}$, and $\tilde{V}$ are reduced parameters and $P^*$, $T^*$, and $V^*$ are fit parameters.[18] Constants $a_0$ through $a_5$ are described by Utracki and Simha as:

$a_0$= -0.10346, $a_1$= 23.854, $a_2$= -0.1320, $a_3$= -33.7, $a_4$= 1032.5, $a_5$= -1329.9.[20] The conventional method to fit $V_{sp}$ data from PVT experiments at ambient conditions is to consider $P$ = 0 MPa and therefore $\tilde{P}$ = 0 reducing SS-EOS to:[20,21,22]

$$\text{Equation 44: } V(P,T) = V^* * exp\left(a_0 + a_1\left(\frac{T}{T^*}\right)^{\frac{3}{2}}\right)$$

Figure 72 shows the temperature dependence of specific volume for f8, f10, and f12. All fits showed sufficient agreement with the model with $R^2$ being greater than 0.99. Volume crystallinity is defined by $x_v = \frac{(\rho-\rho_a)}{(\rho_c-\rho_a)}$ and mass crystallinity is defined as $x_c = \frac{\rho_c}{\rho}x_v$ where ρ is the density, $\rho_a$ is the density of the amorphous fraction.[23] The amorphous fraction can be determined from PVT data and SS-EOS extrapolations from the melt state. The density of the ordered phase, $\rho_c$, was estimated from a and c dimensions of the hexagonal unit cell given by WAXD estimated to be 2.046 g/cc. Results are shown in Table 6.

Table 6

*Percent crystallinity estimated using specific gravity.*

| **f =** | **ρ (g/cc)** | **$\rho_a$ (g/cc)** | **$x_c$** |
|---|---|---|---|
| 10 | 1.798 | 1.734 | 0.233 |
| 12 | 1.852 | 1.773 | 0.319 |

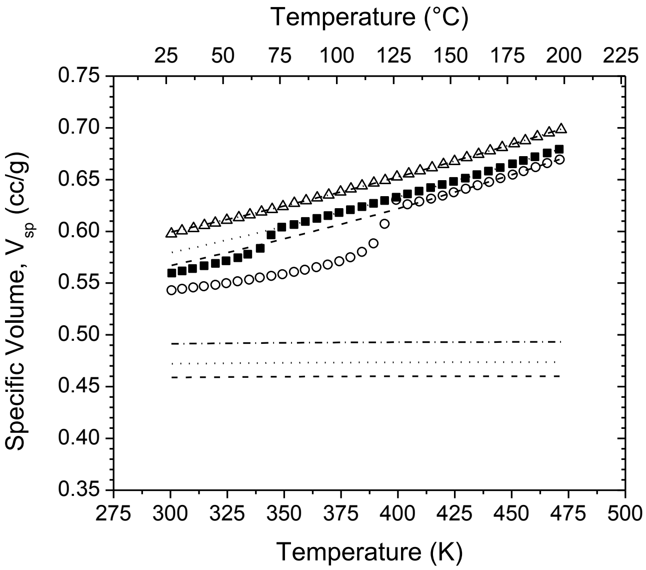

*Figure 72*. Specific volume, SS-EOS fits, and calculated $V_{occ}$ for f8 (△,-··-), f10 (■,·····), and f12 (○,‒ ‒).

Specific volume behavior for f8 displayed typical amorphous behavior. F10, and f12 displayed a typical second order transition at their respective melting temperature. A single step change at the melting temperature was observed for f10 and f12. Specific volume differences in the melt state across these studied systems were a result of the increase in fluorine from f8 to f10 and f12.

*Transport Phenomena*

Transport parameters were calculated from time lag diffusion pressure increase versus time data collected according to conventional diffusion lag techniques.[24] Permeability (P) was determined from the results of a linear regression of the steady state pressure increase versus time, $(dp_1/dt)_{SS}$, and calculated using,

$$\text{Equation 45} \quad P_A = \frac{V_d l}{p_2 ART}\left[\left(\frac{dp_1}{dt}\right)_{ss} - \left(\frac{dp_1}{dt}\right)_{leak}\right]$$

where $V_d$ is the downstream volume, $l$ is the film thickness, $p_2$ is the upstream pressure, A is the exposed area of the film, $R$ is the universal gas constant, $T$ is the absolute temperature of the downstream volume, and $(dp_1/dt)_{leak}$ is the leak slope determined prior to exposing the test gas to the film.[10] For all tests, $(d_{p1}/d_{t})_{leak}$ was less than 0.005 torr/minute and considered negligible. The steady state pressure increase regression was extrapolated to zero pressure using Origin 8.6 software. The x-intercept was defined as the time lag, $\theta$. The time lag was used to calculate the diffusivity, $D$ utilizing Equation 46.[25] Using permeability and diffusivity, solubility was calculated using $S = P / D$.

Equation 46 $$D = \frac{l^2}{6\theta}$$

Raw diffusion lag, pressure increase versus time, curves were collected at 23°C. Figure 73 shows diffusion lag curves of He, $H_2$, $CO_2$ $CH_4$ and $CF_4$ tests for f8 and f10 films. F12 films, even when cast on supports, were too brittle to test within practical limits. From these plots, the resolution was high enough to readily extract time lag and steady state slopes for P, D and S determination. The dotted lines show the extrapolation of the steady state to zero pressure. It is readily apparent from the diffusion lag plots that there is a size dependence on permeability for f8 and f10.

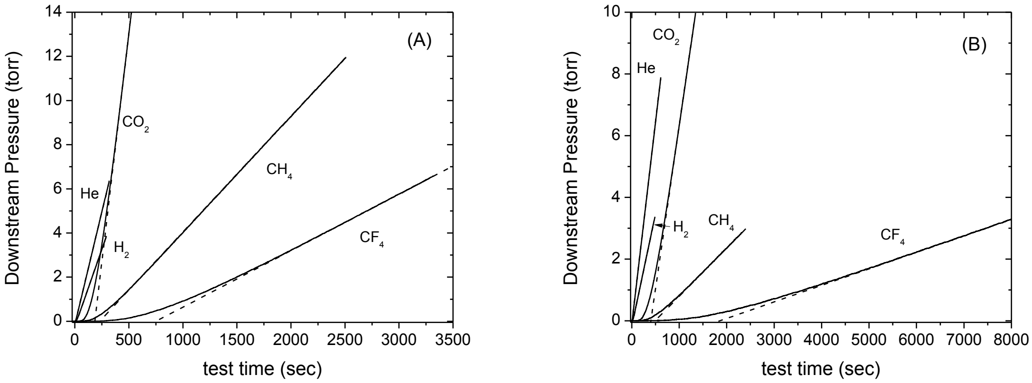

*Figure 73*. Raw diffusion lag downstream pressure increase data curves for f8 (A) and f10 (B) at 23 °C for He, $H_2$, $CO_2$, $CH_4$, and $CF_4$. Dotted lines represent regression fits from the steady state.

The penetrant size dependence of permeability and diffusivity is shown in Figure 74 with *P* and *D* plotted as a function of Lennard Jones collision diameter for He, $H_2$, $O_2$, N2, $CH_4$, $CO_2$, and $CF_4$ tests at 23 °C for f8 and f10. *P* and *D* for $CO_2$ and $N_2$ are also plotted with their kinetic diameters. All other gases show minimal differences between L-J diameter and kinetic diameter. Solubility is plotted against the gas critical temperature in Figure 74c. L-J diameter, kinetic diameter, and critical temperature for all gases can be found in Table 7. As expected, diffusivity data showed a strong dependence with penetrant size. The diffusivity differences between f8 and f10 are minimal compared to the differences shown in the solubility data. The solubility of the amorphous f8 polymer was nearly twice that of f10. This greater solubility in f8 can be attributed to both the morphological differences at 23°C and the lower fluorine content compared to f10.

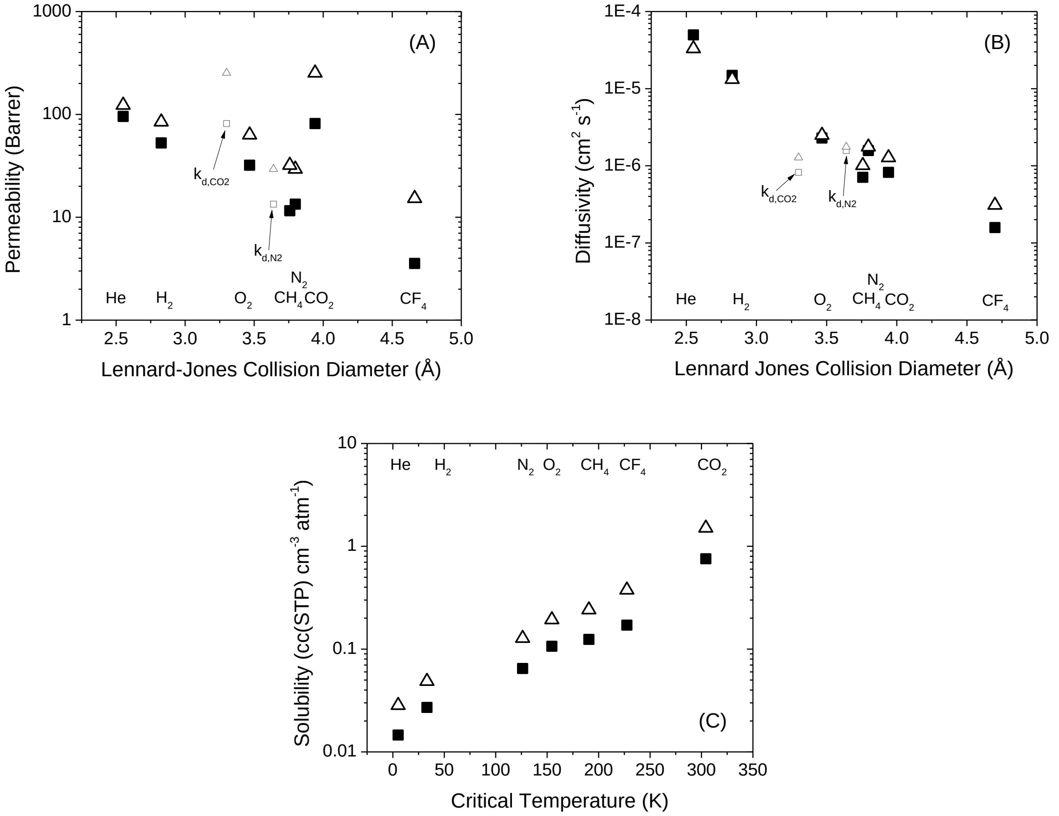

*Figure 74.* Light gas permeability (A), and diffusivity (B) as a function of Lennard Jones collision diameter and solubility (C) as a function of critical temperature for f8 (△) and f10 (■) at 23 °C. Kinetic diameters for $CO_2$ and $N_2$ are shown for comparison.

Table 7

*Kinetic diameters and critical temperatures of the studied penetrant gases.*

| Gas | Critical Temperature $T_C$ (K) | Kinetic Diameter $d_K$[26] (Å) | Lennard-Jones diameter $d_{LJ}$[27] (Å) |
|---|---|---|---|
| He | 5.2 | 2.6 | 2.551 |
| $H_2$ | 33.2 | 2.89 | 2.827 |
| $O_2$ | 154.6 | 3.46 | 3.467 |
| $N_2$ | 126.2 | 3.64 | 3.798 |
| $O_2$ | 304.2 | 3.3 | 3.941 |
| $CH_4$ | 190.6 | 3.8 | 3.758 |
| $CF_4$ | 227.65 | 4.7 | 4.662 |

To determine the effect of the side chain morphology on the transport properties in f10 films, a pseudo amorphous analog, f8, was used as a reference for the calculation of relative transport properties. Relative permeability, diffusivity, and solubility were calculated using $P_{10}/P_8$, $D_{10}/D_8$, and $S_{10}/S_8$, respectively. The compositional difference between f8 and f10 must be accounted for. Using relative transport coefficients, the effect of the additional $C_2F_4$ unit can be determined and can provide an estimate of the change in permeability from the chemical change alone. The relative P, D, and S are shown in Figure 75 versus penetrant kinetic diameter at 23 °C and 80 °C.

In the crystalline phase, at 23 °C, f10 is size selective as the relative permeability decreases with penetrant size. One outlier to this observation is $CO_2$ which shows lower relative permeability than the trend would suggest. If the data were reconsidered plotted against Lennard-Jones parameter $CO_2$ would lie in agreement with the other penetrant data suggesting that $CO_2$ behaves as a sphere rather than a rod in this system. At 23°C, He and $H_2$ show relative diffusivity greater than unity where the larger gases, $N_2$, $O_2$, $CH_4$ and $CO_2$ show diffusivity approaching unity. Diffusivity greater than unity would suggest that the ordered phase may actually promote diffusion, of these small gases, rather than hinder transport. Channeling has been proposed in syndiotactic polystyrene systems where channels increase the diffusion jump length through the crystalline domains, increasing the apparent diffusivity.[28] Here it was not apparent that relative diffusivity greater than unity is explained by channeling, rather, this can be considered directed diffusion where multiple unidirectional jumps can occur within the ordered phase, decreasing the mean diffusion path length. While jump lengths may be equidistant, the number of jumps in one direction is increased, causing higher diffusion rates for He and $H_2$ in the ordered phase compared to the amorphous analog, f8.

At 80 °C, 8 °C above the isotropic transition temperature, the relative permeability of all six gases is near 0.75. The merging of relative permeability at 0.75 is intriguing as $P_{10}/P_8$ for He and $H_2$ gas does not change. This confirms the ability for He to diffuse freely through the side chain morphology where the diffusion of other gases may be impacted by tortuosity. At elevated temperatures, above $T_m$, the size dependence of relative permeability and diffusivity was eliminated as the side chain morphology was disrupted.

The discrepancy from unity at 80°C can be explained as a combination of decreased solubility and diffusivity of f10 films compared to f8 as a result of the increased fluorine content in f10 relative to f8. Above the isotropic transition, relative diffusivity approaches unity and does not show a dependence with kinetic diameter suggesting free hole volume has reached a critical size where penetrant size effect is eliminated. Relative solubility at 23 °C for all gases is near 0.50 but increases to values greater than 0.75 at 80 °C as a result of an increase in sorption sites through the transition and melting of the side chain crystals.

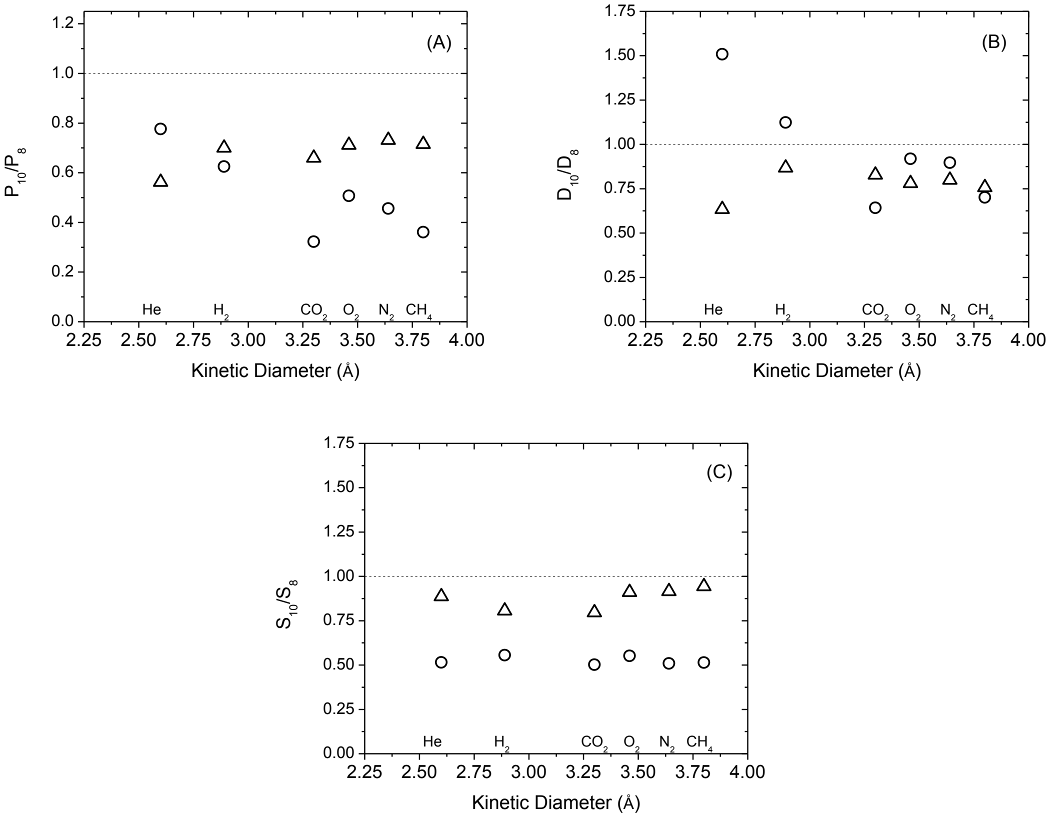

*Figure 75.* Relative transport coefficients, f10/f8, Permeability (A), Diffusivity (B), and Solubility (C) with respect to kinetic diameter at 23°C (○) and 80°C (△).

Rather than using f8 as an amorphous analog, a better approximation of the effect of the ordered domain can be achieved by an Arrhenius fit of melt state data and an extrapolation to temperatures where the ordered phase was present. Models of the temperature dependence of P, D, and S follow van’t Hoff - Arrhenius behavior predicted by[29]

Equation 47 $P = P_0 e^{-\frac{E_P}{RT}}$

Equation 48 $D = D_0 e^{-\frac{E_D}{RT}}$

Equation 49 $S = S_0 e^{-\frac{\Delta H_S}{RT}}$

where $P_0$, $D_0$, and $S_0$ are the pre-exponential factors, $E_P$ is the apparent activation energy of permeation, $E_D$ is the activation energy of diffusion, and $\Delta H_S$ is the enthalpy of sorption.

The effect of the ordered domain on transport properties was probed using four gases: He, $H_2$, $CO_2$, and $O_2$. The temperature dependence of P, D, and S was determined in order to compare the extrapolated melt state to the side chain ordered state. Time lag diffusion curves are shown in Figure 76 for a range of temperatures from 23°C to 95°C. From the diffusion curves, P, D, and S were determined and plotted in Figures 78, 79, and 80, respectively. P,D, and S are values are also tabulated in Table 8. van't Hoff fitting parameters are reported for He, $H_2$, $CO_2$, and $O_2$ in Table 9.

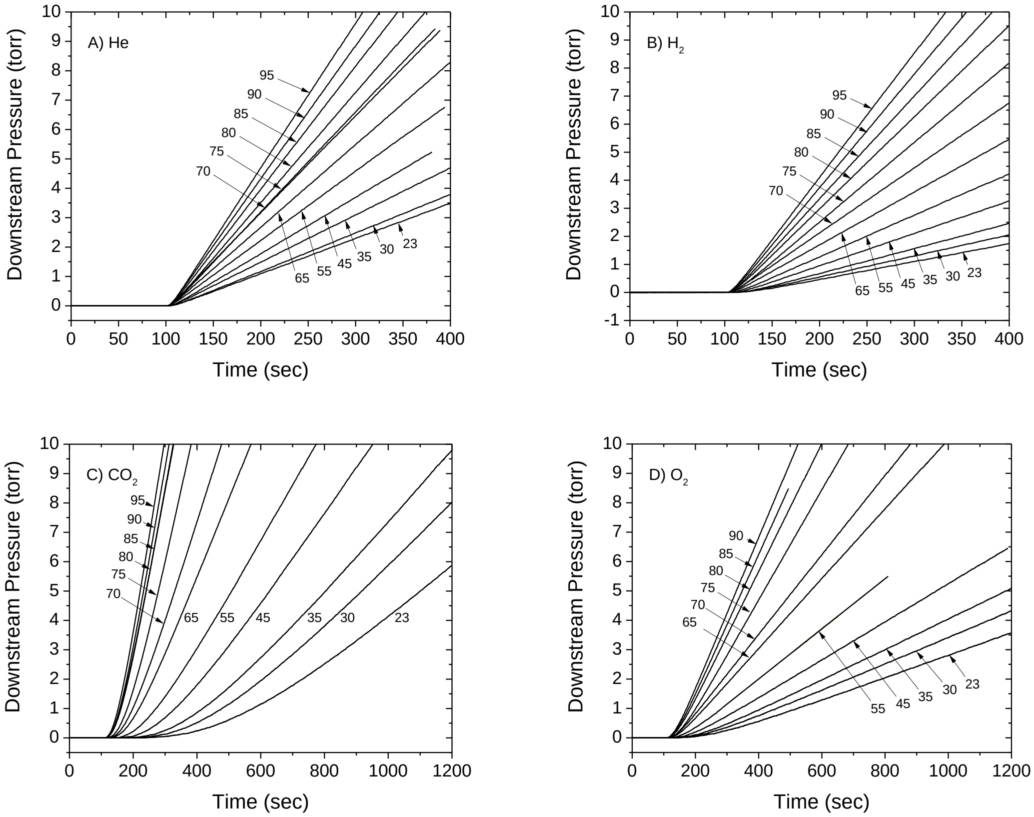

*Figure 76*.– Raw diffusion lag downstream pressure of f8 and f10 for He (A), $H_2$ (B), $CO_2$ (C), and $O_2$ (D) at increasing temperatures from 23 °C to 95 °C. All tests began at 100 seconds.

Permeability results in Figure 77 show large increases in permeability through the isotropic transition temperature for $O_2$, and $CO_2$ and a small step or a change in the slope of the permeability versus temperature plot for $H_2$. Helium data showed an increase of permeability with temperature with no evidence of a step change at the isotropic transition. This supports previous claims of the size dependence of the permeability jump on the penetrant.[6] Compared to linear alkyl side chain polymers which show a full order of magnitude jump in He and $H_2$ permeability at the side chain transition temperature, He does not show a jump in permeability for this f10 system and $H_2$ shows a minimal change in permeability.

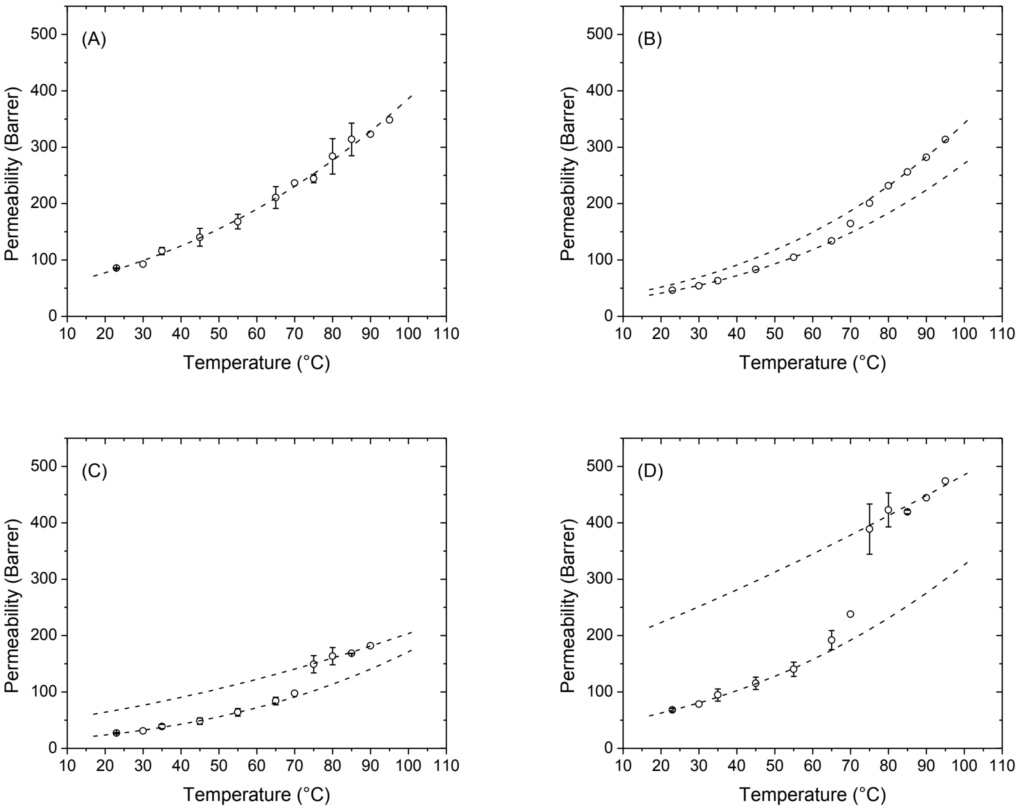

*Figure 77*. He (A), $H_2$ (B), $O_2$ (C), and $CO_2$ (D) permeability for f10 as a function of temperature. Dotted lines indicate the van’t Hoff fits of each data set above and below $T_m$ where applicable.

Diffusion of small gases through a polymer membrane is controlled by both the size of the penetrant[5] and the size of free volume elements in the matrix.[30] The step change through the melt transition was shown by Mogri to be dependent on the penetrant gas size in aliphatic side chain polymers and is suggested to play a larger role in the permeation jump. [5,15] Here, we do not show a major contribution to the step change from the diffusivity. The diffusion coefficient for He, $H_2$, $CO_2$, and $O_2$ are shown in Figure 78 as a function of temperature. Since there was not a significant jump in the diffusion coefficient, there must not be a tortuosity or chain immobilization effect caused by the side chain crystallinity.

In order to understand the effect or absence of tortuosity in the system, the diffusion jump at $T_m$ ($D^+/D^-$) can be used to determine the product of the chain immobilization constant, β, and the tortuosity or geometric impedance factor, τ as described by Michaels and Parker.[31]

$$\text{Equation 50} \quad D^- = \frac{D^+}{\tau\beta}$$

where $D^-$ and $D^+$ are the diffusivity at $T_m$ in the melt and crystalline state determined from van't hoff extrapolations to 72 °C, respectively. Jump size, $D^+/D^-$ values are tabulated in Table 8. $\tau\beta$ was near unity for $CO_2$ and $H_2$ and less than unity for $O_2$. Since this term is near unity, there is no strong evidence saying there is a tortuosity effect in these systems. $O_2$ diffusion may actually be promoted by the side chain crystallinity, giving rise to $\tau\beta$ being less than unity.

Further comparison of the side chain morphology in the semicrystalline state shows a dramatic size difference between aliphatic and perfluorinated side chain morphologies. The characteristic side chain hexagonal packing distance observed in X-ray diffractograms, has been reported as 4.2 Å and 5.0 Å for aliphatic and perfluorinated side chains, respectively.[3,32] The characteristic differences in hexagonal packing may be large enough to allow the free diffusion of gases through the ordered phase, ie no tortuosity, but not allow for the sorption of gases into this regime. The lack of diffusivity jumps for these perfluorinated systems contrasts the diffusivity jump in 22 carbon aliphatic chain systems which show a change in diffusivity across the melting point of side chain crystals for all of the gases studied.[15] This evidence suggests that the chemical nature of the perfluorinated ordered phase must allow for diffusion of gases through the morphology.

The lack of a diffusivity switch may also be due to the weaker inter-chain interactions between perfluoroalkyl side chains compared to linear alkyl side chains. Considering DSC data, the melting endotherm for linear aliphatic side chains is much greater than the perfluoroalkyl side chains. Aliphatic side chains show endotherms of 36 to 115 J/g[32] and f10 perfluoroalkyl side chain crystals give endotherms of 20.35 J $g^{-1}$.[3] This increased energy requirement to traverse the melting transition suggests a higher entropic gain in alkyl side chain systems, leading to greater diffusion coefficient changes through the transition.

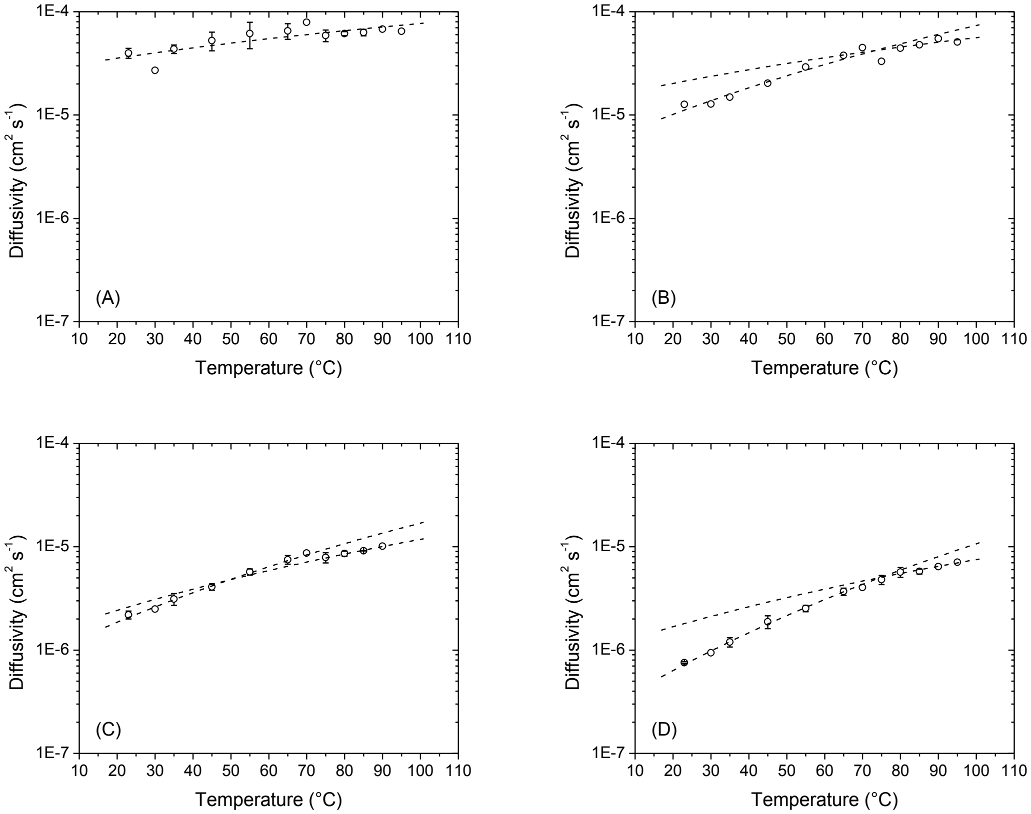

*Figure 78.* He (A), $H_2$ (B), $O_2$ (C), and $CO_2$ (D) diffusivity for f10 as a function of temperature. Dotted lines indicate attempted van't Hoff fits above and below $T_m$ where applicable.

Solubility versus temperature is plotted in Figure 79 for He, $H_2$, $CO_2$ and $O_2$. It is apparent that there was a jump in solubility at the melt transition temperature for $H_2$, $CO_2$ and $O_2$. Helium does not show a significant change in solubility across the melting transition. The temperature dependence of $CO_2$ solubility indicates a negative enthalpy of sorption, indicative of strong affinity between the polymer and the gas. Oxygen solubility shows a weak negative dependence on temperature. The recorded jump in solubility for $H_2$, $CO_2$, and $O_2$ was expected to be from an increase in sorption sites as the side chain order was disrupted through melting.

It would be expected that a relatively lower crystalline content, compared to aliphatic side chain polymers, would lead to less tortuosity and therefore a smaller step size in the diffusivity. The amorphous volume fraction was estimated using Michaels and Bixler's models as interpreted by Mogri, D. Paul[5], where $S = S^{*}\alpha$ and $D = \frac{D^{*}}{\tau ß}$, therefore $\frac{P^{*}}{P} = \frac{\tau ß}{\alpha}$ where X* is the melt state P,D, or S. Using the two gases that show a considerable jump, $CO_2$ and $O_2$, we are able to estimate the amorphous fraction to be 0.56 and 0.53 respectively. These values do not agree with density based crystalline content determinations described earlier. As discussed by Mogri[5], this model was developed for a simplified two-phase semicrystalline model where the crystalline domains and the backbone are chemically identical. Since we know this is not the case, the amorphous fraction should not be quantified in this way.

Conventional semicrystalline polymer theory suggests that crystalline domains provide a tortuous path to the diffusing gas, deviating from pure random walk diffusion. A gas diffusing through a tortuous path decreases the permeability of small gases by increasing the total diffusion path length, whereby, upon melting the crystals, the tortuous path is eliminated and the diffusion would increase as the diffusion path returns to that of a pure random walk. The decreased packing density of these perfluorinated materials may not cause the tortuosity effects that are found with semicrystalline polymers or even the analogous side chain linear alkyl, rather, permeability gains through the transition are purely from an increase in sorption sites, increasing solubility of the system.

This explains the smaller permeability gains through the transition compared to the linear aliphatic side chain materials.

The overall decrease in magnitude of the permeability jump difference between alkyl side chains and perfluoroalkyl chains was due to a lack of diffusion jump in perfluoroalkyl chains. In many polymeric systems diffusivity changes dominate the “switching” behavior upon melting, as shown in linear aliphatic side chains. The presence of a solubility jump and the absence of a diffusivity jump at $T_m$ require the investigation of sorption phenomena. This will be covered in a subsequent publication.

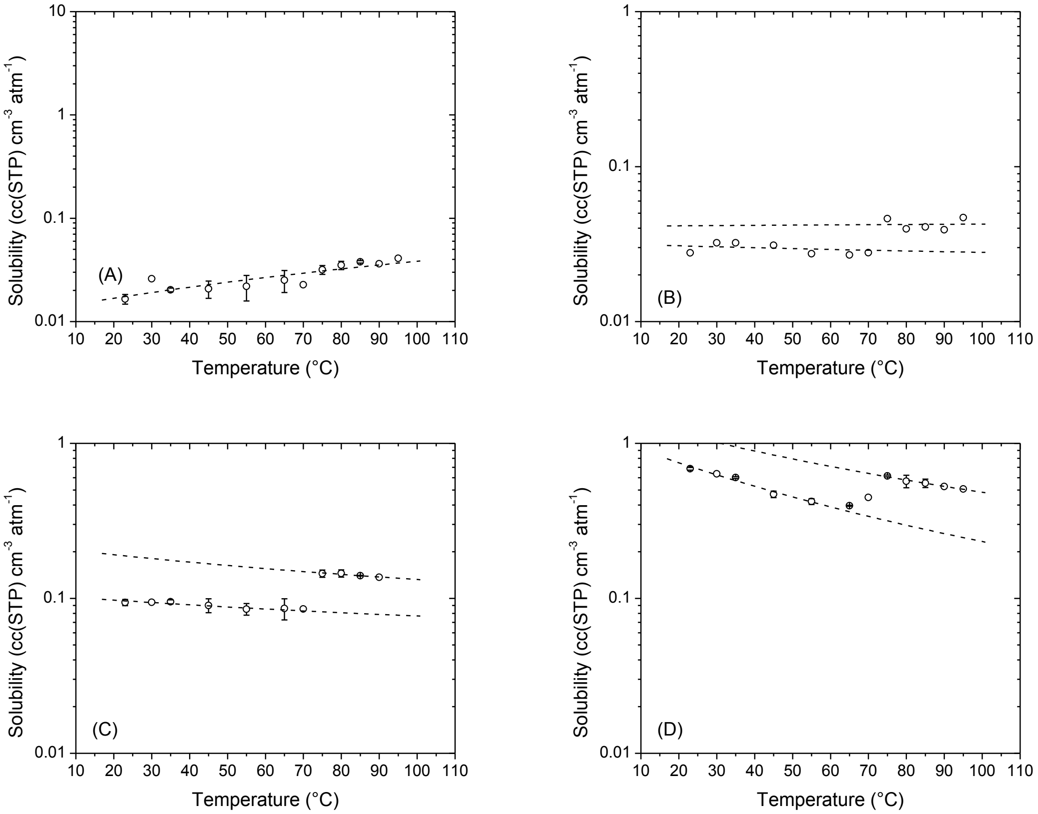

*Figure 79*. He (A), $H_2$ (B), $O_2$ (C), and $CO_2$ (D) solubility for f10 as a function of temperature. Dotted lines are van’t Hoff fits of data above and below the melting temperature.

The penetrant size dependence of the permeability switch is shown in Figure 80 according to the methods of Mogri.[6] Similar to the reported results, the size dependence follows the Lennard-Jones diameter considering $CO_2$ behaves more as a cylinder than as a sphere. Also noted compared to Mogri's results, the step change is a full order of magnitude greater in aliphatic side chain polymers compared to the studied f10. Here we confirm the size dependence of the permeation switch.

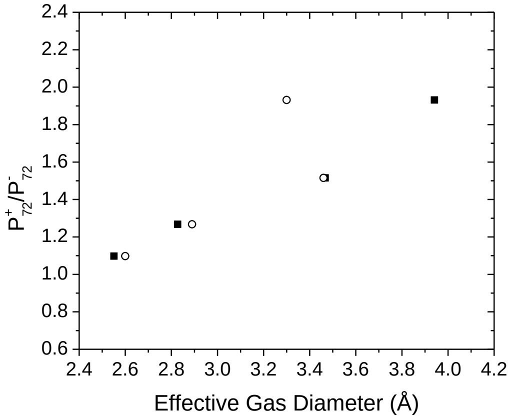

*Figure 80*. Permeation switch magnitude for f10 as a function of estimated kinetic diameter (○) and Lennard-Jones diameter (■).

Table 8

*Permeability (P), Diffusivity (D) and Solubility (S) as for $O_2$, $CO_2$, $H_2$, and He at all tested temperatures.*

| Temperature | $O_2$ | | | $CO_2$ | | | $H_2$ | | | He | | |
|---|---|---|---|---|---|---|---|---|---|---|---|---|
| °C | P* | D** | S*** | P | D | S | P | D | S | P | D | S |
| 23 | 27 | 2.2 | 9.4 | 68 | 0.8 | 68.5 | 46 | 12.7 | 2.8 | 86 | 39.7 | 1.7 |
| 30 | 31 | 2.5 | 9.4 | 79 | 0.9 | 63.5 | 54 | 12.8 | 3.2 | 93 | 27.1 | 2.6 |
| 35 | 39 | 3.1 | 9.5 | 95 | 1.2 | 60.2 | 63 | 14.9 | 3.2 | 116 | 43.5 | 2.0 |
| 45 | 48 | 4.1 | 9.0 | 115 | 1.9 | 46.9 | 83 | 20.3 | 3.1 | 140 | 52.6 | 2.1 |
| 55 | 64 | 5.7 | 8.5 | 140 | 2.5 | 42.1 | 105 | 29.1 | 2.7 | 168 | 61.4 | 2.2 |

Table 8 (continued).

| Temperature | $O_2$ | | | $CO_2$ | | | $H_2$ | | | He | | |
|---|---|---|---|---|---|---|---|---|---|---|---|---|
| °C | P* | D** | S*** | P | D | S | P | D | S | P | D | S |
| 65 | 85 | 7.5 | 8.6 | 192 | 3.7 | 39.6 | 134 | 37.8 | 2.7 | 211 | 65.3 | 2.5 |
| 70 | 97 | 8.7 | 8.5 | 238 | 4.0 | 44.7 | 165 | 44.9 | 2.8 | 236 | 79.0 | 2.3 |
| 75 | 149 | 7.9 | 14.4 | 389 | 4.8 | 61.6 | 201 | 33.1 | 4.6 | 244 | 58.9 | 3.2 |
| 80 | 164 | 8.6 | 14.5 | 423 | 5.7 | 56.9 | 232 | 44.4 | 4.0 | 284 | 61.4 | 3.5 |
| 85 | 168 | 9.2 | 14.0 | 419 | 5.8 | 55.4 | 256 | 47.7 | 4.1 | 314 | 63.0 | 3.8 |
| 90 | 182 | 10.1 | 13.7 | 444 | 6.4 | 52.6 | 282 | 54.9 | 3.9 | 323 | 67.9 | 3.6 |
| 95 | - | - | - | 474 | 7.1 | 50.8 | 314 | 50.9 | 4.7 | 348 | 64.6 | 4.1 |

* Permeability in the units Barrer ** Diffusivity in $cm^2 sec^{-1}$ x $10^6$ *** Solubility in $cc(STP)/cc_{polymer}$

Table 9

*van't Hoff pre-exponential factors, activation energies of diffusion, apparent activation energies of permeation and heats of sorption for He, $H_2$, $O_2$, and $CO_2$. $H_2$, $O_2$, and $CO_2$ values are tabulated for van't Hoff fits below (-) and above (+) the $T_m$.*

| Gas | $E_P$ kcal/mol | $E_D$ kcal/mol | $\Delta H_S$ kcal/mol | $P_0$ Barrer | $D_0$ $cm^2 sec^{-1}$ | $S_0$ cc(STP) $cc^{-1}$ $atm^{-1}$ |
|---|---|---|---|---|---|---|
| He | 4.37 | 2.10 | 2.24 | 140359 | 0.0013 | 0.7887 |
| $H_2$ | 5.04 | 5.29 | -0.245 | 240382 | 0.0904 | 0.0202 |
| | 5.19 | 2.84 | 0.040 | 380871 | 0.0026 | 0.0405 |
| CO2 | 4.48 | 7.67 | -3.181 | 137037 | 0.3332 | 0.0032 |
| | 2.11 | 4.07 | -2.371 | 8355 | 0.0018 | 0.0197 |
| $O_2$ | 5.36 | 5.99 | -0.642 | 238250 | 0.0555 | 0.0323 |
| | 3.14 | 4.29 | -0.999 | 14150 | 0.0039 | 0.0344 |

Table 10

*Relative transport parameters, $X_{72}^{+}/X_{72}^{-}$, for $H_2$, $CO_2$, and $O_2$.*

| | 72 °C | | | 25 °C | | |
|---|---|---|---|---|---|---|
| | $P^+/P^-$ | $D^+/D^-$ | $S^+/S^-$ | $P^+/P^-$ | $D^+/D^-$ | $S^+/S^-$ |
| He | - | - | - | - | - | - |
| $H_2$ | 1.27 | 1.02 | 1.32 | 1.23 | 1.80 | 1.24 |
| $CO_2$ | 1.93 | 1.03 | 1.89 | 2.52 | 1.24 | 1.95 |
| $O_2$ | 1.52 | 0.84 | 1.79 | 3.33 | 2.35 | 1.57 |

Considering the jump in permeability coming from the increase in gas solubility, it was interesting to note not only the large free volume hole size but also the large jump in hole size, probed by positron annihilation, from our previous paper.[7] Considering the Cohen-Turnbull model,[30] where the diffusivity is shown to be dependent on the fractional free volume, one would expect the diffusivity to change drastically through the melt transition as a result of the reported jump in hole size. o-Ps used to probe free volume elements in PALS has an estimated diameter of 1.58 Å which would be able to probe regions smaller than accessible to helium which has a diameter of 2.6 Å. Here, o-Ps shows the step change in lifetime where He transport properties do not. The probing o-Ps may also be able to thermalize into regions of the crystalline structure that He cannot diffuse into.

It was apparent that the free volume elements in this system should not be assumed to be spherical, rather a distribution of spherical and cylindrical holes. Therefore, it is important that we report the lifetimes o-Ps in the studied systems avoiding the assumption that the holes are spherical. It has been shown by various groups that the lifetime of o-Ps does correlate with the hole size but here, we cannot estimate a homogeneous hole shape. Figure 81 shows the o-Ps lifetimes for f8, f10 and f12 systems as a function of temperature probed from 0 to 190 °C.

Furthermore, the relative intensity of o-Ps is shown in Figure 82 as a function of temperature. F8 shows typical behavior for amorphous polymers with no step change in the studied region from 0 to 190 °C. f10 and f12 show step changes in intensity at $T_m$ suggesting an increase in the relative number of positrons emissions yielding o-Ps. Above $T_m$, the intensity values for f8, f10, and f12 converge suggesting similar chemical and morphological environments in the polymer. The step change in f10 and f12 suggests a decreased formation of o-Ps in the crystalline phase or that the crystalline phase causes annihilation of free positrons and p-Ps more readily.

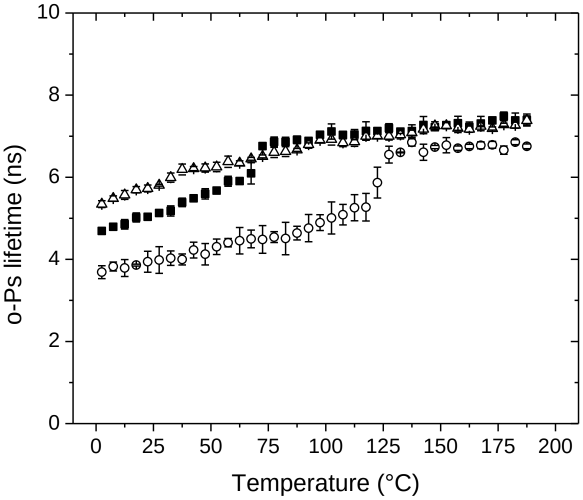

*Figure 81*. Positron annihilation o-Ps lifetimes, $\tau_3$, for f8 (△), f10 (■), and f12 (○).

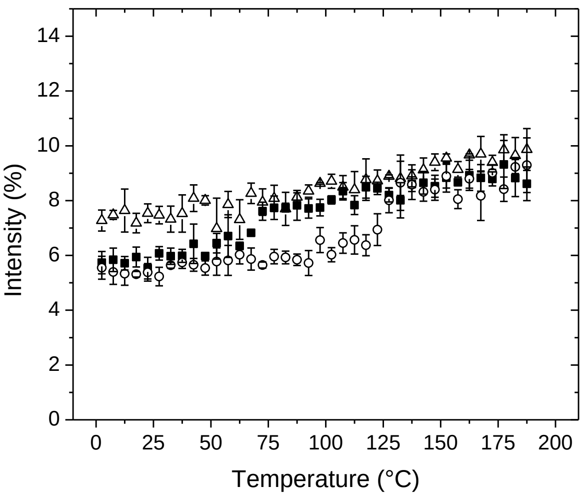

*Figure 82.* Positron annihilation relative intensities for f8 (△), f10 (■), and f12 (○).

To achieve a full understanding of free volume, one must understand the limitations of the positron annihilation technique as this is a good predictor of the hole sizes but not the concentration or number of holes in a given unit volume. To probe the fractional free volume, pressure volume temperature (PVT) experiments were performed to determine the free volume contribution to the permeability switch at Tm. Figure 72 shows the specific volume, temperature data gathered from a standard isothermal pressure sweep analysis as described in the Experimental section. Using this data, we were able to determine the fractional free volume using the Simha Somcynsky equations of state (SS-EOS) through the determination the occupied fraction of lattice sites in melt state of these networks using[18]

Equation 51: $$\frac{\tilde{P}\tilde{V}}{\tilde{T}} = \left[1 - y\left(2^{\frac{1}{2}}\, y\, \tilde{V}\right)^{-\frac{1}{3}}\right]^{-1} + \frac{y}{\tilde{T}}\left[2.002\left(y\,\tilde{V}\right)^{-4} - 2.409\left(y\,\tilde{V}\right)^{-2}\right]$$

Equation 52: $$\mathrm{FFV} = \frac{\left(V_{sp} - V_{occ}\right)}{V_{sp}}$$

where y is the fraction of occupied lattice sites. Fractional free volume was determined using Equation 52 where $V_{occ} = V_{sp} * y$. Figure 72 shows the fit of the SS-EOS to the $V_{sp}$ temperature data and the resolved occupied volume from Equation 51. Figure 83 shows the temperature dependence of fractional free volume showing a convergence above $T_m$ for all studied systems. F12 systems show a lower fractional free volume than f10 at temperatures below $T_m$ most likely caused by the increased fluorine content and the increase side chains contributing to the crystalline, low free volume fraction.

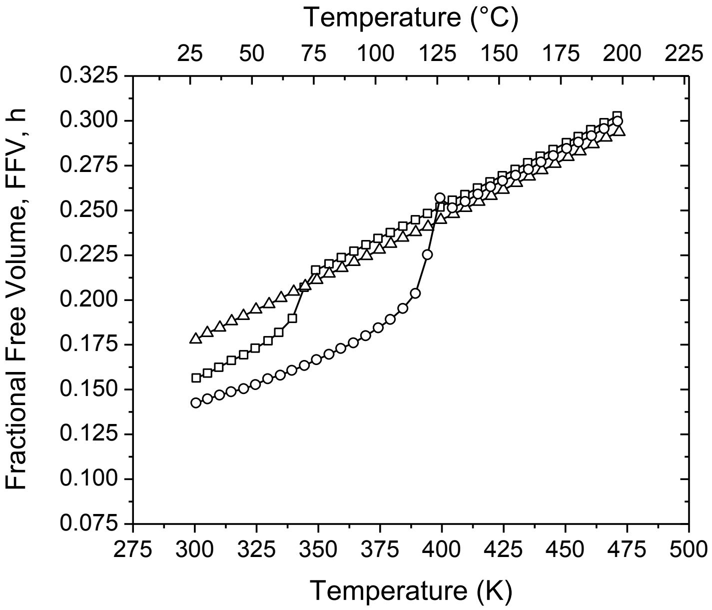

*Figure 83.* Fractional free volume for f8 (△), f10 (□), and f12 (○).

*Gas Separation Performance*

The gas separation performance of a polymeric membrane can be evaluated using

$$\text{Equation 51} \quad \alpha = \frac{P_A}{P_B} = \frac{D_A}{D_B} * \frac{S_A}{S_B}$$

where α is the selectivity between the gas pair *A* and *B*. A is the relatively more permeable, or "fast," gas compared to gas B. The contributing factors leading to permeability selectivity can be determined by analyzing the diffusivity and solubility selectivity. Pure gas separation performance for He/$H_2$ and He/$CO_2$ was determined and plotted in Figure 84A and 84B respectively. Here the data represents data from the van't Hoff fits of the experimental data. At ambient conditions (filled circles) He/$H_2$ separations achieve a level of performance above the 1991 tradeoff upper bound to join a few select fluorinated polymers capable of this separation.[33,34] Temperature dependence of these separations is shown with the open data points with increasing permeability, reflecting the data shown in Figure 84. It is very interesting that the separation performance parallels the upper bound until the melt transition and jumps below the upper bound line. There have been reports of the temperature dependence of the upper bound trade off limit,[35] but here we show the temperature dependence of selectivity to showcase the importance of the morphology in the separation performance of He/$H_2$ and He/$CO_2$. It was expected that the permeability of a light gas will increase and selectivity will decrease as temperature rises. Here we see such performance in He/$H_2$ separation but a slight increase in separation performance as the temperature was increased in the melt state for He/$CO_2$.

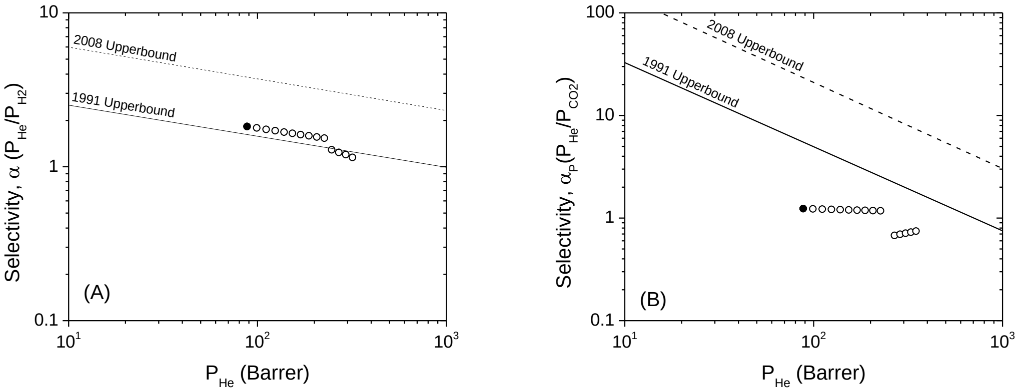

*Figure 84.* f10 He/$H_2$ (A) and He/$CO_2$ (B) separation performance plotted against the Robeson upper bound[34] at ambient (●) and elevated temperatures (○).

Further investigation of the contributing factors leading to the He/$H_2$ separation performance required the observation of D and S selectivity as a function of temperature. Figure 85 shows the van't Hoff fit data for P, D, and S selectivity based on Equation 51. He/$H_2$ solubility selectivity plays little role in the permeability selectivity as both He and $H_2$ have a low solubility in f10. Permeability selectivity was therefore the result of the diffusivity selectivity. Interestingly, the diffusivity did not play a large role in the step change in Tm as shown previously. However the selectivity values show that there was a change in the diffusion selectivity at the melt transition as He and $H_2$ diffusivity converge above the melt temperature. This behavior can be attributed to the small change in diffusivity slope as a function of temperature in the larger gases, $H_2$ and $CO_2$ and the lack of an apparent change in slope in the temperature dependence of He diffusivity.

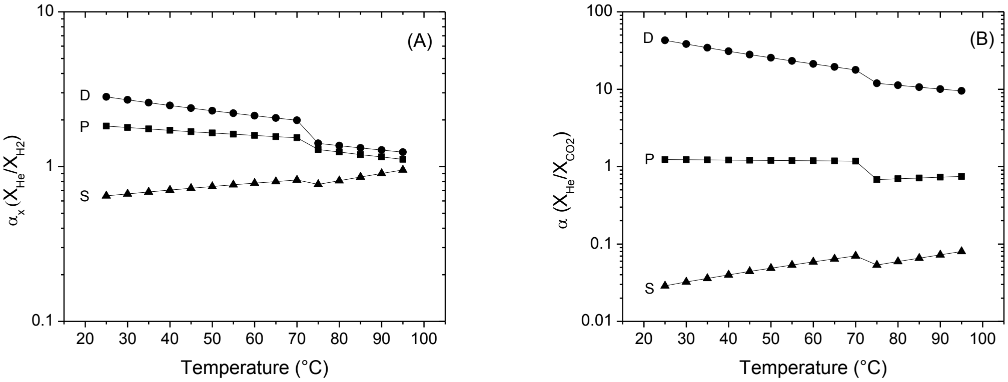

*Figure 85*.- Permeability, diffusivity, and solubility selectivity as a function of temperature for He/$H_2$ (A) and He/$CO_2$ (B). Data plotted here is from the van’t Hoff fits of the original data.

## Conclusions

The liquid crystalline structure of three perfluorinated side chain acrylates was exploited for the well-defined crystalline order and melting temperature. The well-defined order of $C_8F_{17}$ and $C_{10}F_{21}$ side chain acrylates was characterized and shown to develop a mesophase upon UV-curing that was irreversible unless rapidly thermally quenched. The well-defined melting temperature of $C_8F_{17}$ (f10) at 72 °C was exploited in the study of gas transport properties that traversed this melting temperature showcasing low degrees of permeability switching. Permeability gains across the melting of the ordered morphology for several gases were shown to be due to solubility increases alone. Contrary to standard two-phase systems where ordered phases increase tortuosity and therefore diffusivity in the semicrystalline systems, these systems show no detectable switch in diffusivity across the transition temperature. Analysis of both the free volume hole size and volume contributions suggest increases in both hole size and fractional free volume. Furthermore, the side chain morphology lends itself to high He/$H_2$ separation performance from the size dependence of the diffusion coefficient.

## References

(1) Honda, K.; Morita, M.; Otsuka, H.; Takahara, A. *Macromolecules* **2005**, *38*, 5699.

(2) Honda, K.; Morita, M.; Sakata, O.; Sasaki, S.; Takahara, A. *Macromolecules* **2009**, *43*, 454.

(3) Volkov, V. V.; Platé, N. A.; Takahara, A.; Kajiyama, T.; Amaya, N.; Murata, Y. *Polymer* **1992**, *33*, 1316.

(4) Volkov, V. V.; Fadeev, A. G.; Plate, N. A.; Amaya, N.; Murata, Y.; Takanara, A.; Kajiyama, T. *Polymer Bulletin* **1994**, *32*, 193.

(5) Mogri, Z.; Paul, D. R. *Polymer* **2001**, *42*, 2531.

(6) Mogri, Z.; Paul, D. R. *Polymer* **2001**, *42*, 7765.

(7) Goetz, J.; Nazarenko, S. *J Coat Technol Res* **2013**, 1.

(8) Cheng, S. Z. D.; Cao, M. Y.; Wunderlich, B. *Macromolecules* **1986**, *19*, 1868.

(9) Kwisnek, L.; Heinz, S.; Wiggins, J. S.; Nazarenko, S. *Journal of Membrane Science* **2011**, *369*, 429.

(10) Lin, H.; Freeman, B. D. *Journal of Membrane Science* **2004**, *239*, 105.

(11) Lin, H.; Wagner, E. V.; Swinnea, J. S.; Freeman, B. D.; Pas, S. J.; Hill, A. J.; Kalakkunnath, S.; Kalika, D. S. *Journal of Membrane Science* **2006**, *276*, 145.

(12) Raharjo, R. D.; Lin, H.; Sanders, D. F.; Freeman, B. D.; Kalakkunnath, S.; Kalika, D. S. *Journal of Membrane Science* **2006**, *283*, 253.

(13) Olson, B. G.; Lin, J.; Nazarenko, S.; Jamieson, A. M. *Macromolecules* **2003**, *36*, 7618.

(14) Zoller, B., Pahud, Ackermann *Review of Scientific Instruments* **1976**, *47*, 948.

(15) Mogri, Z.; Paul, D. R. *Polymer* **2001**, *42*, 7781.

(16) Kirkland, B. S.; Engineering, T. U. o. T. a. A. C. *Gas Transport Properties of Poly(n-alkyl Acrylate) Blends and Modeling of Modified Atmosphere Storage Using Selective and Non-selective Membranes*; The University of Texas at Austin, 2007.

(17) Goetz, J.; Nazarenko, S. *J Coat Technol Res* **2014**, *11*, 123.

(18) Dlubek, G.; Sen Gupta, A.; Pionteck, J.; Krause-Rehberg, R.; Kaspar, H.; Lochhaas, K. H. *Macromolecules* **2004**, *37*, 6606.

(19) Dlubek, G.; Pionteck, J.; Sniegocka, M.; Hassan, E. M.; Krause-Rehberg, R. *Journal of Polymer Science Part B: Polymer Physics* **2007**, *45*, 2519.

(20) Utracki, L. A.; Simha, R. *Macromolecular Theory and Simulations* **2001**, *10*, 17.

(21) Utracki, L. A.; Jamieson, A. M. *Polymer Physics: From Suspensions to Nanocomposites and Beyond*; Wiley, 2011.

(22) Dlubek, G.; Pionteck, J. *Acta Physica Polonica A* **2008**, *113*, 1331.

(23) Mark, J. E. *Physical Properties of Polymers Handbook*; Springer London, Limited, 2007.

(24) Lin, H.; Freeman, B. D. *Macromolecules* **2006**, *39*, 3568.

(25) Daynes, H. A. *Proceedings of the Royal Society of London. Series A* **1920**, *97*, 286.

(26) Breck, D. W. *Zeolite molecular sieves: structure, chemistry, and use*; Wiley, 1973.

(27) Poling, B.; Prausnitz, J.; Connell, J. O. *The Properties of Gases and Liquids*; Mcgraw-hill, 2000.

(28) Prodpran, T.; Shenogin, S.; Nazarenko, S. *Polymer* **2002**, *43*, 2295.

(29) Michaels, A. S.; Bixler, H. J. *Journal of Polymer Science* **1961**, *50*, 413.

(30) Cohen, M. H.; Turnbull, D. *The Journal of Chemical Physics* **1959**, *31*, 1164.

(31) Michaels, A. S.; Parker, R. B. *Journal of Polymer Science* **1959**, *41*, 53.

(32) Jordan, E. F.; Feldeisen, D. W.; Wrigley, A. N. *Journal of Polymer Science Part A-1: Polymer Chemistry* **1971**, *9*, 1835.

(33) Robeson, L. M. *Journal of Membrane Science* **1991**, *62*, 165.

(34) Robeson, L. M. *Journal of Membrane Science* **2008**, *320*, 390.

(35) Rowe, B. W.; Robeson, L. M.; Freeman, B. D.; Paul, D. R. *Journal of Membrane Science* **2010**, *360*, 58.